# Bioenergetics of mixotrophic metabolisms: A theoretical analysis

by

Stephanie Slowinski

A thesis

presented to the University of Waterloo

in fulfillment of the

thesis requirement for the degree of

Master of Science

in

Earth Sciences (Water)

Waterloo, Ontario, Canada, 2019

© Stephanie Slowinski 2019

## Author's Declaration

This thesis consists of material all of which I authored or co-authored: see Statement of Contributions included in the thesis. This is a true copy of the thesis, including any required final revisions, as accepted by my examiners.

I understand that my thesis may be made electronically available to the public.

## Statement of Contributions

This thesis consists of two co-authored chapters.

I contributed to the study design and execution in chapters 2 and 3. Christina M. Smeaton (CMS) and Philippe Van Cappellen (PVC) provided guidance during the study design and analysis. I co-authored both of these chapters with CMS and PVC.

# Abstract

Many biogeochemical reactions controlling surface water and groundwater quality, as well as greenhouse gas emissions and carbon turnover rates, are catalyzed by microorganisms. Representing the thermodynamic (or bioenergetic) constraints on the reduction-oxidation reactions carried out by microorganisms in the subsurface is essential to understand and predict how microbial activity affects the environmental fate and transport of chemicals. While organic compounds are often considered to be the primary electron donors (EDs) in the subsurface, many microorganisms use inorganic EDs and are capable of autotrophic carbon fixation. Furthermore, many microorganisms and communities are likely capable of mixotrophy, switching between heterotrophic and autotrophic metabolisms according to the environmental conditions and energetic substrates available to them. The potential for switching between metabolisms has important implications for representing microbially-mediated reaction kinetics in environmental models. In this thesis, I integrate existing bioenergetic and kinetic formulations into a general modeling framework that accounts for the switching between metabolisms driven by either an organic ED, an inorganic ED, or both.

In Chapter 2, I introduce a conceptual model for mixotrophic growth. The conceptual model combines the carbon and energy balances of a cell by accounting for the allocation of an organic ED between incorporation into biomass growth and the generation of energy in catabolism. I select experimental datasets from the literature in which mixotrophic growth of pure culture organisms is assessed in chemostats. These experiments employ biochemical methods that allow one to estimate the contributions of the possible end-member metabolisms under variable supply rates of organic and inorganic EDs. Using the conceptual model, I develop a quantitative modeling framework that explicitly accounts for the substrate utilization kinetics and the energetics of the catabolic and anabolic reactions. I then compare the model predictions to the experimental data.

While in Chapter 2 datasets collected in controlled laboratory settings are considered, in Chapter 3 I apply my modeling framework for mixotrophic growth to a lake sediment geochemistry dataset. I focus on the activity of a nitrate reducing, acetate and iron(II) oxidizing mixotrophic microbial community in the suboxic zone of the lake sediment. I demonstrate the application of the modeling framework to this natural system, based on the reported concentration profiles of the relevant EDs (*i.e.*, acetate and iron(II)), electron acceptors (EAs) (*i.e.*, nitrate), and other reactants and products to calculate the depth distributions of the energetic and kinetic constraints in the model calculations. The predicted fractions of the metabolic end-members are in general agreement with the relative distributions of the different microbial functional groups reported in the original study. I also assess the sensitivity of the model's predictions on the kinetic parameter values used to simulate the net utilization rates of the two EDs. The results of the analysis provide new insights into the role of mixotrophy in the coupled cycling of nitrogen, iron(II), and dissolved inorganic carbon in the nitrate-reducing zone of lake sediments.

The conceptual model and modeling framework presented in this thesis can be used to account for mixotrophic activity in environmental reactive transport models. That is, in the future, this modeling framework could be incorporated into models that simulate the interactions of mixotrophy with other geochemical, geomicrobial, and transport processes. The work presented in this thesis is thus a valuable step towards building realistic theoretical representations of microbial activity in earth's near surface environments.

# Acknowledgements

Thank you to Philippe Van Cappellen, my supervisor, for your enthusiasm for bioenergetics and geochemistry, encouraging words, and support.
Thank you to Christina Smeaton, my co-supervisor, for your open-door policy, patient teaching, and encouragement. My completion of this thesis would not have been possible without your support.
Thank you to my committee members, Carol Ptacek and Laura Hug, for your words of advice on my research and meeting deadlines, and for sharing encouraging words.
Thank you to Marianne Vandergriendt for her support during my time in the lab. Thank you to Greg Friday, Elodie Passeport, Catherine Landesman, Adrian Mellage, Samantha Burke, and Leslie Bragg for taking the time to discuss the details of potential experimental work with me. Thank you to Shannon Oliphant for her work developing lab methods that I used. Thank you to Chris Parsons for answering my chemistry questions on the fly in the lab at times.
Thank you to everyone else in the Ecohydrology research group and Earth Sciences department who has offered me research and/ or academic support.

I am unable to thank all the people that have been present in my life during this degree. Thank you to everyone who has: shared a hello or a wave in the hallway, shared encouraging words, shared in intramural games, or discussed biogeochemistry, experimental, coding, or modeling concepts with me. Thank you especially to everyone who has taken the time to discuss the big picture with me and helped me to refocus my perspective. These conversations have meant so much to me.
(And a special shout-out to my roommates, Wynona, Rachel, Christine, and sometimes Camille!)

Thank you to my Mom and Dad for so much support in so many ways (it's hard to express and there's no way to quantify it!) Thanks also to Kathy, Don, James, Erika, Ellie, Nathalie, Evelyn and Sophia for your support.

# Table of Contents

# List of Figures

# List of Tables

# List of Abbreviations

| *Abbreviation* | *Description* | *Units* |
|---|---|---|
| ATP | Adenosine triphosphate | - - - |
| ED | Electron donor substrate | mol ED |
| EA | Electron acceptor substrate | mol EA |
| MEM | Metabolic end member | - - - |
| OH | Organoheterotrophy | - - - |
| LH | Lithoheterotrophy | - - - |
| LA | Lithoautotrophy | - - - |
| SWI | Sediment-water interface | - - - |
| Redox | Reduction-oxidation | - - - |
| eeq | Electron equivalents, number of electrons transferred during a reduction or oxidation half reaction. Used in this thesis to normalize ED utilization rates to a common unit, and thus represents the number of electrons that would be released by the complete oxidation of that ED. | - - - |
| $n_{eeq}^{S}$ | Number of moles of electron equivalents in some compound, S (electrons released by the complete oxidation of a compound) | mol eeq (mol S)$^{-1}$ |
| $r_{ED}$ | Rate of utilization of inorganic or organic ED substrate for use as ED by metabolic reaction (denoted by subscript *inorg ED* or *org ED*) | mol ED (L h)$^{-1}$ |
| $r_{eeq}$ | Rate of utilization of inorganic or organic ED substrate for use as ED by metabolic reaction in units of mol eeq (L h)$^{-1}$ (denoted by subscript *inorg eeq* or *org eeq*) | mol eeq (L h)$^{-1}$ |
| $x_{ik}$ | Fraction of metabolic end member reaction used to build biomass, where the subscript $i$ denotes the electron donating reaction used by the catabolism and anabolism, and $k$ denotes the carbon source | - - - |
| $x_{oh}$ | Fraction of organoheterotrophy (MEM/ biomass fraction) | - - - |
| $x_{lh}$ | Fraction of lithoheterotrophy (MEM/ biomass fraction) | - - - |
| $x_{la}$ | Fraction of lithoautotrophy (MEM/ biomass fraction) | - - - |
| $r_x$ | Total biomass growth rate | C-mol biomass (L h)$^{-1}$ |
| $r_{x,het}$ | Rate of heterotrophic biomass growth | C-mol biomass (L time)$^{-1}$ |

| | | |
|---|---|---|
| $r_{x,auto}$ | Rate of autotrophic biomass growth | C-mol biomass (L time)$^{-1}$ |
| $f_{assim}^{org}$ | Fraction of electron equivalents from the organic ED/ carbon source substrate that is used as a carbon source | - - - |
| $f_{dissim}^{org}$ | Fraction of electron equivalents from the organic ED/ carbon source substrate that is used as an electron donor | - - - |
| $f_k$ | Fraction of metabolism that is either heterotrophic or autotrophic | - - - |
| $f_h$ | Fraction of biomass carbon that is derived from organic carbon source/ ED (fraction of total mixotrophic biomass/metabolism that is heterotrophic) | - - - |
| $f_a$ | Fraction of biomass carbon that is derived from inorganic carbon (fraction of total mixotrophic biomass/metabolism that is autotrophic) | - - - |
| $\phi_i$ | Fraction of total electrons donated to metabolism (for energy conservation and generation in both catabolism and anabolism) that is either organotrophic or lithotrophic | - - - |
| $\phi_o$ | Fraction of electrons donated for oxidation that are from the organic ED substrate, "fraction of organotrophy" | - - - |
| $\phi_l$ | Fraction of electrons donated for oxidation that are from the inorganic ED substrate, "fraction of lithotrophy" | - - - |
| $\Delta G_r$ | Gibbs energy of a reaction under non-standard state conditions | kJ (mol ED)$^{-1}$ or kJ (C-mol biomass)$^{-1}$ |
| $\Delta G_r^\circ$ | Gibbs energy of a reaction under standard state conditions (25 °C, and unit activities for all chemical species) | kJ (mol ED)$^{-1}$ or kJ (C-mol biomass)$^{-1}$ |
| $\Delta G_r^{\circ\prime}$ | Gibbs energy of a reaction under biochemical standard state conditions (25 °C, pH 7 and unit activities for all chemical species, except $H^+$) | kJ (mol ED)$^{-1}$ or kJ (C-mol biomass)$^{-1}$ |
| $met$ | Subscript used to denote metabolic reaction | - - - |
| $cat$ | Subscript used to denote catabolic reaction | - - - |
| $an$ | Subscript used to denote anabolic reaction | - - - |
| $r_{max}$ | Biomass-, yield-, and maximum specific growth rate-implicit maximum rate used in Monod-type kinetics | mol ED (L time)$^{-1}$ |
| $K_{ED}$ | Half-saturation constant used in Monod-type kinetics | mol ED (L)$^{-1}$ |

# Chapter 1
# General Introduction

## 1.1 Chemosynthetic microbial activity in the terrestrial subsurface

In the dark terrestrial subsurface, life and biogeochemical activity is dominated by chemosynthetic prokaryotic microorganisms which derive their energy from the oxidation of electron donors during chemical reduction-oxidation reactions (Whitman *et al.*, 1998; Newman and Banfield, 2002). These environments include aquifers, wetland and hydric soils, peatlands, and aquatic sediments. Globally, the terrestrial subsurface reservoir contains one fifth of the earth's organic carbon, and the production of carbon dioxide by soil respiration is an important flux in the carbon balance of terrestrial ecosystems (Anantharaman *et al.*, 2016). Microbial activity and its associated chemical transformations in these environments controls the speciation, toxicity, and mobility of important nutrients and contaminants (Hunter *et al.*, 1998; Thullner *et al.*, 2007), including for example perchlorate (Hubbard *et al.*, 2014), nitrate (Rivett *et al.*, 2008), uranium (Williams *et al.*, 2011), and trace metals (Torres *et al.*, 2015). Through the hydrological connections between the subsurface and surface water ecosystems, subsurface microbial activity has the potential to mediate nutrient fluxes that fuel harmful algal blooms, as well as other water quality issues (Bouwman *et al.*, 2013). The subsurface is also connected to the atmosphere via the soil interface, and many microbial activities produce greenhouse gases such as nitrous oxide ($N_2O$), carbon dioxide ($CH_4$), and carbon dioxide ($CO_2$) (Long *et al.*, 2016). In short, the activity of subsurface microorganisms contributes many societally-relevant ecosystem functions.

## 1.2 Chemosynthetic microbial metabolisms

During growth, microorganisms carry out two distinct reduction-oxidation (redox) reactions: they couple a reaction for the creation of biomass (the anabolic reaction) to the reaction from

which they derive energy (the catabolic reaction). The energy produced during the catabolic redox reaction is required by microorganisms to survive and grow. Redox reactions are those which involve the exchange of electrons between a reduced chemical species (the electron donor) and an oxidized species (the electron acceptor). The overall reaction, or the metabolic reaction, represents the combination of the catabolic and anabolic reactions.

Microbial metabolic reactions can be classified based on the identities of the electron donor (ED) and carbon source. In chemosynthetic microbial growth reactions, the ED is used as both an energy source by its reaction with an electron acceptor in catabolism, and for energy conservation in the anabolic redox reaction. Organoheterotrophic metabolisms use organic compounds for both energy generation (*i.e.*, as an electron donor) and as a carbon source. Lithoheterotrophic metabolisms use organic carbon compounds as their carbon source, while using an inorganic compound as their catabolic energy source. Lithoautotrophic metabolisms also use an inorganic energy source, while using inorganic carbon (*e.g.*, $CO_2$) as their carbon source. Figure 1-1 is a flow chart that shows the classification and relatedness of these different types of metabolisms. Chemotrophic metabolisms are also distinguished from phototrophic metabolisms in Figure 1-1.

The organic compounds that are commonly used as EDs and/or carbon sources in the subsurface include short chain organic acids (*e.g.*, propionate, lactate, or citrate) generated by the hydrolysis or fermentation of plant-derived polymeric organic molecules (Roden and Jin, 2011). Inorganic compounds that are commonly used as EDs in the subsurface include methane ($CH_4$), ammonia ($NH_4^+$), nitrite ($NO_2^-$), sulfide ($S^{2-}$), thiosulfate ($S_2O_3^{2-}$), iron(II) ($Fe^{2+}$), and dihydrogen ($H_2$). These reduced inorganic compounds are generated by many different processes. For example, weathering of the mineral pyrite produces $S^{2-}$ (Bosch and Meckenstock, 2012), and the

breakdown of organic matter by fermentation and nitrogen fixation by rhizobacterium produce $H_2$ (Lovley and Chapelle, 1995; Miltner *et al.*, 2005; Piché-Choquette and Constant, 2019). Microbial reduction of oxidized forms of the electron donor is also an important source of reduced compounds, such as iron(III) reduction producing $Fe^{2+}$ (Weber *et al.*, 2006; Schmidt *et al.*, 2010; Berg *et al.*, 2016). Anthropogenic input of $NH_4^+$ or $S^0$ via fertilizers is also possible (Lawrence *et al.*, 1988; He *et al.*, 2007). In the deep subsurface, additional processes can generate reduced inorganic compounds, including the serpentization of igneous rocks (*e.g.*, $H_2$) and Fischer-Tropsch type reactions (*e.g.*, $CH_4$) (Sherwood-Lollar *et al.*, 2008; Kieft, 2016).

The most common electron acceptors in anoxic subsurface environments are nitrate ($NO_3^-$), sulfate ($SO_4^{2-}$), iron(III) ($Fe^{3+}$), manganese(IV) ($Mn^{4+}$) and carbon dioxide ($CO_2$) (Bethke *et al.*, 2011; Burgin *et al.*, 2011). These electron acceptors can be used by both organotrophic and lithotrophic catabolic reactions. Microbial activity significantly influences the cycling of the common redox-active elements carbon (C), nitrogen (N), iron (Fe), sulfur (S), and manganese (Mn) in subsurface environments, which is evident given the use of different forms of these elements as both electron acceptors and electron donors. The extent of coupling between these elements can be captured by writing out the metabolic reactions that are occurring in any given environment. This microbial control of the cycling of these redox-active elements is well discussed in the biogeochemical literature (*e.g.*, Burgin *et al.*, 2011), and is a major theme of this thesis.

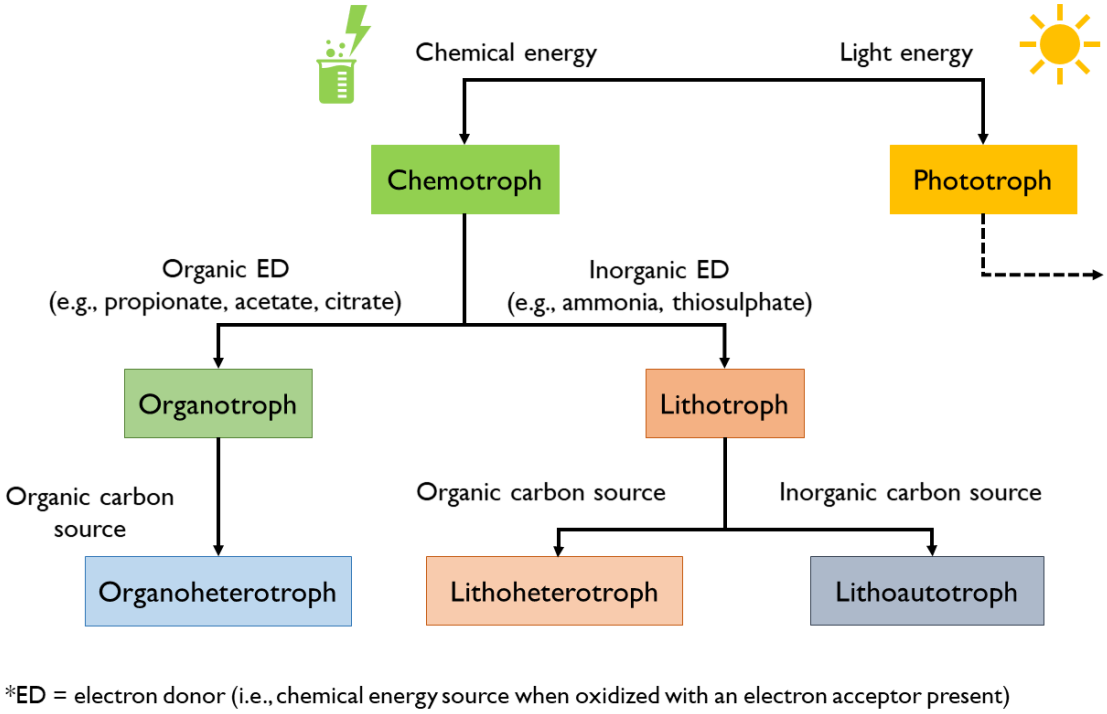


*Figure 1-1. Classification of microbial metabolisms based on the combination of the electron donor (ED) used for energy generation in the catabolic reaction and energy conservation in the anabolic reaction and the carbon source used for biomass.*

### 1.2.1 Bioenergetics: How chemical energy limits microbial activity

Through the exchange of electrons between the electron donor and electron acceptor during metabolism, chemicals are transformed to new forms such that the system has a lower chemical potential. The energy lost by the chemicals in the system due to the reaction is then gained by the organism catalyzing the reaction using an electron transport chain, and stored intracellularly as ATP (Bethke, 2008). Thus, microorganisms are open systems, exchanging energy and matter with their surroundings, and are not in thermodynamic equilibrium with the surroundings (Kleerebezem and Van Loosdrecht, 2010).

Non-equilibrium thermodynamics can be applied to quantify the chemical energy that is gained by microbial catabolic, anabolic and metabolic reactions and therefore how microbial activity is limited by the chemical energy available in a given environment. It is the Gibbs energy of a redox reaction ($\Delta G_r$) that describes the distance of a reaction from thermodynamic equilibrium and therefore also the potential energy that can be gained from that reaction (Kleerebezem and Van Loosdrecht, 2010). For example, the Gibbs energy derived from the oxidation of an organic compound to $CO_2$ coupled to the reduction of an electron acceptor such as $O_2$ depends on the oxidation state of the carbon atoms in the organic compound (Figure 1-2). The higher the oxidation state of carbon for those compounds, the more electrons are released by the oxidation of those carbon atoms to the oxidation state of $CO_2$ (the oxidation state of $CO_2$ is 4), and therefore the more Gibbs energy is released.

For an energy-yielding, thermodynamically favourable reaction, the change in Gibbs energy between products and reactants is negative (Figure 1-2). To calculate $\Delta G_r$, the standard state Gibbs energy of reaction, $\Delta G_r^\circ$ [kJ mol$^{-1}$], is calculated from the Gibbs energies of formations of the reactants and products using equation 1-1:

$$\Delta G_r^\circ = \sum \Delta G^\circ_{f,products} - \sum \Delta G^\circ_{f,reactants} \qquad (1\text{-}1)$$

To calculate the non-standard state Gibbs energy of reaction ($\Delta G_{rxn}$ [kJ mol$^{-1}$]), the reaction quotient (Q) is used:

$$\Delta G_r = \Delta G_r^\circ + RT\ln Q \qquad (1\text{-}2)$$

The reaction quotient is calculated using the actual chemical activities of the products and reactants of the reaction, and thus accounts for the deviation of the system from its corresponding standard state.

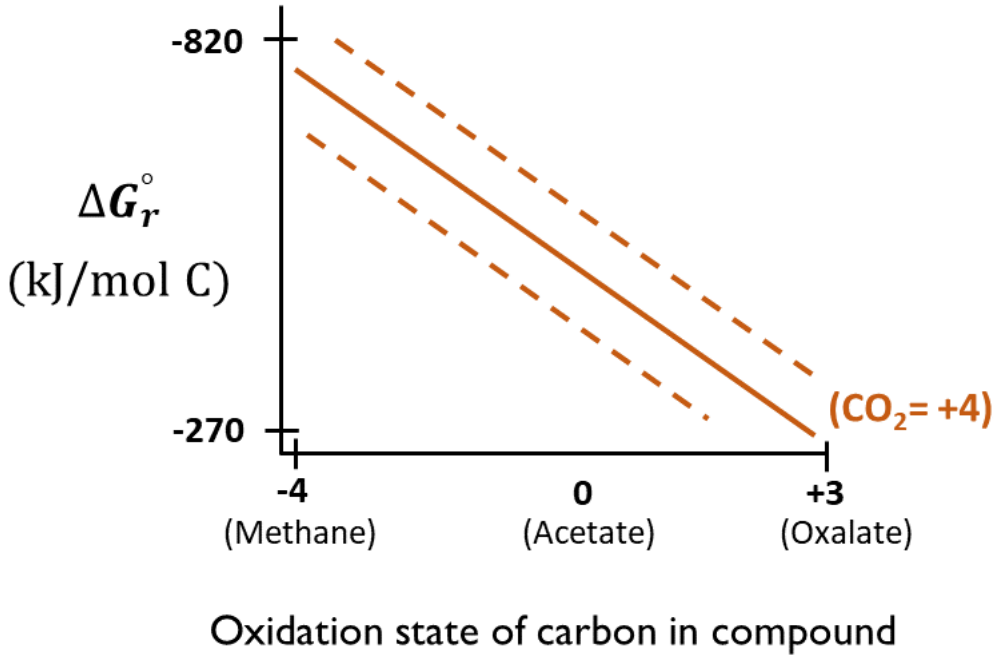


*Figure 1-2. Relationship between the nominal oxidation state of the carbon atoms in an organic compound and the Gibbs energy released by the oxidation of that compound coupled to the reduction of the electron acceptor $O_2$. Figure adapted from LaRowe and Van Cappellen (2011).*

### 1.3 Mixotrophy

Organisms that are metabolically flexible and capable of switching between organoheterotrophy, lithoheterotrophy and lithoautotrophy are called facultative chemolithoautotrophs or, alternatively, mixotrophs (Rittenberg, 1972; Kelly, 1981). These microorganisms possess the genes to carry out all three metabolisms, and can regulate which metabolism they use according to which one is most optimal under the given conditions (Rittenberg, 1972). This metabolic flexibility has been recognized in pure cultures for some time and is likely also a community-level attribute in a variety of environments.

Recognition of the widespread capacity for metabolic flexibility across many genera of bacteria and archaea is growing, especially with the increased use of omics techniques for analyzing laboratory cultures and environmental samples (Long, Williams, Hubbard, & Banfield, 2016). For example, the bacteria *Leptothrix ochracea,* one of the first lithotrophic organisms discovered by Winogradsky, was previously thought to be a strict lithoautotroph. When grown in an enrichment culture with different concentrations of iron(II), *L. ochracea* was able to assimilate both organic and inorganic carbon, revealing that it is capable of mixotrophy (Rittenberg, 1972; Fleming *et al.*, 2018).

#### 1.3.1 Environmental occurrence and controls on mixotrophy

In the environment, mixotrophy can be identified using metagenomic methods by the coincident occurrence of genes for carbon fixation and genes for assimilating organic compounds (Probst *et al.*, 2017), by stable isotope probing (Bellini *et al.*, 2018), by tracing natural carbon isotope fractionation (Probst *et al.*, 2018), or by Most Probable Number (MPN) approaches that employ mixotroph-specific media (Hauck *et al.*, 2001; Melton *et al.*, 2014).

The geochemical controls on the relative abundance of autotrophs versus heterotrophs have been discussed for some field studies, and for a variety of experimental and modeling studies. Many chemostat studies using either pure, enrichment, or mixed cultures have assessed the regulation of metabolic flexibility as a function of the changing supply ratios of an organic and inorganic ED by monitoring changes in enzyme production and cell physiology (Shively *et al.*, 2002). These experiments have collectively demonstrated that the relative utilization rates of inorganic versus organic electron donors determines whether or not autotrophy is induced (Dijkhuizen and Harder, 1984; Gommers *et al.*, 1988; Gottschal, 1993). In the presence of an organic compound that could be used for heterotrophic growth, autotrophy is only possible if there is a sufficient excess of the inorganic electron donor available (Dijkhuizen and Harder, 1984). Wegner *et al.* (2018) highlighted that the limited occurrence of nitrification and annamox, two lithoautotrophic metabolisms, in aquifer hotspots was constrained by the limited availability of inorganic electron donors. Most field studies, however, have focused on the occurrence and relative abundances of autotrophic and heterotrophic metabolisms in subsurface systems rather than relating them to the geochemical controls.

### 1.4 Representing microbial activity in biogeochemical models

Reactive transport models (RTMs) represent the coupling of geomicrobial, geochemical, and transport processes to predict the transformations of chemical species over time and space in the environment (Hunter *et al.*, 1998; Mayer *et al.*, 2002; Brookfield *et al.*, 2006; Li *et al.*, 2017). Many geochemical reactions are catalyzed by microorganisms, and for this reason, much attention has been given to representing them in RTMs (Arora *et al.*, 2015). Major progress has been made with implementing bioenergetics-based methods to describe how chemical energy limits chemosynthetic growth and reaction rates. Here, I summarize how bioenergetics is used in

RTMs by introducing how microbially-controlled reaction rates are represented in RTMs and then how bioenergetics can be integrated into these rate expressions to improve their realism.

### 1.4.1 Bioenergetics and the microbial growth yield

The motivation for applying bioenergetic methods in environmental models is to represent the regulating role of the $\Delta G_r$ of the net metabolic reaction, $\Delta G_{met}$. In doing so, one can predict how a group of microorganisms allocates the energy-yielding substrate they consume to growth relative to energy generated via the catabolic reaction, that is, the efficiency of growth. This is very relevant in biogeochemical models where the goal is to represent the turnover of substrate via catabolism as well as the growth of biomass, the catalyst of these reactions.

The $\Delta G_{met}$ is calculated using the catabolic and anabolic Gibbs energies (*i.e.*, $\Delta G_{cat}$ and $\Delta G_{an}$). It is the growth yield parameter, which describes the fraction of ED consumed that is used for biomass, and therefore represents the growth efficiency. The growth yield couples anabolism and catabolism via an energy balance, which accounts for the allocation of the energy in the ED substrate to either biomass (or reducing equivalents used to build biosynthetic molecules) or to generating energy via catabolism to build biomass. This is shown schematically in Figure 1-3 and mathematically in Eq. 1-3 (see Smeaton and Van Cappellen, 2018 for more details):

$$\Delta G_{met} = \frac{1 - Yv}{Y} \Delta G_{cat} + \Delta G_{an} \tag{1-3}$$

where $v$ is a stoichiometric coefficient that is used to non-dimensionalize Y from its usual units of, say, [C-mol biomass (mol ED)$^{-1}$], $\Delta G_{cat}$ is in units of [kJ (mol ED)$^{-1}$], $\Delta G_{an}$ is in units of [kJ (C-mol biomass)$^{-1}$], and $\Delta G_{met}$ is in units of [kJ (C-mol biomass)$^{-1}$].

The energy balance described in Eq. 1-3 can be rearranged to express the growth yield ($Y$) as a function of all three Gibbs energies (Smeaton and Van Cappellen, 2018):

$$Y = \frac{\Delta G_{cat}}{\Delta G_{met} + \Delta G_{cat} \nu - \Delta G_{an}} \quad (1\text{-}4)$$

Using this energy balance relationship, bioenergetics methods have focused on predicting the growth yields of specific microbial metabolisms by calculating $\Delta G_{cat}$ and $\Delta G_{an}$ for these metabolisms using the chemical activities of the reactants and products (*i.e.*, using Eq. 1-1 and 1-2), and then predicting the value of $\Delta G_{met}$ to calculate $Y$. This has been done by approximating the value of $\Delta G_{met}$ based on typically observed values (Heijnen and van Dijken, 1992; Tijhuis *et al.*, 1993), or recently, using a semi-empirical relationship relating $\Delta G_{cat}$ to $\Delta G_{met}$ for different metabolic groups (Smeaton and Van Cappellen, 2018). Alternatively, $Y$ can be predicted directly using linear free energy relationships (Roden and Jin, 2011), or by applying optimization methods (Vallino, 2010; Algar and Vallino, 2014).

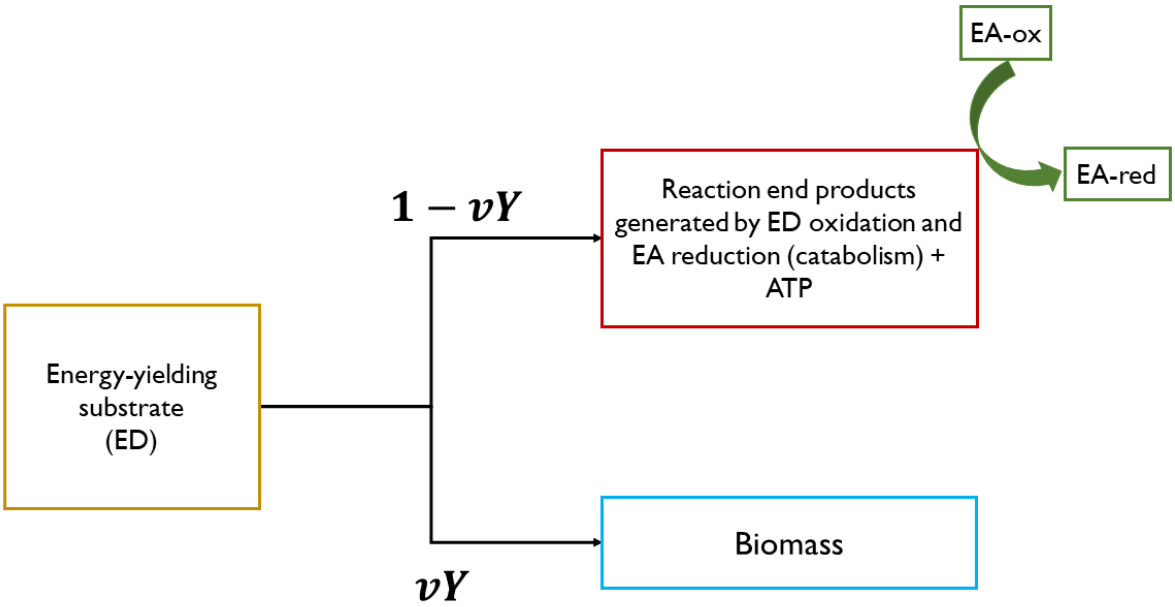

*Figure 1-3. Conceptual diagram illustrating the significance of the growth yield, Y. The diagram shows the allocation of an ED substrate to be oxidized by catabolism, or allocated to biomass.*

### 1.4.2 Geomicrobial kinetics

Monod-type kinetics (also called Michaelis-Menten kinetics) are the standard formulations used in RTMs to represent microbial reaction rates (Regnier *et al.*, 2005; Arora *et al.*, 2015). Monod-type kinetics relate the specific growth rate ($\mu$ [time$^{-1}$]) to the concentration of a growth-controlling substrate ($C_{ED}$ [mol ED l$^{-1}$]) via two parameters, the maximum specific growth rate ($\mu_{max}$ [time$^{-1}$]), and the half-saturation constant ($K_{ED}$ [mol ED l$^{-1}$]):

$$\mu = \mu_{max} * \frac{C_{ED}}{C_{ED} + K_{ED}} \tag{1-5}$$

Eq. 1-5 describes how the specific growth rate saturates at some ED substrate concentration, with the two parameters describing the maximum specific growth rate possible ($\mu_{max}$) and the concentration at which $\mu$ begins to saturate ($K_{ED}$). Equation 1-5 is the basis for relating geochemical conditions to microbially-controlled reaction rates. Two formulations are used to represent the influence of microbial biomass, the catalyst for these reactions, on the actual production or consumption rates (*i.e.*, "turnover" rates) of growth-controlling substrates (*e.g.*, $r_{ED}$ [mol ED (L time)$^{-1}$]).

In the first formulation, the concentration of biomass ($X$ [C-mol l$^{-1}$]) is explicitly included in the equation as a factor which impacts the rate of the reaction. The inverse of the growth yield ($Y$ [C-mol biomass (mol ED)$^{-1}$]) is used to represent the biomass-specific moles of substrate turnover, effectively converting the units of biomass concentration to units of ED concentration (Eq. 1-6):

$$r_{ED} = X * \frac{\mu_{max}}{Y} \frac{C_{ED}}{C_{ED} + K_{ED}} \tag{1-6}$$

where $r_{ED}$ is the rate of ED substrate utilization [mol ED (L time)$^{-1}$].

In the second formulation, an implicit maximum rate, $r_{max}$ (in units of [mol ED (L time)$^{-1}$]), is used instead (Eq. 1-7):

$$r_{ED} = r_{max} * \frac{C_{ED}}{C_{ED} + K_{ED}} \quad (1\text{-}7)$$

In low energy environments, reaction rates have the potential to be thermodynamically limited. This occurs when the energy yield from the Gibbs energy of metabolism is insufficient to generate ATP to be used for growth. Therefore, there is an energetic threshold such that when the Gibbs energy is below this threshold, growth is inhibited. In RTMs, representing this limit is accomplished using the thermodynamic potential factor, $F_T$ (Arora *et al.*, 2015). One formulation for this factor is (LaRowe *et al.*, 2012) :

$$F_T = \frac{1}{e^{(\frac{\Delta G_{met} + F\Delta\Psi}{RT})} + 1} \quad (1\text{-}8)$$

where F is the Faraday constant, [96485.34 coulomb mol$^{-1}$], $\Delta\Psi$ is the potential across a cell membrane [mV], R is the gas constant [8.314 J (K mol)$^{-1}$], and T is the temperature in Kelvin.

This $F_T$ term can be appended to Eq. 1-6 or 1-7 as a thermodynamic factor impacting the reaction rate. The thermodynamic potential factor is thus the second way that the Gibbs energy of metabolism enters into the representation of bioenergetic controls on growth and reaction rates in geomicrobial kinetics models.

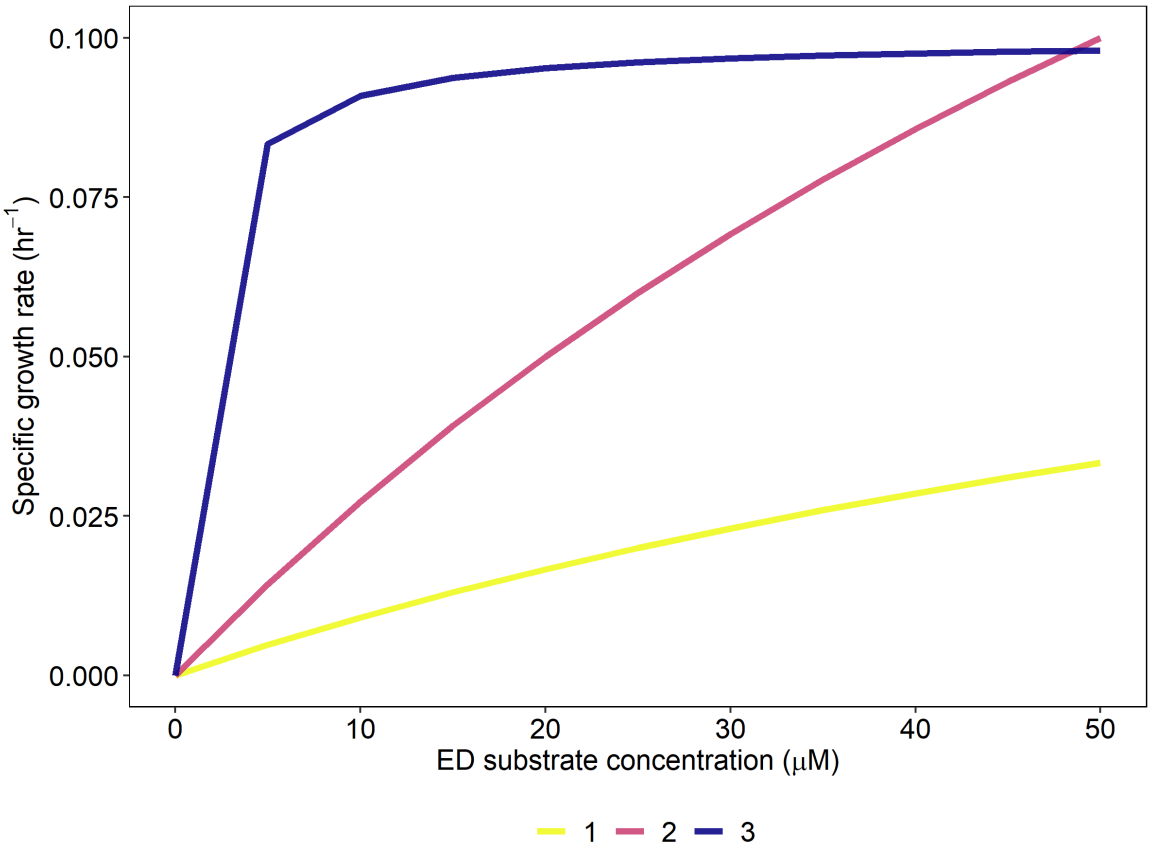


*Figure 1-4. Hypothetical specific growth rates versus the ED substrate concentration for three different combinations of Monod-type kinetic parameters. Lines 1 and 2 share the same $K_{ED}$ value, while lines 1 and 3 share the same $\mu_{max}$ value, with line 3 corresponding to the smallest $K_{ED}$ value and line 2 to the highest $\mu_{max}$ value.*

## 1.5 Biogeochemical implications of mixotrophy

Typically, carbon cycling in subsurface environments is assumed to be unidirectional, with microbial "soil respiration" degrading the organic carbon previously fixed by terrestrial plants and microorganisms to inorganic carbon, which can be returned to the atmosphere as carbon dioxide ($CO_2$). Under this assumption, subsurface microbial growth and activity is assumed to be organoheterotrophic. There is growing evidence in many environments that indicates that lithoautotrophic and mixotrophic metabolisms play a prominent role in subsurface ecosystems in terms of their relative abundance and contribution to ecosystem function (Kellermann *et al.*, 2012; Griebler and Avramov, 2015; Jewell *et al.*, 2016). With this metabolic capacity, subsurface prokaryotic communities are not only catalysts of carbon degradation, but are capable of inorganic carbon fixation and therefore they close the carbon cycle in the subsurface (Hutchins *et al.*, 2016).

Figure 1-5 illustrates the implications of mixotrophy for biogeochemical reaction dynamics. This conceptual diagram is largely informed by pure culture experiments that studied the metabolic flexibility of mixotrophs. The changes in carbon cycle fluxes, biomass assimilation of organic carbon, and electron acceptor turnover rates are shown as a function of the relative proportions of the organic and inorganic ED substrates that a mixotrophic organism consumes. With increasing relative utilization of the inorganic compound, autotrophic activity does not occur immediately, but instead begins at some threshold (as discussed in section 1.3.1). Prior to this threshold, microbial activity is heterotrophic (*i.e.*, uses only organic carbon for biomass synthesis). This sustained heterotrophic activity is matched by an increased assimilation of the organic compound for biomass C compared to growth on the organic compound alone. Consequently, the rate of inorganic C production decreases because the inorganic ED is being

oxidized for energy generation rather than the organic ED. At some point following the onset of autotrophic activity, there is a net consumption of inorganic C.

Mixotrophy impacts the overall turnover rate of electron acceptors such as nitrate, sulfate and iron(III) due to the different energetic efficiencies of autotrophic and heterotrophic metabolisms. Heterotrophic metabolisms require less energy to form organic biosynthetic molecules from existing organic compounds compared to autotrophic metabolisms which must fix inorganic C into organic molecules (Heijnen and van Dijken, 1992). Per unit of biomass produced, autotrophic metabolisms therefore need to run their catabolic reaction more times relative to heterotrophic metabolisms, making growth less efficient in terms of the total energy-yielding substrate (*i.e.*, electron donor or electron acceptor) that is consumed. Consequently, the biomass-specific electron acceptor turnover rates by autotrophic metabolisms are higher, that is, the amount of the electron acceptor consumed by catabolism per amount of biomass formed is higher. The overall turnover rates, however, are lower due to the impact of the less efficient growth of autotrophs on the overall turnover rate (*i.e.*, $r_{max}$ in Eq. 1-7 is the overall turnover rate, and can be compared to Eq. 1-6 to see the three parameters that are lumped into $r_{max}$, including the growth yield *Y*, which represents the growth efficiency) (Koenig and Liu, 2001; Watson *et al.*, 2003; Cardoso *et al.*, 2006; Handley *et al.*, 2013).

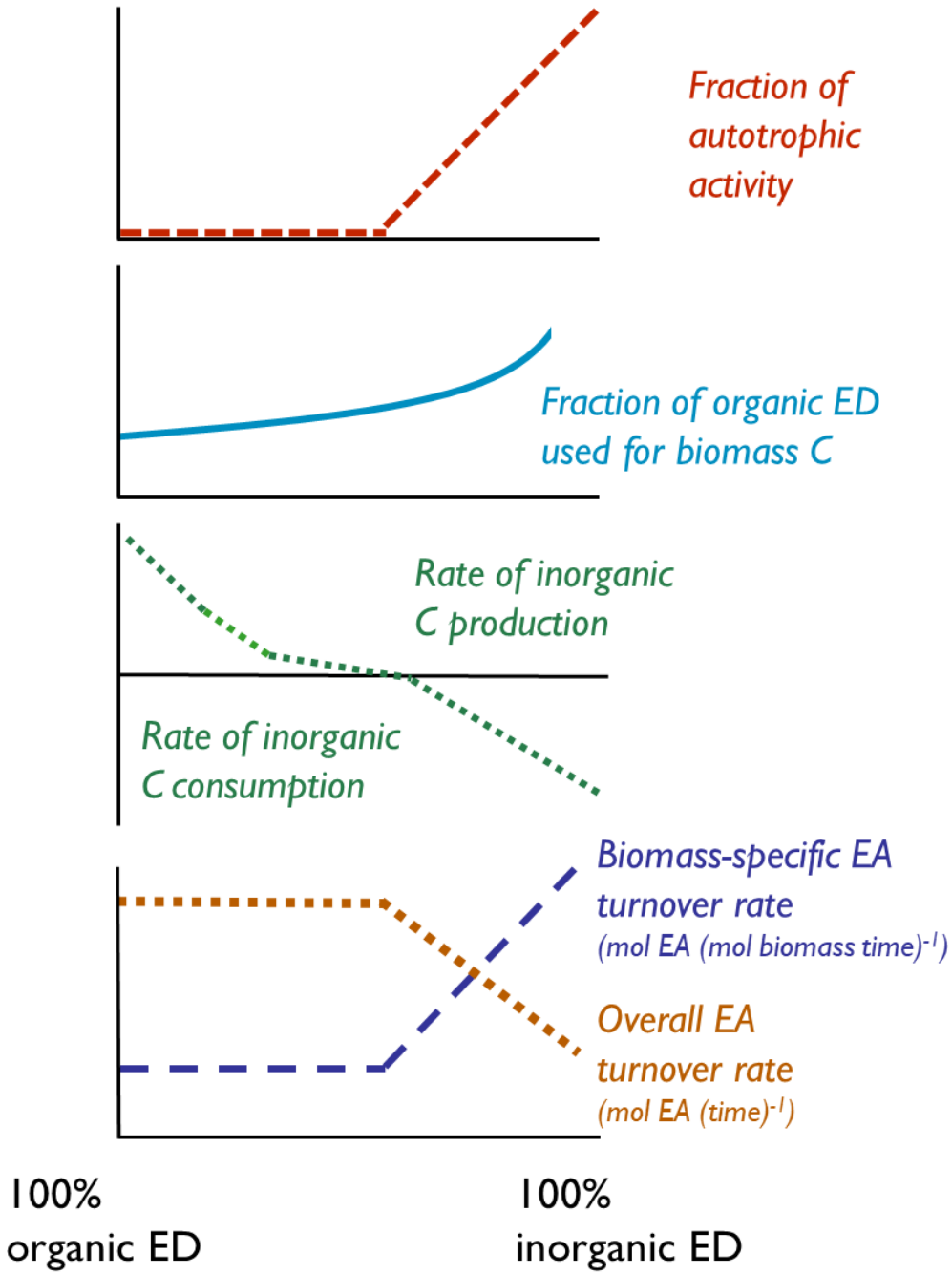


*Figure 1-5. Conceptual diagram illustrating the implications of mixotrophic metabolisms for the biogeochemical cycling of redox-active compounds. EA = electron acceptor substrate and ED = electron donor substrate.*

### 1.5.1 Accounting for mixotrophy in environmental models (RTMs)

Newman and Banfield (2002) summarize the major questions motivating research that seeks to improve representation of geomicrobial reactions using models:

> *"How do organisms self-organize in response to changes in their environment (both biological and chemical)? In turn, how does their organization affect the chemistry of their environment? What are the metabolic and genetic networks that link the members of the community to one another? And how robust are these networks in the face of environmental perturbations?"*

Mixotrophy involves important changes to the chemistry of an environment compared to organotrophy. In turn, the availability of alternative EDs in the environment determines whether mixotrophy is energetically desirable (Figure 1-5). This thesis seeks to build a modeling framework based on the "metabolic network" involved, in order to be able to represent the chemical controls on the metabolic flexibility of mixotrophy. This modeling framework can then be used to predict the response of mixotrophy to changes in environmental conditions, and to predict the turnover of environmentally-relevant chemicals.

Progress has been made in RTMs by using bioenergetics to more accurately represent growth yields and energetic limitations of reaction kinetics (*i.e.*, the $F_T$ term) (Arora *et al.*, 2015). A major challenge remaining in RTMs is accounting for when reactions are energetically favourable ($\Delta G_{cat} < 0$ , $\Delta G_{met} < 0$, and $F_T > 0$), but are not occurring, because some reaction is even more favourable. In a sense, this challenge represents a form of competition between multiple reactions for EA reduction, ED oxidation, or carbon source utilization reactions.

Modelling frameworks that integrate thermodynamic (*i.e.*, bioenergetic) and kinetic constraints using the formulations outlined in sections 1.4.1 and 1.4.2 have been successful in

more systematically representing switching between types of metabolisms other than those involved in mixotrophy. For example, Algar and Vallino (2014) used a bioenergetic-kinetic approach to predict the competition between nitrate reducing processes. Payn *et al.* (2014) used a bioenergetic-kinetic approach to represent the different energetic efficiencies (*i.e.*, growth yields) of autotrophic and heterotrophic metabolisms. However, these authors did not explicitly represent the progressive switching between all the metabolisms involved in mixotrophy.

### 1.6 Thesis objectives

The overall objective of this thesis is to describe the competition between heterotrophic versus autotrophic, and organotrophic versus lithotrophic metabolic activities in metabolically flexible chemotrophic microbial communities using a combined bioenergetic and kinetic approach. This approach is compatible with the formulations and level of detail typically implemented in reactive transport models. The specific objectives of the thesis are to (1) develop a conceptual model of mixotrophic growth informed by experimental datasets that describes the constraints on energy and carbon allocation among end member metabolisms, (2) apply this conceptual model into a bioenergetic-kinetic modeling framework that incorporates the existing Gibbs Energy Dynamic Yield Method (GEDYM, Smeaton and Van Cappellen, 2018) bioenergetics framework to predict the relative abundances of heterotrophy and autotrophy at steady state in experimental chemostat systems, and (3) apply the framework to predict the relative contribution of autotrophic and heterotrophic metabolisms to iron, nitrogen, and carbon cycling in a lake sediment.

# Chapter 2
# Mathematically representing chemosynthetic mixotrophy in biogeochemical models

## 2.1 Introduction

Chemosynthetic microorganisms play major roles in biogeochemical elemental cycling, thereby influencing nutrient and metal cycling and greenhouse gas fluxes (Long *et al.*, 2016). Outside the photic zone, organic compounds are typically assumed to be the primary carbon sources and electron donors (EDs) supporting microbial activity. That is, the metabolic activity of chemosynthetic communities is often closely regulated (or limited) by the supply and energy content of low molecular weight organic acids (*e.g.* acetate) (Gottschal and Dijkhuizen, 1988; Vallino *et al.*, 1996). In addition to serving as energy substrates, these organic compounds can also provide the carbon atoms needed for the synthesis of new biomass. Alternatively, inorganic carbon sources, most often $CO_2$, can be used for growth by autotrophic microorganisms. Carbon in $CO_2$, however, has an oxidation state greater than that of carbon in biomass, making it energetically costlier to incorporate into biomass.

Although chemoorganotrophs are usually assumed to dominate non-photosynthetic microbial communities, there is growing evidence of the significance of chemolithoautotrophy, sometimes called dark carbon fixation, in the biogeochemical reaction systems controlling the cycling of elements such as iron and sulfur (Alfreider *et al.*, 2003; Kellermann *et al.*, 2012; Griebler and Avramov, 2015; Herrmann *et al.*, 2015; Francois *et al.*, 2016; Jewell *et al.*, 2016). The corresponding chemolithoautotrophic metabolisms incorporate $CO_2$ into biomass using a variety of fixation pathways (Sato and Atomi, 2010), while acquiring energy from the oxidation of an inorganic ED, for example, methane ($CH_4$), ammonium ($NH_4^+$), nitrite ($NO_2^-$), sulfide ($S^{2-}$), thiosulfate ($S_2O_3^{2-}$), and dihydrogen ($H_2$). These inorganic compounds are generated by

processes such as mineral weathering (Yabusaki *et al.*, 2017; Dwivedi *et al.*, 2018) and organic matter fermentation (Lovley and Chapelle, 1995). The inclusion of autotrophic metabolisms in reactive transport models of subsurface environments has demonstratably improved the predictions of reaction rates associated with carbon, sulfur, iron and nitrogen cycling (Arora *et al.*, 2017; Yabusaki *et al.*, 2017; Dwivedi *et al.*, 2018). In environments where low concentrations of organic and inorganic electron EDs are available, the microbial community is likely to simultaneously utilize more than one carbon source, including $CO_2$, for growth, and more than one ED for energy generation. That is, these environments may support mixotrophic or facultative chemolithoautotrophic communities (Rittenberg, 1972; Matin, 1978; Dijkhuizen and Harder, 1984).

The chemical and biological controls on mixotrophic metabolisms have been fairly well studied in pure cultures by measurement of enzyme production, substrate utilization rates (*e.g.*, carbon fixation rates), and biomass concentrations, as examples. These experiments have demonstrated that during growth on mixtures of organic and inorganic ED substrates, growth is enhanced compared to growth on the organic substrate alone. This growth is related to the enhanced incorporation of the organic ED substrate into biomass. Accordingly, there is a threshold for the onset of autotrophy, where autotrophy is only possible once the relative rate of utilization of the inorganic ED is in sufficient excess that the metabolism is organic carbon-limited (Dijkhuizen and Harder, 1984). This behaviour highlights the importance of the competition between heterotrophic and autotrophic modes of metabolism during mixotrophic growth.

The regulation of metabolic functions and rates is closely linked to the generation and use of catabolic energy by cells, which forms the field of research known as bioenergetics. There are

only a few studies in which bioenergetic models have been applied in environmental simulations to account for the thermodynamic limitations on biogeochemical reaction rates (Payn *et al.*, 2014; Arora *et al.*, 2015). The potential co-occurrence of autotrophic and heterotrophic metabolisms as a function of (variable) environmental conditions needs to be acknowledged and more systematically represented in a bioenergetics framework. While it is possible to quantify the thermodynamic driving forces of metabolic reactions, many reactions may be thermodynamically favourable at the same time, but they may not all occur, because cells and communities strive to optimize the allocation of limiting resources, whether an electron donor or acceptor, an essential nutrient, or even habitat space (Arora *et al.*, 2015). In other words, we cannot assume that a community uses only organic carbon compounds for energy production and biomass growth, or that a given combination of carbon sources and energy substrates remains unchanging over time.

In this chapter, I develop a bioenergetics-based mathematical framework for representing mixotrophy in biogeochemical reaction systems. The derivation of this framework is inspired by recent work on the prediction of dynamic growth yields of microorganisms, the so-called Gibbs Energy Dynamic Yield method (Smeaton and Van Cappellen, 2018). It takes into account kinetic and thermodynamic constraints on the rates of the possible metabolic end members, under imposed chemo-static conditions.

**2.2 Conceptual model**

Chemosynthetic mixotrophic growth can be conceptualized as the combination of a set of three metabolic end member (MEM) reactions occurring simultaneously (Wood and Kelly, 1980; Gottschal and Thingstad, 1982; Perez and Matin, 1982; Lee *et al.*, 1985; Von Stockar *et al.*, 2011). These end member reactions represent unique combinations of an ED (and energy source) and carbon source used for growth. They are: organoheterotrophy (OH), lithoautotrophy (LA),

and lithoheterotrophy (LH). As section 2.2 described, OH uses organic carbon substrates as both an energy and carbon source, and LA uses inorganic substrates as an energy source and inorganic carbon for its carbon. LH, then uses an inorganic substrate for its energy, while using an organic carbon source.

The relative rates of these MEMs undertaken by a population of organisms at any time during growth on a mixture of an organic ED and inorganic ED are regulated by the relative utilization rates of the two EDs ($r_{inorg\ ED}$ and $r_{org\ ED}$). The relative expression of the three MEMs can be described as a fraction of the total mixotrophic biomass, $x_{ik}$, where $i$ is either $o$ or $l$ and used to represent organotrophy or lithotrophy, respectively, and $k$ is either $h$ or $a$ to represent heterotrophy or autotrophy, respectively. These MEM fractions can be related to $r_{inorg\ ED}$ and $r_{org\ ED}$ using expressions for the energy and carbon balances of the population. Figure 2-1 illustrates the conceptual model, showing the relationship between the utilization rates of the two EDs and the carbon and energy balances.

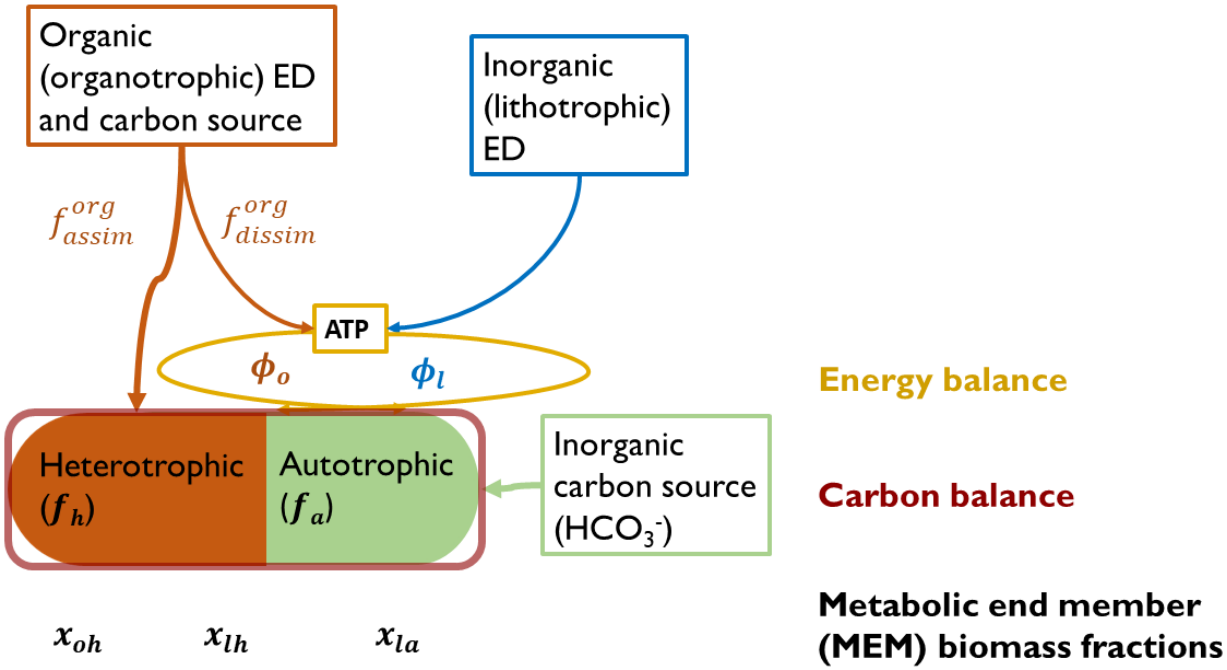


*Figure 2-1. Illustration of conceptual model of mixotrophic growth. The diagram shows how electron equivalents from the organic and inorganic electron donors are either allocated for use as a carbon source (incorporation into biomass) or for generating energy for biosynthesis or energy conservation in the anabolic reaction.* $f_{assim}^{org}$ *is the fraction of organic carbon assimilated into biomass, while* $f_{dissim}^{org}$ *is the fraction of organic carbon dissimilated (i.e., oxidized for energy during catabolism). The various fractions referred to in the text are labelled for clarification and to demonstrate how they are related to each other. The carbon and energy balance fractions are noted by symbols* $f_h$ *and* $f_a$ *for fractions of heterotrophy and autotrophy, respectively, and* $\phi_o$ *and* $\phi_l$ *for the fractions of organotrophy and lithotrophy, respectively. The metabolic end member (MEM) fractions are noted using* $x$*, with subscripts "oh" referring to organoheterotrophy, "lh" for lithoheterotrophy, and "la" for lithoautotrophy.*

### 2.2.1 Carbon and energy balances

Here, I outline the energy and carbon balance expressions for mixotrophic growth which describe the allocation of the two EDs and two carbon sources to the energy-requiring processes of biosynthesis and energy conservation, plus the carbon requirement for biosynthesis. The energy balance fractions represent the proportions of the overall metabolism that use the organic (*i.e.*, organotrophy) and inorganic (*i.e.*, lithotrophy) EDs for energy, while the carbon balance fractions represent the proportion of the biomass that is formed using organic (*i.e.*, heterotrophy) and inorganic (*i.e.*, autotrophy) carbon.

To compare the ED utilization rates in terms of the energy available, it is necessary to convert the rates from units of mole of ED to units of moles of electron equivalents (eeq). Electron equivalents represent the number of electrons ($e^-$) released during complete oxidation of the ED. For example, during the oxidation half reaction of thiosulfate ($S_2O_3^{2-}$), 8 $e^-$ are released:

$$S_2O_3^{2-} \rightarrow 2SO_4^{2-} + 8e^- \quad (2\text{-}1)$$

An eeq factor ($n_{eeq}^{ED}$) [mol eeq (mol ED)$^{-1}$] can be used to convert ED utilization rate units. For example, $r_{org\ ED}$ [mol org ED (L time)$^{-1}$] can be converted to $r_{org\ eeq}$ [mol org eeq (L time)$^{-1}$] using Eq. 2-2. These two notations for distinguishing rates in units of mol ED and mol eeq will be used throughout this thesis.

$$r_{org\ eeq} = r_{org\ ED} * n_{eeq}^{ED} \quad (2\text{-}2)$$

The total rate of ED utilization of the inorganic and organic substrates for processes requiring electron donation in both catabolism and anabolism ($r_{eeq}$)[mol eeq (L time)$^{-1}$] is the sum of the rates of consumption of the two EDs where the organic ED utilization rate is multiplied by the electron equivalents fraction of the organic ED dissimilated, $f_{dissim}^{org}$:

$$r_{eeq} = f_{dissim}^{org} * r_{org\ eeq} + r_{inorg\ eeq} \quad (2\text{-}3)$$

The fraction of the total metabolic reaction that is organotrophic ($\phi_{org}^{met}$) and lithotrophic ($\phi_{litho}^{met}$) can be calculated using each of the terms on the right side of Eq. 2-3 as the numerator and the total eeq utilization rate for energy production as the denominator:

$$\phi_{org} = \frac{f_{dissim}^{org} * r_{org\ eeq}}{r_{eeq}} \quad (2\text{-}4)$$

$$\phi_{litho} = \frac{r_{inorg\ eeq}}{r_{eeq}} \quad (2\text{-}5)$$

The carbon balance fractions are calculated using units of C-mol rather than units of mol eeq, as with the energy balance fractions. The total biomass production rate ($r_x$) [C-mol biomass (L time)$^{-1}$] reflects the use of organic (*i.e.*, heterotrophic) and inorganic (*i.e.*, autotrophic) carbon to build biomass and can therefore be expressed as the sum of the two rates of consumption of these carbon sources:

$$r_x = r_{x,het} + r_{x,auto} \quad (2\text{-}6)$$

whereby the total rate of heterotrophic microbial growth (*i.e.*, the OH and LH MEMs) ($r_{x,het}$) [C-mol biomass (L time)$^{-1}$] is:

$$r_{het,x} = f_{assim}^{org} * r_{org\ ED} * n_C^{org\ ED} \quad (2\text{-}7)$$

where $n_C^{org}$ is the number of moles of carbon in one mole of organic substrate, and is used to convert the organic ED utilization units to C-mol units, and $f_{assim}^{org}$ is the fraction of the organic substrate assimilated for biomass synthesis (and is equal to 1-$f_{dissim}^{org}$).

All inorganic carbon uptake is allocated to biomass synthesis and, given the 1:1 ratio of carbon in $CO_2$ and in a C-mol of biomass, the rate of biomass production attributed to autotrophy ($r_{x,auto}$) [C-mol biomass (L h)$^{-1}$] is equal to the rate of carbon dioxide uptake ($r_{CO_2}$) [C-mol (L h)$^{-1}$]:

$$r_{x,auto} = r_{CO_2} \tag{2-8}$$

The fraction of the total metabolism that is heterotrophic ($f_h$) and autotrophic ($f_a$) is described using:

$$f_h = \frac{r_{x,het}}{r_x} \tag{2-9}$$

$$f_a = \frac{r_{x,auto}}{r_x} \tag{2-10}$$

These metabolic carbon and energy balance fractions can be used to calculate the relative proportions of the MEMs. These MEM fractions represent the fraction of biomass, and therefore also total metabolic activity, that uses that MEM reaction. Given that there are three MEMs representing the unique combination of a carbon and energy source, the fraction of each MEM will be the product of a metabolic energy balance fraction ($\phi_i^{met}$) and a carbon balance fraction ($f_k$):

$$x_{ik} = \phi_i^{met} * f_k \tag{2-11}$$

### 2.2.2 Representing energetic constraints: Defining reaction stoichiometries

To apply this conceptual framework using a bioenergetic-kinetic approach, and represent the energetic constraints on each MEM, the Gibbs Energy Dynamic Yield Method (GEDYM) is used. This method uses the Gibbs energies of the anabolic (*i.e.*, biomass forming) and catabolic (*i.e.*, energy generating) reactions that make up the metabolic reaction to predict how they are

combined to yield the metabolic reaction. The details of deriving catabolic and anabolic reactions are described by Smeaton and Van Cappellen (2018). By calculating the bioenergetics-predicted metabolic reaction stoichiometry, the specific turnover rates of reactants and products can be calculated for each MEM.

As examples, the catabolic and anabolic reactions during lithoheterotrophic growth using thiosulfate ($S_2O_3^{2-}$) as an ED/ energy source, oxygen ($O_2$) as an electron acceptor, and acetate ($C_2H_3O_2^{\ -}$) as a carbon source are outlined here. The catabolic reaction describing the oxidation of $S_2O_3^{2-}\ to\ SO_4^{2-}$ coupled to the reduction of $O_2$ to $H_2O$, called lithotrophy would be:

$$S_2O_3^{2-} + 2O_2 + H_2O \rightarrow 2SO_4^{2-} + 2H^+ \qquad (2\text{-}12)$$

For the anabolic reactions describing the formation of biomass, the generic formula, $CH_{1.8}O_{0.5}N_{0.2}$, is used to represent one carbon mole of biomass. The anabolic reaction here involves the reduction of $C_2H_3O_2$ to the oxidation state of biomass coupled to the oxidation of $S_2O_3^{2-}\ to\ SO_4^{2-}$:

$$\begin{aligned} 0.15S_2O_3^{-2} + 0.5C_2H_3O_2^- + 0.2NH_4^+ + 0.27H_2O \rightarrow \\ 0.3SO_4^{-2} + 0.05HCO_3^- + 0.06H^+ + CH_{1.8}O_{0.5}N_{0.2} \end{aligned} \qquad (2\text{-}13)$$

These reactions can be used to calculate the standard state Gibbs energies, $\Delta G_{an}^{\circ}$ and $\Delta G_{cat}^{\circ}$ (using Eq. 1-1, and Eq. A-16 (Appendix A) to correct for temperature), and subsequently $\Delta G_{an}$ and $\Delta G_{cat}$ (using Eq. 1-2) given the chemical activities in the environment being simulated.

Smeaton and Van Cappellen (2018) present the principle equation of the GEDYM that is used to calculate growth yields and the energetic limitations to metabolic reactions. Its derivation

is reproduced in Appendix A. The method uses linear regressions specific to different metabolic groups with different energetic costs. Here, I use the linear regression parameters from the fit to the "majority of metabolisms" for heterotrophic metabolisms (*i.e.*, for the OH and LH MEMs). For autotrophic metabolisms, I use an unpublished linear regression that is meant to represent the energetic costs of reverse electron transport and inorganic carbon fixation. Reverse electron transport is used by many lithoautotrophs to generate the reducing equivalents necessary to reduce $CO_2$ to the oxidation state of biomass. The linear regression parameters for these two metabolic groups are given in Table A-4 (Appendix A). In addition to being able to calculate the growth yield ($Y$) for a metabolism given the energy available from the specific chemical activities in a given environment, the maximum potential growth yield can also be calculated using bioenergetics. The calculation for this maximum potential growth yield ($Y_{max}$) is also described in Appendix A.

MEM-specific rates of reactant or product turnover, including growth rates, can be calculated using these MEM-specific growth yields. The anabolic and catabolic reactions can be added together to yield the metabolic reaction using the energy balance relationship described by Eq. 1-3. This metabolic reaction describes the stoichiometric coefficients in front of all reactants and products and thus facilitates the conversion of ED utilization rates to the rate of interest. For example, to account for the total potential MEM-specific turnover rate of a substrate S ($r_{S,MEM}$), the general equation 2-14 can be used:

$$r_{S,MEM} = r_{ED} * \frac{n_S^{met}}{n_{ED}^{met}} \qquad (2\text{-}14)$$

where $n_S^{met}$ is the stoichiometric coefficient in front of a substrate, S in the metabolic reaction for that MEM [mol S (C-mol biomass)$^{-1}$], and $n_{ED}^{met}$ is the stoichiometric coefficient in front of the ED in the metabolic reaction [mol ED (C-mol biomass)$^{-1}$].

To account for the limitation of MEM turnover rates by their competition with other MEMs, I scale the total potential MEM-specific rate by energy balance or carbon balance fractions. For the OH MEM, the total potential rate is scaled by $\phi_o$, the fraction of organotrophy, to represent the fact that not all the $r_{org\ ED}$ consumed is used for organotrophic growth:

$$r_{S,OH} = \phi_o * r_{org\ ED} * \frac{n_S^{met}}{n_{ED}^{met}} \quad (2\text{-}15)$$

where $r_{S,OH}$ is the OH-specific turnover rate of substrate S.

For LH, and LA, the two lithotrophic metabolisms, all of the inorganic ED consumed is used for donating electrons, so to describe the partitioning of the ED to either of the two MEMs, the carbon balance fractions ($f_k$) can be used to scale the total potential rates of each MEM:

$$r_{S,MEM} = f_k * r_{ED} * \frac{n_S^{met}}{n_{ED}^{met}} \quad (2\text{-}16)$$

Therefore, for LH, Eq. A-28 becomes:

$$r_{S,LH} = f_h * r_{inorg\ ED} * \frac{n_S^{met}}{n_{ED}^{met}} \quad (2\text{-}17)$$

And for LA, Eq. A-28 becomes:

$$r_{S,LA} = f_a * r_{inorg\ ED} * \frac{n_S^{met}}{n_{ED}^{met}} \quad (2\text{-}18)$$

To calculate MEM-specific growth rates (*i.e.*, $r_{x,OH}$, $r_{x,LH}$, and $r_{x,LA}$) , the same equations can be used, with $\frac{n_S^{met}}{n_{ED}^{met}}$ replaced by $Y_{ik}$, the potential growth yield (in units of [C-mol biomass (mol ED)$^{-1}$] for that specific MEM. The total mixotrophic substrate turnover rate or growth rate can then be calculated as the sum of these MEM-specific rates:

$$r_x = \phi_o * r_{org\ ED} * Y_{oh} + r_{inorg\ ED} * (f_h * Y_{lh} + f_a * Y_{la}) \quad (2\text{-}19)$$

To validate my modeling framework for predicting the relative abundances of the MEMs expressed as a function of the relative utilization of the two EDs, I collected data from chemostat studies identified in the literature which directly traced the fraction of the organic ED/ carbon source assimilated ($f_{assim}^{org}$), enabling the calculation of the MEM fractions using the conceptual model illustrated in Figure 2-1.

**2.3 Literature experimental data compilation**

Chemostats are ideal experimental systems to study mixotrophy, because they allow organisms to grow under stable, steady state conditions, simulating environmental conditions. Consequently, organisms grow in a constant physiological state, such that growth yields and kinetic parameters (such as $r_x$) are more precise and reproducible than those extracted from batch experiments (Kovarova-Kovar and Egli, 1998). Moreover, the supply rates of different ED and carbon source mixtures can be tightly controlled in chemostats.

In chemostats, sterile growth medium is supplied at a constant volumetric flow rate (*F*) to a culture vessel containing microorganisms (*e.g.*, Esteve-Núñez *et al.*, 2005). Biomass-containing effluent is removed from the vessel at the same flow rate to maintain a constant culture volume (*V*). The residence time of the cells in the reactor is given by the dilution rate (*D*) [time$^{-1}$] (Herbert et al, 1956) (Eq. 2-20). At steady state, the specific growth rate of the organisms, $\mu$, is equal to $D$.

$$D = \frac{F}{V} \tag{2-20}$$

Literature chemostat studies were chosen that used biochemical techniques (*e.g.*, isotopic labelling, tracking $CO_2$ gas production, and measurement of specific $CO_2$ fixation rates) to track

the proportion of organic substrate assimilated and used for biosynthetic molecules ($f_{assim}^{org}$) versus the fraction dissimilated for biomass synthesis and energy conservation ($f_{dissim}^{org}$). These studies also reported measurements that could be used to calculate $r_{org\ ED}$, $r_{inorg\ ED}$, and $r_x$. While studies that fit all the above criteria are sparse, these data enable fully constraining the energy and carbon balances described in section 2.2.1 to calculate the fraction of each MEM. Three published chemostat studies which investigated mixotrophic pure cultures grown on mixtures of organic and inorganic EDs were identified. Table 2 summarizes the experimental conditions of each study.

Briefly, all chosen studies used $O_2$ as the sole electron acceptor. Study 1 examined mixotrophic growth of *Paracoccus versutus* (formerly known as *Thiobacillus A2* and *Thiobacillus versutus)* (Katayama *et al.*, 1995) on the organic ED acetate and the inorganic ED thiosulfate (Gottschal and Kuenen, 1980). The catabolic and anabolic reactions for study 1 are in Table A-1 (Appendix A). In study 2, *Pseudomonas oxalaticus* was grown on mixtures of acetate and formate. While formate is an organic compound, it is treated as an "inorganic" substrate for the purposes of this synthesis since *P. oxalaticus* is unable to use formate as a C source for biomass, and its growth on formate is therefore exclusively autotrophic (Dijkhuizen *et al.*, 1977b). In other words, no formate is assimilated for forming biomass, which is the same for lithoautotrophic growth using a true inorganic compound such as $H_2$. While some papers have called autotrophic growth where formate or other one carbon acids such as methanol are used as the ED either organoautotrophic or methylotrophic (Dijkhuizen and Harder, 1984; Bowien *et al.*, 1996), it is herein referred to as lithoautotrophic. Studies 2 and 3 are nearly identical (*i.e.*, same organism, inorganic ED and electron acceptor), with the only difference being that in study 3 the

organic ED substrate is oxalate. The anabolic and catabolic reactions corresponding to studies 2 and 3 are found in Appendix A, Tables A-2 and A-3.

*Table 2-1. Description of experimental datasets available that examined mixotrophic growth on variable ratios of organic and inorganic ED substrate.*

| Study no. | Reference | Organism | Temperature (°C) | Organic ED | Inorganic ED | Electron acceptor | Specific growth rate ($h^{-1}$) | % Autotrophy determined by |
|---|---|---|---|---|---|---|---|---|
| 1 | (Gottschal and Kuenen, 1980) | *Paracoccus versutus* | 28 | Acetate | Thiosulfate | Oxygen | 0.05 | Acetate assimilation (gas production and $^{14}C$-labelling) |
| 2 | (Dijkhuizen *et al.*, 1980) | *Pseudomonas oxalaticus* | 28 | Acetate | Formate | Oxygen | 0.1 | Cell-specific carbon fixation rate |
| 3 | (Dijkhuizen and Harder, 1979) | *Pseudomonas oxalaticus* | 28 | Oxalate | Formate | Oxygen | 0.1 | Cell-specific carbon fixation rate |

### 2.3.1 Calculating the net ED utilization and growth rates

The concentrations of ED substrates supplied ($C_{ED}^{supplied}$) [mol ED (L)$^{-1}$] and the steady state residual concentrations ($C_{ED}^{residual}$) [mol ED (L)$^{-1}$] of ED substrates in the chemostat studies are used to calculate the net rates of organic and inorganic ED utilization ($r_{ED}$ ) [mol ED (L time)$^{-1}$] using Eq. 2-21. As described in Eq. 2-2, this rate can be converted to units of mol eeq using the eeq factor, $n_{eeq}^{ED}$.

$$r_{ED} = D \cdot (C_{ED}^{supplied} - C_{ED}^{residual}) \quad (2\text{-}21)$$

For the studies considered here, the residual concentrations were reported as not detectable, so that the ED utilization rates are equivalent to rate of ED supply at the chemostat inlet. For energetic calculations, the residual concentrations of the EDs were estimated using calculations that are outlined in Appendix A.

The total biomass concentrations ($X_{tot}$) measured at the outlet of the chemostat and reported in the studies in either [g of biomass C (L)$^{-1}$] or [g of dry weight biomass (L)$^{-1}$] were converted to units of [C-mol biomass (L)$^{-}$1] by multiplying them by the molecular weight of carbon (12.01 g (mol)$^{-1}$) or the average molecular weight of biomass (24.6 g (C-mol biomass)$^{-1}$ (Smeaton and Van Cappellen, 2018)), respectively. The total biomass production rate ($r_x$) [C-mol biomass (L time)$^{-1}$] was determined using:

$$r_x = X_{tot} * D \quad (2\text{-}22)$$

### 2.3.2 Calculating the MEM fractions

In the selected studies, two different approaches were used to monitor inorganic carbon fixation activity versus heterotrophic organic carbon use. In study 1, $f_{assim}^{org}$ was measured directly by

either tracing the $CO_2$ produced by organic substrate oxidation or by tracing the carbon allocated to biomass using an isotopic label (Gottschal and Kuenen, 1980). Along with the calculated growth rates and ED substrate utilization rates (described in section 2.31), this enabled the calculation of the carbon and energy balances as described in section 2.2.1, and therefore the calculation of the MEM fractions (using Eq. 2-9).

While $f_{assim}^{org}$ was not directly measured in studies 2 and 3, the carbon fixation rate was measured and could be used to determine the fractions of autotrophy ($f_a$) and heterotrophy ($f_h$). This is accomplished by comparing the biomass production ($r_{tot\,x_{100}}$) and carbon fixation ($r_{CO2_{100}}$) rates under 100% autotrophic conditions (*i.e.*, no added organic carbon) to the biomass production ($r_{tot\,x}$) and carbon fixation ($r_{CO2}$) rates of chemostat experiments containing organic carbon using:

$$\frac{f_a}{f_{a_{100}}} = \frac{\frac{r_{CO2}}{r_x}}{\frac{r_{CO2_{100}}}{r_{x_{100}}}} \tag{2-23}$$

At 100% autotrophy, $f_{a_{100}}$ = 1, therefore:

$$f_a = \frac{r_{CO2}/\,r_x}{r_{CO2_{100}}/\,r_{x_{100}}} \tag{2-24}$$

The fraction of heterotrophy, $f_h$ can thus be determined given that $f_h = 1 - f_a$.

Given that biomass-specific carbon fixation rates were reported in studies 2 and 3 (*i.e.*, per units biomass; [nmol-$CO_2$ $min^{-1}$ mg dry $weight^{-1}$]), this effectively accounts for normalizing the rate by biomass, and thus Eq. 2-25 was used:

$$f_a = \frac{q_{CO2}}{q_{CO2_{100}}} \tag{2-25}$$

where $q_{CO2}$ is the specific rate of $CO_2$ fixation for the conditions of interest, and $q_{CO2_{100}}$ is the specific rate of $CO_2$ fixation for the 100% autotrophy conditions, both in units of nmol-$CO_2$ $min^{-1}$ mg dry $weight^{-1}$. After the fraction of autotrophy is calculated, the fraction of the organic substrate assimilated can be calculated by rearranging Eq. 2-7, and $f_{dissim}^{org}$ can also be calculated since it is equal to 1 – $f_{assim}^{org}$. The carbon and energy balances and MEM fractions can then be calculated as described in section 2.2.1.

### 2.3.3 Comparing data-derived and GEDYM-predicted growth yields

Given the importance of the value of $Y$ for accurately predicting substrate turnover rates (*e.g.*, Fig. 1-3) (Smeaton and Van Cappellen, 2018), I sought to (1) derive the experimental observed $Y$ values for each MEM (*i.e.*, $Y_{ik}$), and use these values to (2) validate the use of a bioenergetics-based $Y$ prediction method (GEDYM).

To determine $Y_{ik}$ from the literature experimental data, we assume that all three MEMs (OH, LA and LH) were present in the chemostats. In cases when only the organic ED substrate is used (*i.e.*, 100% OH) or only the inorganic ED is used (*i.e.*, 100% LA), these growth yields ($Y_{ik}$, either $Y_{oh}$ or $Y_{la}$ [C-mol biomass (mol ED)$^{-1}$]) are calculated using:

$$Y_{ik} = \frac{r_x}{r_{ED}} \tag{2-26}$$

We assume that these represent the value of $Y_{oh}$ and $Y_{la}$ for the other ED mixture scenarios. Since the total mixotrophic growth rate is the sum of the MEM-specific growth rates (Eq. 2-19), this relationship can be rearranged to solve for $Y_{lh}$ when all the other values are known, which is possible using the datasets considered here, since I assume that the values of $Y_{oh}$ and $Y_{la}$ are fixed at the values that I calculated using Eq. 2-25 above:

$$Y_{lh} = \frac{r_x - \phi_o \cdot r_{org\ ED} \cdot Y_{oh} - f_a \cdot r_{inorg\ ED} \cdot Y_{la}}{f_h \cdot r_{inorg\ ED}} \quad (2\text{-}27)$$

To calculate the total observed Y values in units of C-mol biomass/ mol-$O_2$, Eq. 2-28 was used. The electron acceptor, $O_2$, is used as the denominator for the units of the growth yield since it is the one shared substrate among all three MEMs. The term $r_x \cdot n_{eeq}^x$ is substracted from the total moles of eeq generated by the two EDs to represent the moles of eeq that are allocated to biomass synthesis rather than catabolism. $n_{eeq}^x$ is 4.2 mol eeq (C-mol biomass)$^{-1}$. $n_{eeq}^{O_2}$ (4 mol eeq (mol $O_2$)$^{-1}$) is then used to convert the units from eeq to mol $O_2$.

$$Y_{ik} = \frac{r_x}{\left(r_{org\ ED} + r_{inorg\ ED} - r_x * n_{eeq}^x\right) * n_{eeq}^{O_2}} \quad (2\text{-}28)$$

where the units of $r_{org\ ED}$ and $r_{inorg\ ED}$ are [mol e-eq ED (L time)$^{-1}$].

All data-derived $Y$ values are herein referred to as observed $Y$ values. Appendix A and section 2.2.2 describe how the GEDYM is used to predict growth yields from chemical activities. Appendix A also describes how I calculated the residual concentrations of the reactants and products, from which their chemical activities could be calculated by modeling each growth medium using PHREEQC (Parkhurst and Appelo, 2013). The total GEDYM-predicted growth yield was calculated by multiplying each of the MEM-specific predicted growth yields (in units of C-mol biomass (mol $O_2$)$^{-1}$) by the fraction of that MEM ($x_{ik}$) observed (*i.e.*, calculated using Eq.2-11).

Figure 2-3 shows parity plots of the observed versus predicted $Y$ values for all three MEMs, and for the total $Y$ values**.** The $Y$ values in the parity plots for the OH and LA MEMs lay close to the 1:1 line; thereby demonstrating that GEDYM can be applied to represent these two MEMs. This demonstrates that the GEDYM linear regression parameters used for autotrophy accurately capture the energetic costs involved during autotrophy, including reverse electron

transport. However, the parity plot for the LH MEM shows that GEDYM is less accurate. A potential reason for the discrepancy is that the steady state concentrations of the reactants and products in the chemostats are not actually known but are instead estimated. The GEDYM is sensitive to these steady state concentrations since they affect the reaction quotient and therefore represent the distance of the metabolic growth reaction from equilibrium. Another potential reason for the lack of agreement is due to possible experimental errors. The total mixotrophic growth yields are predicted relatively well using the GEDYM (Figure 2-2), with some deviation from the 1:1 parity line which can be attributed in part to experimental error.

### 2.3.4 Bioenergetic controls on $Y$ values

The MEM-specific growth yields, $Y_{ik}$, were calculated using the GEDYM and plotted as a function of the relative utilization rate of the inorganic ED (in units of eeqs, as a fraction of the total eeqs consumed from both EDs) (Figure 2-3). The total observed growth yields in units of C-mol/ mol $O_2$ were calculated using Eq. 2-28. Figure 2-3 demonstrates the implications of the competition between autotrophy and heterotrophy for the total mixotrophic growth yield, and therefore for the turnover of substrates by mixotrophy. Heterotrophic growth yields are greater than autotrophic growth yields, and the transition between the OH MEM and LA MEM at relative rates of the inorganic ED consumed of 0 and 1, respectively, is not linear. Instead, the existence of two phases of mixotrophic growth (*i.e.*, heterotrophy and autotrophy, or energy-limited and organic carbon-limited) leads to a trend in the total growth yield that deviates from being linear, due to the presence of three rather than two MEMs. Figure A-4 shows the trends in the Gibbs energies of catabolism, anabolism, and metabolism that were used to calculate these growth yields. These figures demonstrate the need to account for all three MEMs to describe the energetics and metabolic behaviour of mixotrophic growth.

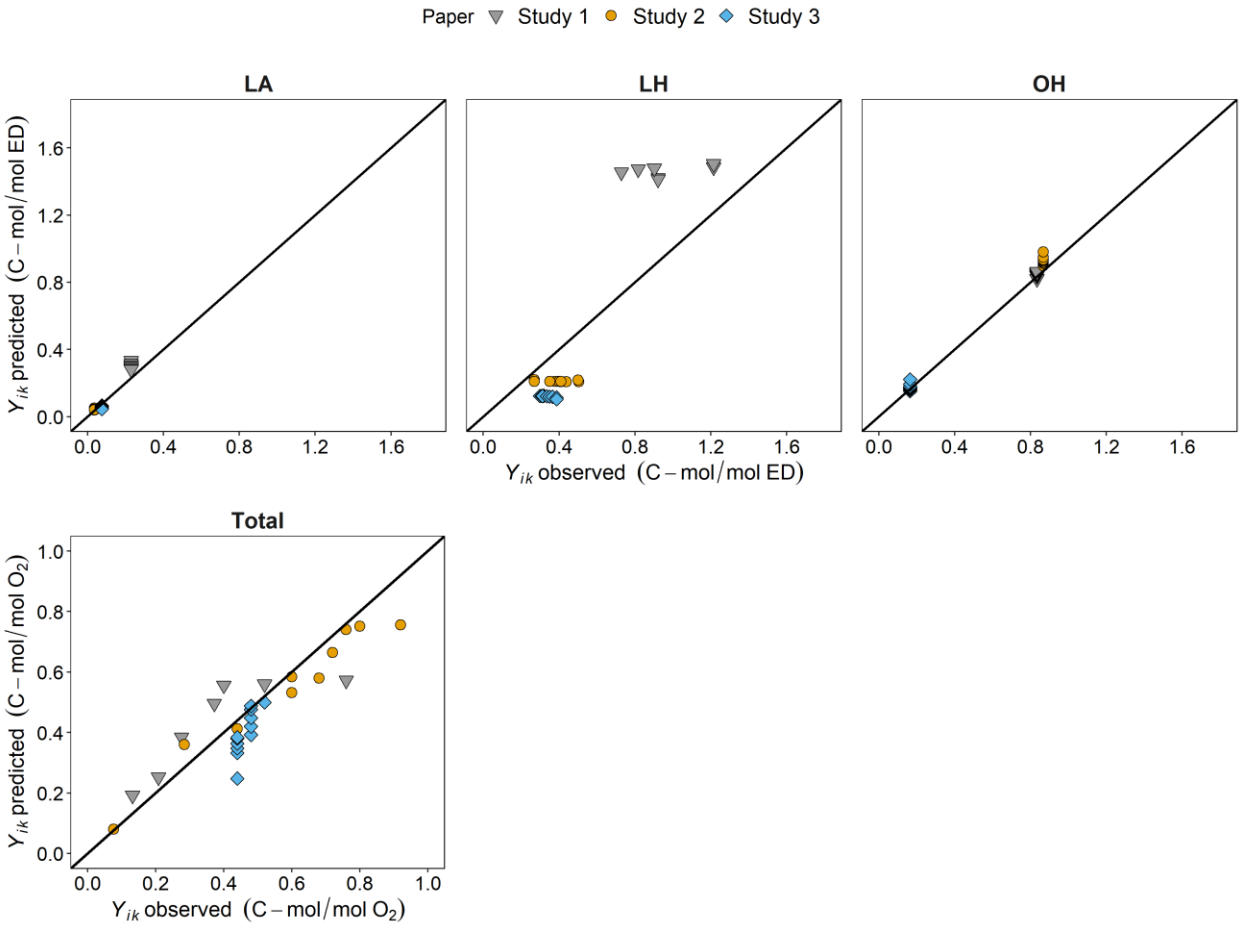


*Figure 2-2. Parity plots of observed and predicted yields in C-mol biomass/ mol ED for the 3 individual MEMs as indicated by subplot header (where LA= lithoautotrophy, LH= lithoheterotrophy, OH= organoheterotrophy), and for the total yield calculated as the sum of the three predicted yields, in units of C-mol biomass/ mol $O_2$.*

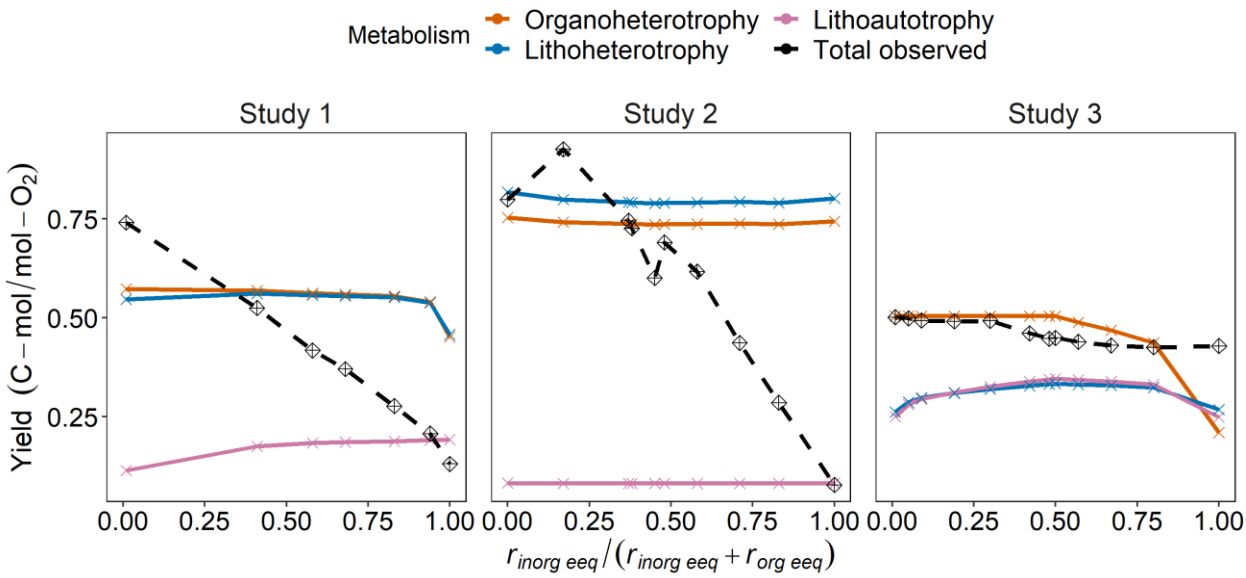


*Figure 2-3. Total calculated mixotrophic growth yield, Y, and MEM-specific growth yields versus the fraction of inorganic electron equivalents consumed , $r_{inorg\ eeq}/(r_{inorg\ eeq} + r_{org\ eeq})$. The identities of study 1, 2 and 3 are described in the text and in table 2-1.*

### 2.3.5 Trends in the data-derived MEM fractions, $f_h$, $f_a$ and $f_{org}^{assim}$

Figure 2-4-A shows the trends in the MEM fractions ($x_{ik}$), and therefore also the fractions of heterotrophy and autotrophy ($f_h$ and $f_a$, since $f_h = x_{oh} + x_{lh}$ and $f_a = x_{la}$) as a function of the relative utilization rate of the inorganic ED. Figure 2-4-B shows the fraction of the organic ED assimilated, demonstrating the relationship between the fraction of the organic ED assimilated and the fraction of heterotrophy (which is also described mathematically by Eqs. 2-5 and 2-7). Effectively, it shows that autotrophic activity (indicated by the relative fraction of the LA MEM in panel A) occurs at some threshold rather than at the point that the inorganic ED is first consumed. This is due to the extended occurrence of heterotrophy which is facilitated by the LH MEM, and is reflected in the increased assimilation of the organic ED.

In the biotechnology literature, this behaviour has been described by identifying two phases of growth. The phase when the metabolism is still 100% heterotrophic has been called the energy-limited phase of mixotrophic growth (Gommers *et al.*, 1988). Correspondingly, the phase of growth when autotrophy is occurring is the organic carbon-limited phase. These two phases of growth are classified in the same way as the limitations to growth on single organic ED substrates (Linton and Stephenson, 1978; Vallino *et al.*, 1996). In the geomicrobiology literature, this behaviour has been called the "energetic advantage" of mixotrophic growth, since the supply of the auxiliary ED helps to overcome the energetic limitations of growth on the single organic substrate alone (Gottschal and Kuenen, 1980; Muehe *et al.*, 2009; Chakraborty *et al.*, 2011).

### 2.3.6 Bioenergetic controls on the upper and lower bounds to $f_{org}^{assim}$

For all three studies, the relative fractions of the three MEMs (and $f_h$, $f_a$, and $f_{assim}^{org}$) are regulated in similar ways by the relative utilization rates of the organic and inorganic EDs (Figure 2-4). This validates the conceptual model outlined in section 2.3. The observed fractions

of the MEMs do differ among the three studies, however. Specifically, the onset of autotrophy occurs at different eeq fractions of the inorganic ED consumed. This is attributed to the differences in the oxidation state of the organic EDs. Organic ED substrates for which the oxidation state of the carbon atoms is further from that of biomass carbon atoms (*e.g.*, oxalate) are considered more energy-limited than those with an oxidation state closer to that of biomass (*e.g.*, acetate). These more energy-limited compounds require more energy to reduce the carbon atoms to the oxidation state of biomass carbon. They are therefore less advantageous to use as carbon sources, and the onset of autotrophy during mixotrophic growth on mixtures of that organic ED and some inorganic ED occurs at values of lower eeq fractions of the inorganic ED consumed, $r_{inorg\ eeq}/(r_{inorg\ eeq} + r_{org\ eeq})$ (compare study 3, which used oxalate as an organic ED and carbon source, to studies 1 and 2, which used acetate).

100% assimilation of the organic substrate is never reached (Figure 2-3-B), which demonstrates that there is an upper limit to the fraction that can be assimilated. This theoretical maximum yield ($Y_{max}$) is the yield calculated when $\Delta G_{met}$ is set to zero (Smeaton and Van Cappellen, 2018) (Appendix A). The values of $Y$ and $Y_{max}$ for the organoheterotrophic metabolism, calculated as described in Appendix A using GEDYM, are shown in the figure to demonstrate that these are the bounds on the fraction of the organic substrate assimilated. The organoheterotrophic $Y$ is the lower bound for $f_{assim}^{org}$ since these variables are equal during organoheterotrophic growth on a single carbon substrate (when $Y$ is in units of mol eeq biomass (mol eeq ED)$^{-1}$).

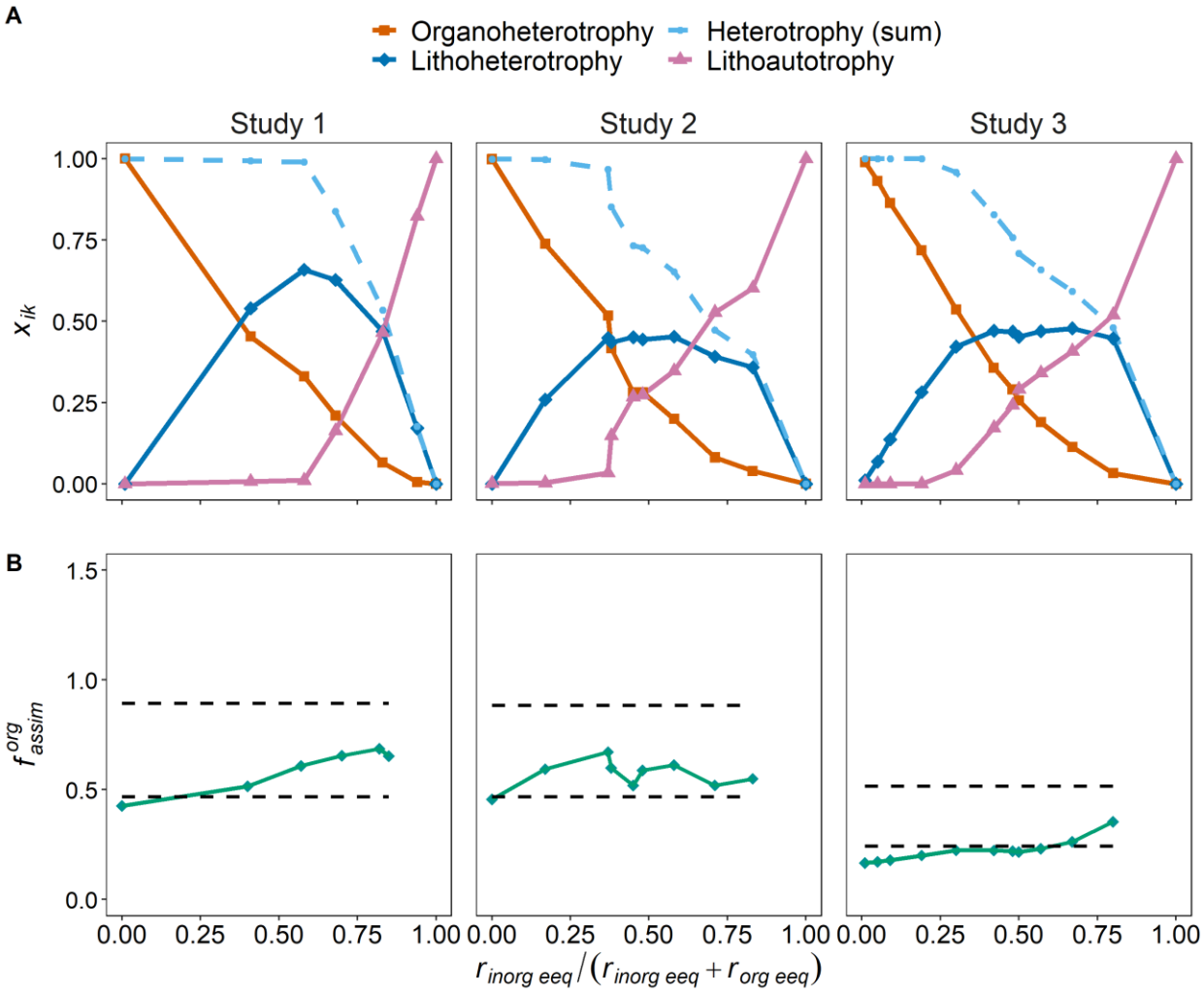


*Figure 2-4. Data-derived fractions of three MEMs observed ($x_{ik}$), $f_h$ and $f_{org}^{assim}$ as a function of the fraction of inorganic electron equivalents consumed, $r_{inorg\ eeq}/(r_{inorg\ eeq}+r_{org\ eeq})$. Panel A: Fractions of the three MEMs observed ($x_{ik}$) and fraction of heterotrophy observed (i.e., $f_h$, the sum of the OH and LH MEMs). Panel B: Calculated fraction of the organic ED assimilated ($f_{assim}^{org}$, dark green line and points), with GEDYM-predicted $Y$ and $Y_{max}$ of the OH MEM indicated (black dashed lines, with upper line being $Y_{max}$). The identities of studies 1, 2 and 3 are specified in section 2.4 of the text.*

## 2.4 Applying the conceptual model: A modeling framework for mixotrophy

A system of governing equations to predict the MEM fractions was developed using the conceptual framework built in the preceding sections. The system of equations relates the MEM fractions, $x_{oh}$, $x_{lh}$ and $x_{la}$, and the fraction of the organic ED/ carbon source dissimilated, $f_{dissim}^{org}$ to the utilization rates of the EDs ($r_{inorg\ eeq}$ and $r_{org\ eeq}$), and the GEDYM-predicted growth yields of the three MEMs ($Y_{ik}$) for a steady state chemostat system. The equations effectively represent the kinetic (*i.e.*, ED utilization rates) and thermodynamic (*i.e.*, growth yields) constraints on the expression of the three MEMs. The purpose of developing this modeling framework is that it can be implemented in larger kinetic reaction models where the MEM fractions can be calculated at each time step as a function of the changing utilization rates of the two EDs, changes in the growth yields, and/ or other limitations. The inputs are the net utilization rates of the two ED substrates, and the chemical environment-specific growth yields of the three MEMs.

### 2.4.1 System of equations

The first constraint describes how the three MEM fractions must sum to unity:

$$x_{oh} + x_{lh} + x_{la} = 1 \tag{2-29}$$

The second constraint is derived from the energy balance expression for the fraction of lithotrophy. It specifies that the two lithotrophic MEMs, $x_{lh}$ and $x_{la}$, must combine to equal the fraction of the total metabolic reaction that is lithotrophic ($\phi_{litho}^{met}$) by imposing:

$$\phi_{litho}^{met} = x_{lh} + x_{la} \tag{2-30}$$

This can be expressed in terms of ED utilization rates and MEM fractions only by substituting Eqs. 2-5 and 2-3 into Eq. 2-30:

$$\frac{r_{inorg\ eeq}}{r_{inorg\ eeq} + r_{org\ eeq} * f_{dissim}^{org}} = x_{lh} + x_{la} \tag{2-31}$$

The third constraint is derived from the carbon balance and describes the relationship between the two MEM fractions that use organic carbon (*i.e.*, the two heterotrophic fractions, $x_{oh}$ and $x_{lh}$) and the fraction of the organic ED assimilated. Eq. 2-7 can be rearranged with substitution of a rearranged Eq. 2-9 to relate $f_{assim}^{org}$ to $f_h$, the total growth rate, and the utilization rate of the organic ED/ carbon source:

$$f_{assim}^{org} = f_h \cdot \frac{r_x}{r_{org\ ED} \cdot n_C^{org\ ED}} \tag{2-32}$$

The fraction of heterotrophy is equal to the sum of the two heterotrophic MEM fractions:

$$f_h = x_{oh} + x_{lh} \tag{2-33}$$

while the total growth rate can be expressed in terms of the three MEM growth yields ($Y_{ik}$) (Eq. 2-19) and the two ED utilization rates ($r_{ED}$), as in Eq. 2-19. Substituting Eqs. 2-33 and 2-19 into 2-32 and replacing $f_{assim}^{org}$ with 1- $f_{dissim}^{org}$ gives the third constraint:

$$1 - f_{dissim}^{org} = (x_{oh} + x_{lh}) \cdot \frac{(\phi_o \cdot r_{org\ ED} \cdot Y_{oh} + r_{inorg\ ED} \cdot (f_h \cdot Y_{lh} + f_a \cdot Y_{la})}{r_{org\ ED} \cdot n_C^{org\ ED}} \tag{2-34}$$

The fourth and final constraint is taken from the expression for calculating $x_{oh}$ (from the general Eq. 2-11). Eq. 2-26 substituted for $f_h$, while $\phi_o$is expressed in terms of the two ED utilization rates, $r_{org\ ED}^{met}$ and $r_{inorg\ ED}^{met}$, and $f_{dissim}^{org}$, as in the energy balance expression for $\phi_o$ (Eq. 2-3 and Eq. 2-4), giving the final constraint:

$$x_{oh} = (x_{oh} + x_{lh}) \cdot \left[\frac{f_{dissim}^{org} \cdot r_{org\ eeq}}{f_{dissim}^{org} \cdot r_{org\ eeq} + r_{inorg\ eeq}}\right] \tag{2-35}$$

These constraints (Eqs. 2-29, 2-31, 2-34, 2-35) describe how energy is allocated within mixotrophic populations as a function of the utilization rates of the two EDs and the growth yields of the three MEMs on their respective EDs.

In addition to the constraints, the solver used to implement the system of equations allows for the specification of lower and upper bounds to the unknown variables. These bounds describe the range of values that the solver guesses for, and therefore represent the range of values that are possible for that variable. Values of 0 and 1 are imposed as the lower and upper bounds, respectively, of the variables $x_{oh}$, $x_{lh}$, and $x_{la}$. As discussed in section 2.3.6, the lower and upper bounds for the value of $f_{dissim}^{org}$ can be described using the values of $Y_{oh}$ and $Y_{max}$ of the OH MEM calculated using the GEDYM. Therefore, for the variable $f_{dissim}^{org}$, the lower and upper bounds specified are 1-$Y_{max}$ and 1-$Y_{oh}$. These values can both be calculated using the GEDYM for the specific chemical conditions and organic compound.

### 2.4.2 Implementation

The ability of the four constraints, or the non-linear system of governing equations, to accurately predict MEM fractions ($x_{oh}$, $x_{lh}$, and $x_{la}$) and the fraction of the organic ED/carbon source assimilated ($f_{assim}^{org}$) were tested using the three compiled literature datasets. During computation (see Section 2.4.3 for more details), $x_{oh}$, $x_{lh}$, $x_{la}$ and $f_{dissim}^{org}$ are the only unknowns and the rest of the parameters are calculated as described in the previous sections. Accordingly, the values of the net ED utilization rates ($r_{org\ ED}$ and $r_{inorg\ ED}$) were determined using Eq. 2-21.

The values of $Y_{oh}$, $Y_{lh}$, and $Y_{la}$, and the upper and lower bounds of $f_{dissim}^{org}$ were provided to the system of equations by predicting them using GEDYM (as described in section 2.2.2 and Appendix A).

### 2.4.3 Implementation: Matlab

I used the *fmincon* solver in Matlab to apply the system of equations to the datasets described in section 2.4. *fmincon* is a general constrained optimization algorithm available in the MATLAB Optimization Toolbox (MathWorks, 2016). Typically, this solver is used to minimize an objective function that is a function of the variables being solved for, given some constraints on the variables. In this case, it was used to solve for the non-linear system of equations, and thus no objective function was needed since the number of constraints is equal to the number of variables and the system of equations is completely defined. In this way, the root finding algorithms built into *fmincon* were used to solve the system of equations. *fmincon* uses the Newton-Raphson method as a first approach to solving the system of equations. If the Newton-Raphson method does not work, it uses a Conjugate Gradient step method instead (MathWorks, 2016). This local optimization method was implemented within a global search algorithm, which is also available in the MATLAB Optimization Toolbox (MathWorks, 2016). The global search algorithm uses a stochastic method to generate many starting points from which to run *fmincon* to identify which of the local solutions is the global solution (MathWorks, 2016).

### 2.4.4 Comparing actual versus predicted MEMs

Figures 2-5, 2-6, and 2-7 are parity plots comparing the observed versus the predicted MEM fractions (*i.e.*,$x_{ik}$). Agreement between the data is compared using the root mean squared error (RMSE) which is calculated using:

$$RMSE = \sqrt{\frac{1}{N} * \sum_{1}^{N} (x_{ik,pred} - x_{ik,obs})^2} \tag{2-36}$$

where $x_{ik,pred}$ is the value of $x_{ik}$ predicted by the modeling framework and $x_{ik,obs}$ is the value of $x_{ik}$ "observed" in the experimental dataset (calculated using Eq. 2-11), and N is the number of observations/ predictions.

The solutions predict the MEM fractions relatively well, with a maximum RMSE of 0.16 when predicting the 3 MEM fractions, and of 0.30 when predicting the fraction of the organic ED dissimilated ($f^{org}_{dissim}$) One reason for the deviation from the parity line between the observed and predicted fractions is the experimental error that is likely to occur during the measurement methods used to trace the carbon fixation activities. This error would be further propagated when these measurements were used to calculate the data-derived carbon and energy balance fractions, and subsequently, the MEM fractions.

The deviation from the parity line that is observed for the values of $x_{ik}$ is matched by deviation of the $f^{org}_{dissim}$ value from the parity line. This is because the accuracy of the prediction of the values of $x_{ik}$ depends on the accuracy of predicting $f^{org}_{dissim}$, which is evident in the governing equations. The value of $f^{org}_{dissim}$ controls to what extent heterotrophy or organotrophy occurs and therefore plays a role in predicting OH and LH, and LA indirectly since the value of LA is codependent on the value of LH predicted (Eq. 2-31). The predicted values of $x_{la}$ are systematically overpredicted for study 1 and underpredicted for study 3, which can be attributed to the inaccurate prediction of the value of $f^{org}_{dissim}$ (Figures 2-4 and 2-7). This is also matched by the deviation of another MEM fraction other than $x_{la}$, either $x_{lh}$ or $x_{oh}$, from the parity line, since the MEM fraction values predicted are not independent of each other. The predictions of the growth yields, which are used in Eq. 2-34 of the governing equations, and therefore of the MEM fractions, could be improved by more accurate geochemical data for the steady state conditions in the chemostats, since energetics calculations using the GEDYM are very sensitive to the

geochemical conditions used as inputs (Smeaton and Van Cappellen, 2018). The system of governing equations could be simplified from four to three equations by eliminating the explicit representation of $f^{org}_{dissim}$, and instead rearranging the existing equations such that $f^{org}_{dissim}$ is implicitly included in the system of equations.

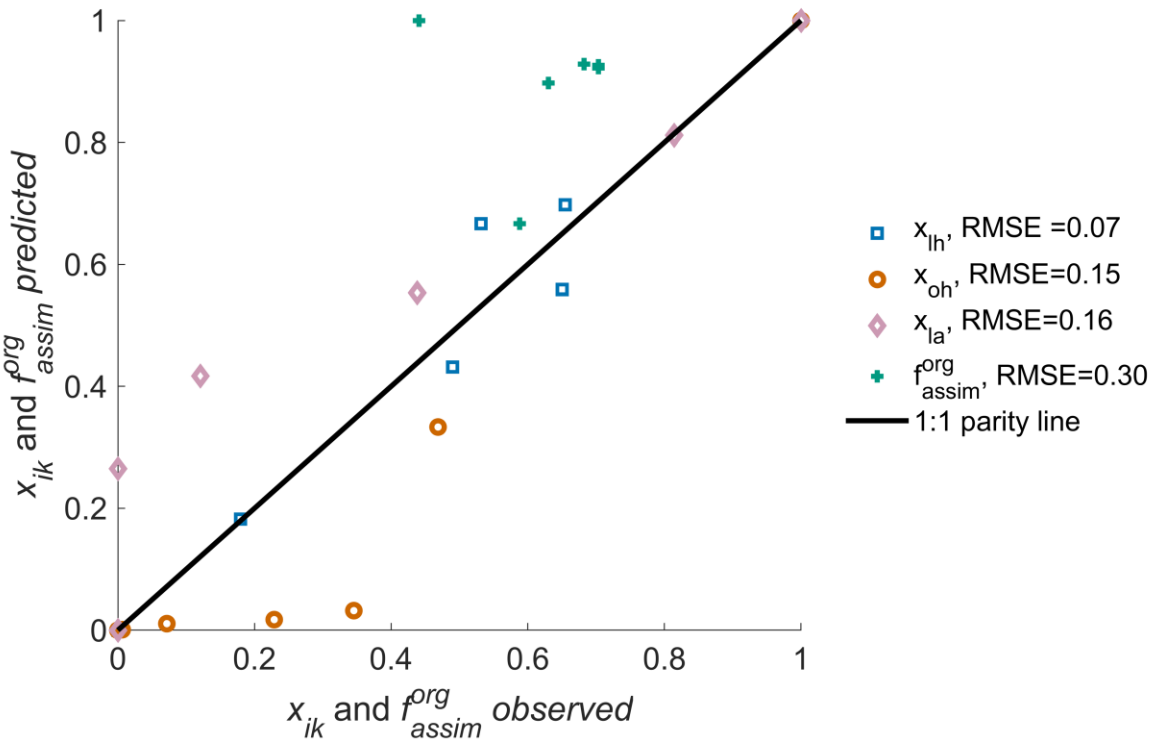


*Figure 2-5. Predicted versus observed fractions of three end member metabolisms ($x_{ik}$) and fraction of the organic ED substrate assimilated ($f_{assim}^{org}$) during growth of Paracoccus versutus on mixtures of acetate and thiosulfate. Representing data from Gottschal and Kuenen (1980) (study 1).*

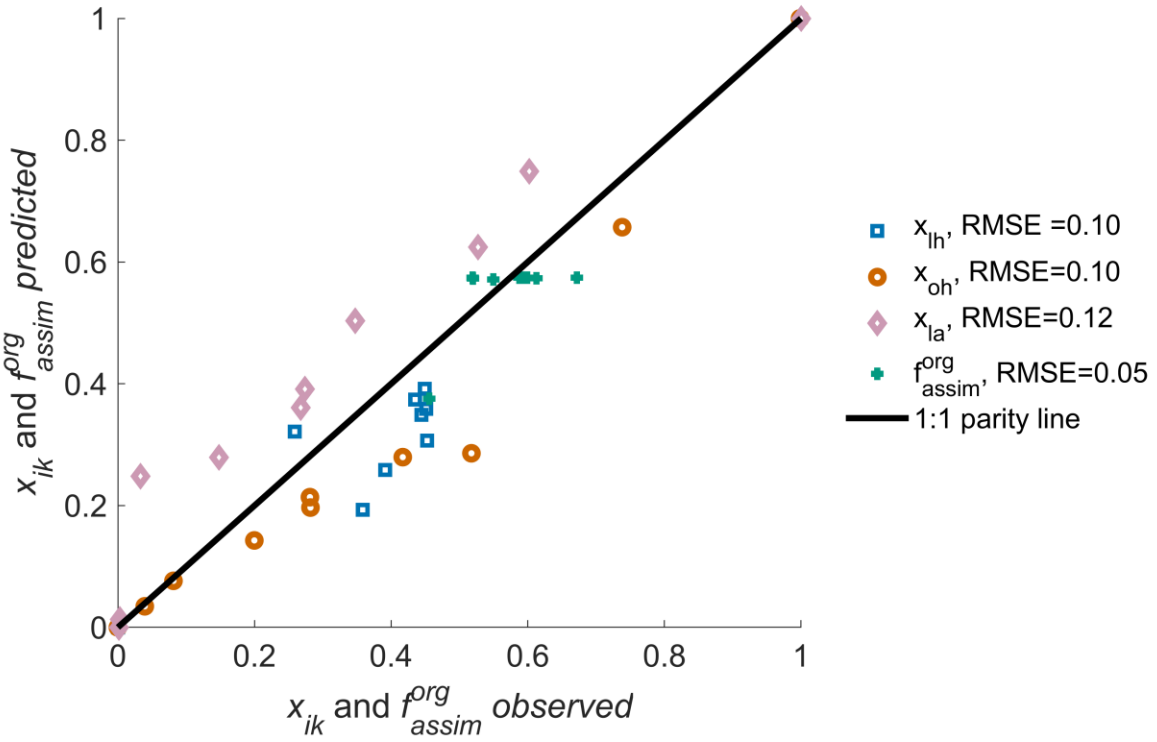


*Figure 2-6. Predicted versus observed fractions of three end member metabolisms ($x_{ik}$) and fraction of the organic ED substrate assimilated ($f_{assim}^{org}$) during growth of Pseudomonas oxalaticus on mixtures of acetate and formate,, calculated from data from Dijkhuizen et al. (1980) (study 2)*

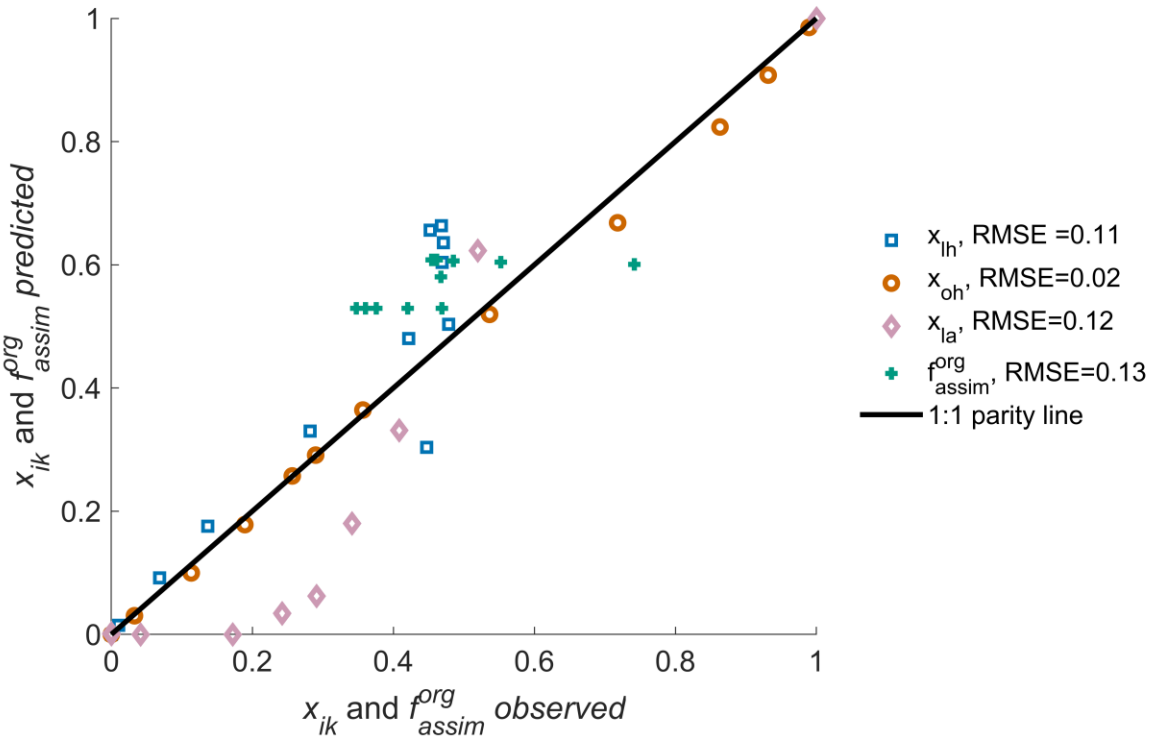


*Figure 2-7. Predicted versus observed fractions of three end member metabolisms ($x_{ik}$) and fraction of the organic ED substrate assimilated ($f_{assim}^{org}$) during growth of Pseudomonas oxalaticus on mixtures of oxalate and formate , calculated from data from Dijkhuizen and Harder (1979) (study 3)*

## 2.5 Discussion

### 2.5.1 Combined kinetic and energetic constraints regulate metabolic flexibility

The ability of the system of equations to predict the relative abundances of the 3 MEMs and $f_{dissim}^{org}$ demonstrates that it is the combination of thermodynamic (*e.g.*, bioenergetic) and kinetic constraints that regulates the combination of MEMs expressed under different ED supply scenarios. The role of the 2 ED utilization rates ($r_{ED}$) in regulating the relative proportions of the 3 MEMs is evident in the carbon and energy balance expressions that represent the constraints on the metabolism. The utilization rates of either one of or both of the 2 EDs are present in all 4 equations. These equations work to predict the MEM fractions because the "energy available" to an organism is primarily determined by the utilization rate of EDs, the kinetic constraints. The system of equations describes how each of the 2 ED substrates are required by 2 MEMs, and therefore how their utilization rates constrain whether these MEMs are possible. The second control on the "energy available" is the energetic constraints of the growth substrates, which are represented by the growth yields of the 3 MEMs, and the upper and lower bounds provided to the solver for predicting the value of $f_{dissim}^{org}$. The equations also represent the dual role of the organic compound as an ED and carbon source using the $f_{dissim}^{org}$ variable.

### 2.5.2 Implications for predicting carbon and energy cycling

The system of equations predicts the expression of autotrophy versus heterotrophy, two metabolic regimes with distinct energetic costs and growth efficiencies (*i.e.* growth yields). This has significant implications for the prediction of reaction rates for carbon and other elements associated with energy cycling in subsurface environments (Jin and Bethke, 2003).

The ability of this system of equations to predict the fractions of MEMs in ED-limited chemostats where mixed organic and inorganic EDs are present and consumed at low

concentrations explains the pervasiveness of autotrophy in aquifer and other terrestrial subsurface environments. The occurrence of autotrophy in these environments demonstrates that subsurface communities do not necessarily rely on carbon produced at the surface by photosynthesis for their energy or carbon (Griebler and Lueders, 2009; Probst *et al.*, 2014; Emerson *et al.*, 2016). For example, inorganic carbon trends and fluxes in the Colorado River aquifer were best reproduced when lithoautotrophy was included in the model (Arora *et al.*, 2017).

Therefore, predicting the occurrence of autotrophy and heterotrophy for whole communities in real environments using the system of equations proposed here has the potential to improve the representation of soil carbon cycling in models (Wieder *et al.*, 2015; Bradford *et al.*, 2016; Buchkowski *et al.*, 2017; Li *et al.*, 2017). Figures 2-3 and 1-5 highlight the significance of the LH MEM in controlling whether carbon dioxide fixation occurs, and to what extent, when an inorganic ED is being oxidized that can be used by lithotrophic MEMs (and when there is coincident utilization of an organic ED). LH is likely under underrepresented in current models and should be considered when representing lithotrophy in environmental models.

Autotrophic biomass-specific nitrate reduction rates can be ten times slower than those of heterotrophic denitrification (based on implicit maximum rate (*i.e.*, $r_{max}$ in Eq. 1-7) parameters collected by Handley *et al.* (2013)) due to the differences in growth yields between the heterotrophic and autotrophic MEMs (Figure 2-3). Consequently, omitting lithoautotrophic and lithoheterotrophic processes from a community's microbial reaction network would fail to account for potential denitrification pathways and could either over- or under- predict nitrate reduction rates. For example, including chemolithoautotrophic metabolic reactions in

geochemical models of the Colorado River aquifer is essential for predicting "hot spots" and hot moments" of nitrate removal (Dwivedi *et al.*, 2018). In section 3.3.4 of Chapter 3, I also demonstrate the sensitivity of nitrate cycling rates to the relative abundance of autotrophic activity.

Including these lithotrophic MEMs in reaction networks is not only important for predicting the turnover rates of electron acceptors, but also for predicting the oxidative cycling of reduced geochemical species (*i.e.*, EDs). ED oxidation reactions regenerate oxidized species which can be used as electron acceptors, closing the redox cycling of redox active elements such as C, N, Fe and S. For example, Yabusaki *et al.*(2017) showed that including chemolithoautotrophic pathways improved the predictions of S and Fe cycling in a Colorado River aquifer model.

While in this chapter I have only demonstrated the applicability of this framework at the population scale, I believe that the same kinetic and energetic constraints could potentially be applied at the community scale. At this scale, the goal of applying this framework would be to predict the relative functional abundances of metabolisms and their contributions to geochemical rates rather than specific biological species. This is also the typical goal in trait-based and dynamic energy allocation approaches, which this framework is similar to (Arora *et al.*, 2015). However, I acknowledge that representing community scale microbial processes is an ongoing challenge due to the need to account for facilitative, predative and competitive interactions (Hug and Co, 2018).

## 2.6 Conclusions

In this chapter, I present a modeling framework for predicting the competition between, and relative contributions of, autotrophic and heterotrophic metabolisms. Literature data collected from ED-limited chemostat studies were used to validate a system of governing equations that is

used to calculate the fractions of MEMs. With these equations, I show mathematically how the relative utilization rates of the organic and inorganic ED regulate the combination of MEMs expressed by the microorganisms grown in the chemostat experiments. Moreover, I show that the threshold at which inorganic carbon fixation (*i.e.*, autotrophy) is initiated is dependent on the energy contents of the two EDs. These findings highlight the key role of the ED supply rates in regulating autotrophy and heterotrophy in natural geomicrobial systems, as a direct consequence of the distinct energetic costs of the two end-member metabolisms. The occurrence of mixotrophy in the environment has important implications for the turnover of redox-active elements including N, S, Fe, Mn, H and especially C, since the relative utilization rates of organic versus inorganic EDs directly impacts carbon fixation versus mineralization.

# Chapter 3
# Application of a bioenergetic-kinetic model: Predicting mixotrophic nitrate-dependent iron oxidation in a lake sediment

## 3.1 Introduction

Lake sediments are a large reactive interface and reservoir, acting as either a source or sink of carbon, nutrients (*e.g.*, phosphorus and silicon), and metals (*e.g.*, arsenic and selenium) to the overlying water column (Hunter *et al.*, 1998; Pace and Prairie, 2005; Couture *et al.*, 2010; Omoregie *et al.*, 2013; Liu *et al.*, 2015; Orihel *et al.*, 2017). Sediment biogeochemistry is characterized by distinct vertical stratification of redox processes with depth from the sediment-water interface (SWI) (Van Cappellen *et al.*, 1993; Thullner *et al.*, 2007). Consequently, characterizing both the abiotic and biotic reactions occurring in sediments is essential for predicting the fate of carbon, nutrients and metals.

Iron (Fe) and nitrogen (N) are especially prominent in lake sediment energy cycling since manganese and sulfur concentrations are quite low, especially in Lake Constance, for which the sediment geochemistry is used in this chapter to predict the occurrence of a mixotrophic metabolism (Melton *et al.*, 2014). Nitrate and ferric iron (Fe(III)) are used as terminal electron acceptors for microbial respiration of organic carbon compounds in the absence of oxygen. While these reduction reactions link both the iron Fe and N cycles to the carbon cycle in sediments, the Fe and N cycles are directly linked by microbially mediated iron(II) ($Fe^{2+}$) oxidation coupled to nitrate ($NO_3^-$) reduction, also called nitrate dependent iron oxidation (NDFO). This lithotrophic catabolic reaction is given by reaction 3-1:

$$Fe^{2+} + 0.2NO_3^- + 1.4H_2O \rightarrow Fe(OH)_2^+ + 0.1N_2 + 0.8H^+ \qquad (3\text{-}1)$$

NDFO closes the Fe cycle in dark anoxic sediments where $Fe^{2+}$ oxidation using oxygen ($O_2$) or by phototrophic iron oxidizers is not possible (Roden 2012).

Found in sediments and groundwater at neutral pH, NDFO bacteria and archaea are well studied (Straub *et al.*, 1996). These organisms are suspected to be mixotrophs that are capable of coupling $NO_3^-$ reduction to the oxidation of either $Fe^{2+}$ or an organic ED substrate as their energy source, and of using both inorganic and organic carbon sources (Bryce *et al.*, 2018; Jamieson *et al.*, 2018). The proposed ED, EA, and C sources that would be used by the MEM reactions during NDFO-driven mixotrophy are summarized in Table 3-1. However, the exact mechanism(s) responsible for the net NDFO process observed in laboratory cultures, sediments and groundwater remains unknown. It is unclear if $Fe^{2+}$ oxidation is abiotic or biotic (Bryce *et al.*, 2018; Jamieson *et al.*, 2018). Furthermore, should NDFO be a lithotrophic metabolism where $Fe^{2+}$ oxidation is biotic, it is unknown if all strains can grow autotrophically (Bryce *et al.*, 2018).

*Table 3-1. Summary of electron donor, electron acceptor, and carbon source used by each metabolic end member reaction (MEM) during potential mixotrophic NDFO.*

| MEM reaction | Electron acceptor (EA) | Electron donor (ED) | Carbon source |
|---|---|---|---|
| OH | Nitrate ($NO_3^-$) | Acetate ($C_2H_3O_2^-$) | $C_2H_3O_2^-$ |
| LH | $NO_3^-$ | Iron(II) ($Fe^{2+}$) | $C_2H_3O_2^-$ |
| LA | $NO_3^-$ | $Fe^{2+}$ | Inorganic carbon ($HCO_3^-$) |

Evidence of the capacity for lithoheterotrophy during NDFO includes enhanced growth of pure cultures grown with $NO_3^-$ as their EA on mixtures of $Fe^{2+}$ and an organic ED substrate such as acetate (*e.g.*, Muehe *et al.*, 2009) over those grown on the organic ED alone (Muehe *et al.*, 2009; Chakraborty *et al.*, 2011; Bryce *et al.*, 2018). However, mechanisms that could explain this enhanced growth that do not involve enzyme-catalyzed $Fe^{2+}$ oxidation have been proposed. One proposed mechanism is that the enzymatic reduction of $NO_3^-$ reduction to nitrite ($NO_2^-$) using an organic ED/ C source (organoheterotrophy) induces chemodenitrification, the abiotic reduction of $NO_2^-$ by $Fe^{2+}$ oxidation. Chemodenitrification could confer an energetic advantage to NDFO organisms by acting as a detoxification mechanism for dealing with nitrite (Carlson *et al.*, 2013). Enhanced growth could also be explained by a high demand for nutrient iron in some organisms (Klueglein and Kappler, 2013).

Various studies have demonstrated that certain NDFO organisms may be unable to carry out NDFO-driven lithoautotrophy (Byrne-Bailey *et al.*, 2012; Ishii *et al.*, 2016), while studies of other organisms have demonstrated the opposite (Hallbeck and Pedersen, 1991; Straub *et al.*, 1996; Oshiki *et al.*, 2013). The capacity for NDFO-driven lithoautotrophy is likely present in whole communities of organisms, since it has been demonstrated in sediment incubations and enrichment cultures (Blöthe and Roden, 2009; Laufer *et al.*, 2016). These two unknown aspects of NDFO (*i.e.*, the relative contributions of biotic versus abiotic and heterotrophic versus autotrophic reactions) are related, since organoheterotrophy-driven $NO_3^-$ reduction to $NO_2^-$ and subsequent $Fe^{2+}$-driven chemodenitrification means that populations growing via that mechanism are not capable of either lithotrophic MEMs (neither lithoheterotrophy nor lithoautotrophy).

To investigate the bioenergetic constraints on the potential mixotrophic biotic contribution to NDFO, I apply the modeling framework developed for mixotrophy in Chapter 2,

representing the competition between $NO_3^-$ reducing, $Fe^{2+}$- or acetate- oxidizing autotrophic and heterotrophic metabolisms in lake sediments. I apply it to literature geochemical and microbial datasets collected in the profundal sediments of Lake Constance (Schulz and Conrad, 1995; Melton *et al.*, 2014). NDFO is identified as a likely mixotrophic metabolism occurring in these sediments (Hauck *et al.*, 2001; Muehe *et al.*, 2009; Melton *et al.*, 2012; Melton *et al.*, 2014).

### 3.1.2 Lake Constance background

Lake Constance is a large (over 500 $km^2$) freshwater lake located at the border of Switzerland, Germany, and Austria at an elevation of 385 m above sea level (Altermatt *et al.*, 2014). L. Constance is a monomictic lake, experiencing stratified conditions between the months of May and September, and fully mixed conditions otherwise (Wahl and Peeters, 2014). The depth of water in the profundal zone of L. Constance ranges from 60-254 m, with a mean depth of 100 m (Hauck *et al.*, 2001; Wahl and Peeters, 2014). The sediment geochemistry in L. Constance is quite well characterized. In terms of electron accepting half reactions, there are prominent $O_2$-, $NO_3^-$-, iron(III)-, and $CO_2$- reducing zones at different depths in L. Constance sediments (Schulz and Conrad, 1995; Schulz and Conrad, 1996; Melton *et al.*, 2014). In terms of electron donors, $Fe^{2+}$, $NH_4^+$, and organic acids are commonly used (with the organic acids also being used as carbon sources) (Melton *et al.*, 2014).

## 3.2 Methods

### 3.2.1 Geochemical dataset compilation and synthesis

Reported high resolution *in situ* porewater profiles of $O_2$, $NO_3^-$, ammonium ($NH_4^+$), and pH in Lake Constance from Fig. 2 in Melton *et al.* (2014) were digitized using WebPlotDigitizer (Rohatgi, 2019)**.** Concentrations of poorly crystalline (0.5 M HCl extractions) and crystalline solid phase $Fe^{2+}$ and $Fe^{3+}$ (6 M HCl extractions) with depth were digitized from Fig. 3, MPN counts were taken from Table 1, and functional gene copy numbers were digitized from Fig. 8 in

Melton et. al (2014a). The digitized geochemical data was interpolated to a resolution of 0.1 mm using an interpolation tool in Matlab (MathWorks, 2016). Porewater acetate concentrations were estimated to be constant at 7 μM at all depths, based on Fig. 2 in Schulz and Conrad (1995). The MPN enumeration data collected from Melton *et al.* is given in Table 3-2. They used two types of media, one that selected for heterotrophic NDFO organisms, and another that selected for autotrophic NDFO organisms. I therefore used these enumerations to approximate the potential relative abundance of heterotrophic and autotrophic activity with depth in the sediment.

Porewater aqueous $Fe^{2+}$ concentrations were approximated by modeling the sediment geochemistry in PHREEQC (Parkhurst and Appelo, 2013)**,** where aqueous $Fe^{2+}$ was in equilibrium with solid phase siderite, the predominant iron(II) mineral in Lake Constance sediments (Schink and Benz, 1999) (Figure 3-1, panel A). The solid phase siderite concentrations used in PHREEQC (Parkhurst and Appelo, 2013) were the poorly crystalline solid phase iron(II) concentrations taken from Melton *et al.* (2014). The activities of the other reactants and products of the catabolic and anabolic reactions (given in Table B-1 in Appendix B) were also estimated using PHREEQC (Figure B-1, appendix B).

Figure 3-1, panel A shows the dissolved $Fe^{2+}$ and acetate concentration profiles, while Figure 3-1, panel B shows the dissolved $NO_3^-$ and $O_2$ concentration profiles and the predicted zone of $NO_3^-$ reduction. The additional geochemical data ($HCO_3^-$, $NH_4^+$, $NO_3^-$, extractable-poorly crystalline iron(III) and iron(II) concentrations, and pH) used for modeling the sediment are shown in Figure B-1 in appendix B. The microbiological qPCR data digitized from Melton *et al.* (2014) are plotted in Figure B-2.

### 3.2.2 Applying the bioenergetic-kinetic modeling framework

As outlined in Section 3.2, while the exact mechanisms of NDFO are not fully known or agreed upon, for the purposes of this chapter, I assume that NDFO is a mixotrophic metabolism that can be represented using the three metabolic end member (MEM) modeling framework introduced in Chapter 2. The presence of *Gallionella* spp., an $Fe^{2+}$ oxidizing bacteria that is capable of mixotrophic NDFO, in the lake sediments of Lake Constance demonstrates the potential metabolic capacity of the microbial community for facultative chemolithoautotrophy (Hallbeck and Pedersen, 1991; Melton *et al.*, 2014). Chemodenitrification (*i.e.*, abiotic $NO_2^-$ reduction by $Fe^{2+}$) is not included in this modeling exercise because the goal of this Chapter is to demonstrate the application of the modeling framework developed in Chapter 2 to an environmental system.

The 3 anabolic and 2 catabolic reaction stoichiometries assumed to be carried out during mixotrophic NDFO are given in Table B-1 (Appendix B). The $NO_3^-$ reduction half reaction was assumed to be denitrification (*i.e.*, $NO_3^-$ is reduced to $N_2$) rather than dissimilatory nitrate reduction to ammonium (DNRA). While DNRA via organic C or iron (II) oxidation is possible (Robertson *et al.*, 2016; Robertson and Thamdrup, 2017), and even autotrophically (Robertson and Thamdrup, 2017), most studies of NDFO metabolisms focus on $NO_3^-$ reduction via denitrification to $N_2$ (*e.g.*, Jamieson *et al.*, 2018). I chose to focus on denitrification since it is one end member electron accepting reaction and the motivation of this research is to account for account for the competition between autotrophy and heterotrophy coupled to some fixed electron acceptor reduction reaction. Goethite (FeOOH) is the assumed iron(III) mineral produced by $Fe^{2+}$ oxidation because it is considered to be one of the more common minerals produced (Chakraborty and Picardal, 2013). Many other mineral and amorphous Fe(III) oxide products may be produced by microbial oxidation, including goethite, magnetite, lepidocrocite, and green

rust or other amorphous ferric oxides (Vollrath, 2012; Seto, 2014; Jamieson *et al.*, 2018). The growth yields and the Gibbs energies of catabolism, anabolism and metabolism were calculated as outlined in Chapter 2 (section 2.3.2 and Appendix A) for the 3 end member metabolisms using the chemical activities of the reactants and products computed in PHREEQC (Figure B-5).

I used the digitized concentration profiles from Figure 3-1 A and implicit Monod-type kinetic equations to determine $Fe^{2+}$ and acetate oxidation rates. Since both oxidation reactions were coupled to $NO_3^-$ reduction, limitation by $NO_3^-$ and inhibition by $O_2$ was accounted for with multiplicative Monod limitation and inhibition factors for these processes. Acetate oxidation rates **(**$R_{ac}$ [mol acetate (L d)$^{-1}$]**)** were determined using Eq. 3-2:

$$R_{ac} = r_{ac}^{max} \frac{C_{ac}}{C_{ac} + K_{ac}} \cdot \frac{C_{NO_3^-}}{C_{NO_3^-} + K_{NO_3^-}} \cdot \frac{K_{O_2}^{in}}{C_{O_2} + K_{O_2}^{in}} \qquad (3\text{-}2)$$

where $C_{ac}$ is the concentration of acetate [mol acetate (L)$^{-1}$], $r_{ac}^{max}$ is the implicit maximum rate of acetate oxidation [mol acetate (L d)$^{-1}$], $K_{ac}$ is the half-saturation constant of acetate [mol acetate (L)$^{-1}$], $C_{NO_3^-}$ is the concentration of $NO_3^-$ [mol $NO_3^-$ (L)$^{-1}$], $K_{NO_3^-}$ is the half-saturation constant of $NO_3^-$ [mol $NO_3^-$ (L)$^{-1}$], $C_{O_2}$ is the concentration of $O_2$ [mol $O_2$ (L)$^{-1}$], and $K_{O_2}^{in}$ is the inhibition constant for oxygen [mol $O_2$ (L)$^{-1}$].

Iron(II) oxidation rates were estimated using Eq. 3-3:

$$R_{Fe^{2+}} = r_{Fe^{2+}}^{max} \frac{C_{Fe^{2+}}}{C_{Fe^{2+}} + K_{Fe^{2+}}} \cdot \frac{C_{NO_3^-}}{C_{NO_3^-} + K_{NO_3^-}} \cdot \frac{K_{O_2}^{in}}{C_{O_2} + K_{O_2}^{in}} \qquad (3\text{-}3)$$

where $C_{Fe^{2+}}$ is the concentration of $Fe^{2+}$ [mol $Fe^{2+}$ (L)$^{-1}$], $r_{Fe^{2+}}^{max}$ is the implicit maximum rate of acetate oxidation [mol $Fe^{2+}$ (L d)$^{-1}$], and $K_{Fe^{2+}}$ is the half-saturation constant of acetate [mol $Fe^{2+}$ (L)$^{-1}$].

The parameters used in Eq. 3-2 and 3-3 were taken from the literature and are summarized in Table 3-3. Figure 2-1 (panel C) shows the predicted $Fe^{2+}$ and acetate oxidation

rates with depth. Fig. B-3 compares calculated $Fe^{2+}$ oxidation rates to the observed numbers of sediment *Gallionella* spp. gene copy numbers, and to the concentration of poorly crystalline Fe (III) (0.5 M HCl-extractable) in the sediment.

Using the MEM reaction stoichiometries described in Table B-1 (Appendix B) and ED utilization rates estimated using Eq. 3-2 and 3-3, the modeling framework described in Chapter 2 was applied to the assembled dataset to predict the relative rate of the mixotrophic MEMs associated with NDFO occurring in the $NO_3^-$ reducing zone of the sediment. Steady state conditions were assumed, such that a kinetic model representing the evolution of sediment chemistry over time was not needed. In other words, I assume that there is no net change in the concentrations of the energetic and nutrient substrates (*e.g.*, $Fe^{2+}$, $NO_3^-$, acetate, $NH_4^+$) in the sediments because the sum of the fluxes supplying them (via a combination of geochemical and transport processes) are equal to the sum of the fluxes that are removing them.

To calculate the MEM-specific rates of $NO_3^-$ reduction and dissolved inorganic C (DIC) consumption/ production, the stoichiometries of the metabolic reactions of each MEM were calculated from the GEDYM-predicted growth yields. The ratio of these metabolic stoichiometric coefficients was then used to convert the ED (*i.e.*, $Fe^{2+}$ or acetate) oxidation rates to units of $NO_3^-$ reduction or DIC consumption/ production using the equations described in section 2.2.2. The sum of these MEM-specific rates thus represents the net mixotrophic rate of $NO_3^-$ reduction or DIC consumption/ production.

*Table 3-2. Most Probable Number data from Melton et al. (2014)*

| Sediment depth (mm) | Autotrophic $Fe^{2+}$ oxidizing, $NO_3^-$ reducing | Heterotrophic, $Fe^{2+}$ oxidizing, $NO_3^-$ reducing | % Heterotrophy estimated |
|---|---|---|---|
| | Cells ($10^3$) / g dry weight sediment | | |
| 0-1 | 23.8 | 263 | 91 |
| 8-9 | 15.1 | 716 | 98 |
| 19-20 | 146 | 199 | 58 |

*Table 3-3. Monod kinetic parameters used to calculate the rates of iron oxidation and acetate oxidation in the sediments.*

| Parameter | Description | Literature value | Units | Source |
|---|---|---|---|---|
| $r_{Fe^{2+}}^{max}$ | Maximum iron (II) oxidation rate ($\Delta Fe(II)$ measured during incubation of lake sediment slurry, pH 7) | $1.4 * 10^{-4}$ | M $d^{-1}$ | [1] |
| $K_{Fe^{2+}}$ | Half-saturation of iron (II) during iron(II) oxidation | $1 * 10^{-5}$ | M | [2] |
| $r_{ac}^{max}$ | Maximum acetate oxidation rate (aerobic) | $1.2 * 10^{-5}$ | M $d^{-1}$ | [3] |
| $K_{ac}$ | Half-saturation constant of acetate during acetate oxidation | $2 * 10^{-5}$ | M | [3] |
| $K_{NO_3^-}$ | Half-saturation of nitrate in denitrification | $1.1 * 10^{-4}$ | M | [4] |
| $K_{O_2}^{in}$ | Inhibition constant for oxygen | $1.6 * 10^{-8}$ | M | [4] |

1: (Kopf *et al.*, 2013); 2: (Arora *et al.*, 2017); 3: (Yabusaki *et al.*, 2017); 4: (Arora *et al.*, 2016)

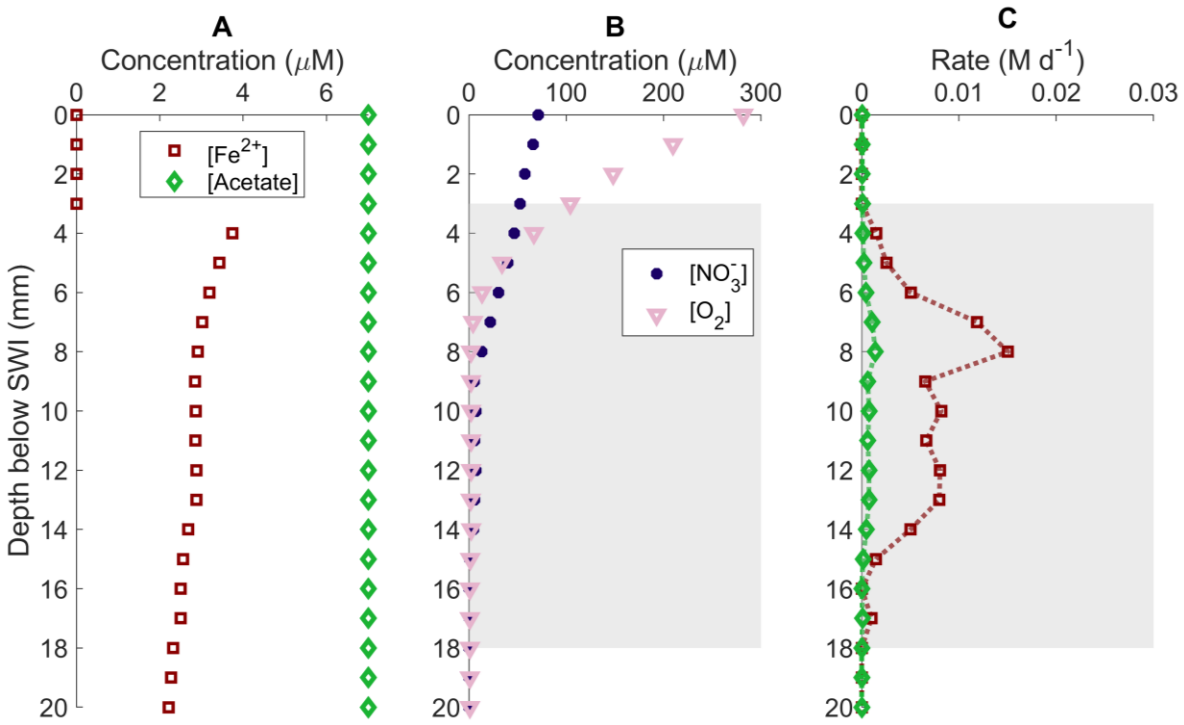


*Figure 3-1. Depth profiles of concentration data taken from Melton et al. (2014) and predicted rates. Depth profile A: Concentrations of porewater $Fe^{2+}$ and acetate with depth. Depth profile B: Concentrations of porewater $NO_3^-$ and $O_2$ with depth. Depth profile C: Acetate and $Fe^{2+}$ utilization rates calculated using Monod kinetics with depth. In panels B and C, the zone where nitrate reduction is occurring is noted by the gray shading. Data taken from Melton et al. (2014) and Schulz and Conrad (1995).*

### 3.2.3 Sensitivity analysis

To test the sensitivity of the MEM fractions and C, N and Fe rates predicted to the values of $r_{ED}^{max}$ provided to the kinetic constraints (*i.e.*, Eq. 3-2 and 3-3) in the modeling framework, I varied the values of $r_{Fe^{2+}}^{max}$ and $r_{Ac}^{max}$ within defined ranges. For $r_{Fe^{2+}}^{max}$, this range was $1.4*10^{-5}$ to $1.4*10^{-3}$ mol $Fe^{2+}$ $(L\ d)^{-1}$, while for $r_{Ac}^{max}$, this range was $1.2*10^{-7}$ to $1.2*10^{-3}$ mol acetate $(L\ d)^{-1}$. To demonstrate the sensitivity of the simulated nitrate reduction, $Fe^{2+}$ oxidation, and net inorganic C consumption/ production rates to the fraction of autotrophy ($f_a$) simulated, I grouped the data according to the range of $f_a$ values that the predicted $f_a$ occupies. I limited the sensitivity analysis to depths where nitrate reduction was not inhibited by oxygen, since this would confound the interpretation of the influence of $f_a$ on the predicted rates. I used the grouped data to fit linear regressions and Monod-type kinetic parameters to the data, which is not possible using continuous data. I use this analysis to consider the impact on the fraction of autotrophic activity on the nitrate reduction rates predicted for the same geochemical conditions (Figure 3-4). I used the grouped data to calculate the value of $r_{NO_3^-}^{max}$, the maximum implicit nitrate reduction rate, for each range of $f_a$, by fixing the value of $K_{NO_3^-}$ at $1.1*10^{-4}$ (which is the value derived from the literature, see Table 3-3). I also used the $f_a$-grouped data to analyze the impact of variable proportions of autotrophic activity on the ratios of coupling between the rates of DIC consumption/ production, $NO_3^-$ reduction, and $Fe^{2+}$ oxidation (Figure 3-5).

## 3.3 Results and Discussion

### 3.3.1 Nitrate, inorganic carbon, and iron(II) turnover rates predicted

The $NO_3^-$ reducing zone of the sediment occurs between 3 and 18 mm below the sediment-water interface (SWI), based on the Monod-type kinetics-predicted rates that incorporated a $NO_3^-$ limitation and $O_2$ inhibition factor (Figure 3-1 B and C). Above this zone, $O_2$ would be the

electron acceptor used for oxidizing EDs, although that is not explicitly represented in the model considered here, while below this zone, iron(III) reduction would be the electron accepting half reaction (Melton *et al.*, 2014). The peak $Fe^{2+}$ oxidation, $NO_3^-$ reduction, and acetate oxidation rates occur at around 8-10 mm below the SWI (Figure 3-1 A, Figure 3-3). Calculated $NO_3^-$ reduction rates compare relatively well to the relative abundances of the copy numbers of $NO_3^-$ reduction related genes (nirK, nirS and narG) (Appendix B, Figure B-4). The $Fe^{2+}$ oxidation rates predicted with depth in the sediment correlate well with the concentration of amorphous iron(III) oxides, but not very well with the relative abundance of *Gallionella* spp. gene copy numbers (Appendix B, Figure B-3). The net DIC consumption/ production rate calculated indicates that mixotrophic NDFO is a net producer of DIC given the chemical conditions in the $NO_3^-$ reducing zone of the sediments. Although the fraction of LA (which consumes DIC) predicted is relatively high compared to the fraction of OH predicted, the growth yield, and therefore also the DIC fixation activity, of the LA MEM predicted is very low.

### 3.3.2 MEM fractions predicted

The predicted MEM fractions fall into two distinct groups based on the depth in the sediment and therefore the geochemical controls. At depths between 0 and 4 mm below the sediment water interface (SWI), organoheterotrophy (*i.e.*, ED= acetate, EA= $NO_3^-$) is the only predicted $NO_3^-$-reducing MEM (Figure 3-2 A). At these depths, oxygen is still present (Fig. 2-3 B), which consumes any $Fe^{2+}$ by abiotic oxidation and outcompetes microbial iron oxidation. Thus, the only remaining ED (acetate)/ EA ($NO_3^-$) couple is predicted to be occurring, albeit at very low rates due to inhibition of $NO_3^-$ reduction by oxygen (in terms of the $NO_3^-$ reduction rate, Figure 3-3). Thus, the fraction of heterotrophy predicted at these depths is 1, which is in good agreement with the fraction of heterotrophy calculated using the MPN counts (Figure 3-1-B). At

depths greater than 4 mm, conditions are suboxic, $NO_3^-$ reduction is not inhibited, and iron oxidation is not outcompeted. Therefore, NDFO-driven $Fe^{2+}$ oxidation and acetate consumption (oxidation and incorporation into biomass) are both predicted to be occurring at these depths based on their concentrations in the sediment and the kinetic parameters used to predict utilization rates. The predicted percentages of organoheterotrophy (OH), lithoheterotrophy (LH), and lithoautotrophy (LA) in this $NO_3^-$-reducing zone are relatively constant, and are predicted to be 3-4%, 37-40%, and 53-58%, respectively, and the predicted percentage of heterotrophy is thus 40-44%.

The predicted fraction of heterotrophy ($f_h$) at a depth of 20 mm below the SWI is in relatively close agreement with the observed values (Figure 3-2B). However, there is a large discrepancy between predicted and observed values at 9 mm, at which the predicted fraction of heterotrophy (40%) is much lower than the observed value (100%). Possible reasons for the discrepancy between predicted and observed fractions of heterotrophy at 9 mm may be due to either the over-interpretation of the meaning of MPN counts, or an unaccounted-for reaction (biotic or abiotic) in both the conceptual and mathematical model. MPN counts are not necessarily representative of the *in situ* rates of processes occurring in the sediment (Regnier *et al.*, 2005). In other words, MPN counts quantify the capacity of the total population for function (*e.g.*, denitrification), but that total population may not be actively carrying out that process *in situ*. Moreover, unculturable microorganisms missed by the MPN method remain unaccounted for, which potentially biases the assessment towards only culturable microorganisms (Lloyd *et al.*, 2018). To overcome these limitations, *in situ* autotrophic activity could be detected by measuring in-situ enzyme activities of rubisco (one of the enzymes responsible for carbon

fixation, *e.g.*, Kellermann *et al.* (2012)), by omics methods (*e.g.*, Probst *et al.* (2017)), or by stable isotope fractionation (*e.g.*, Preuß *et al.* (1989)).

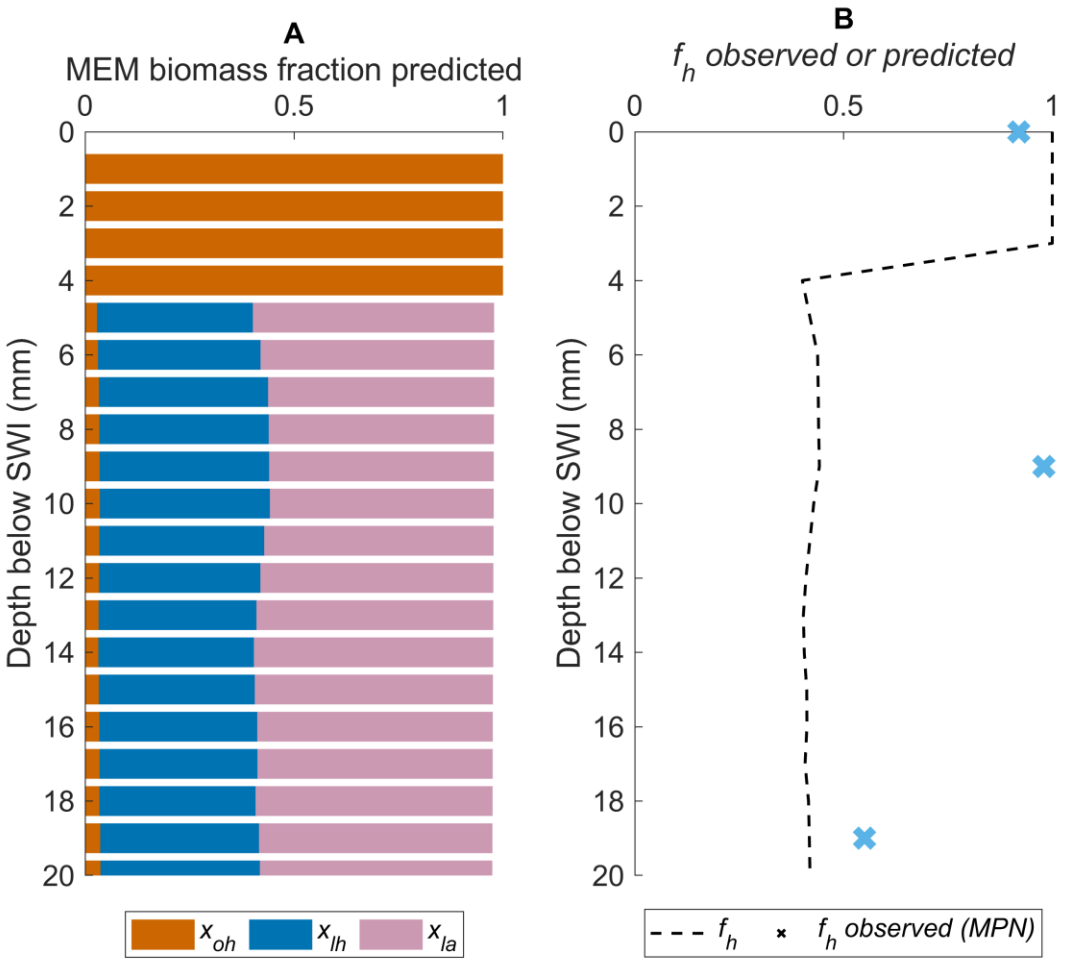


*Figure 3-2. Fractions of all 3 MEMs predicted with depth (left panel), and fraction of heterotrophy ($f_h$) predicted (dotted line) and observed (($f_{h\ obs}$ via MPN counts, pink symbols) with depth (right panel).*

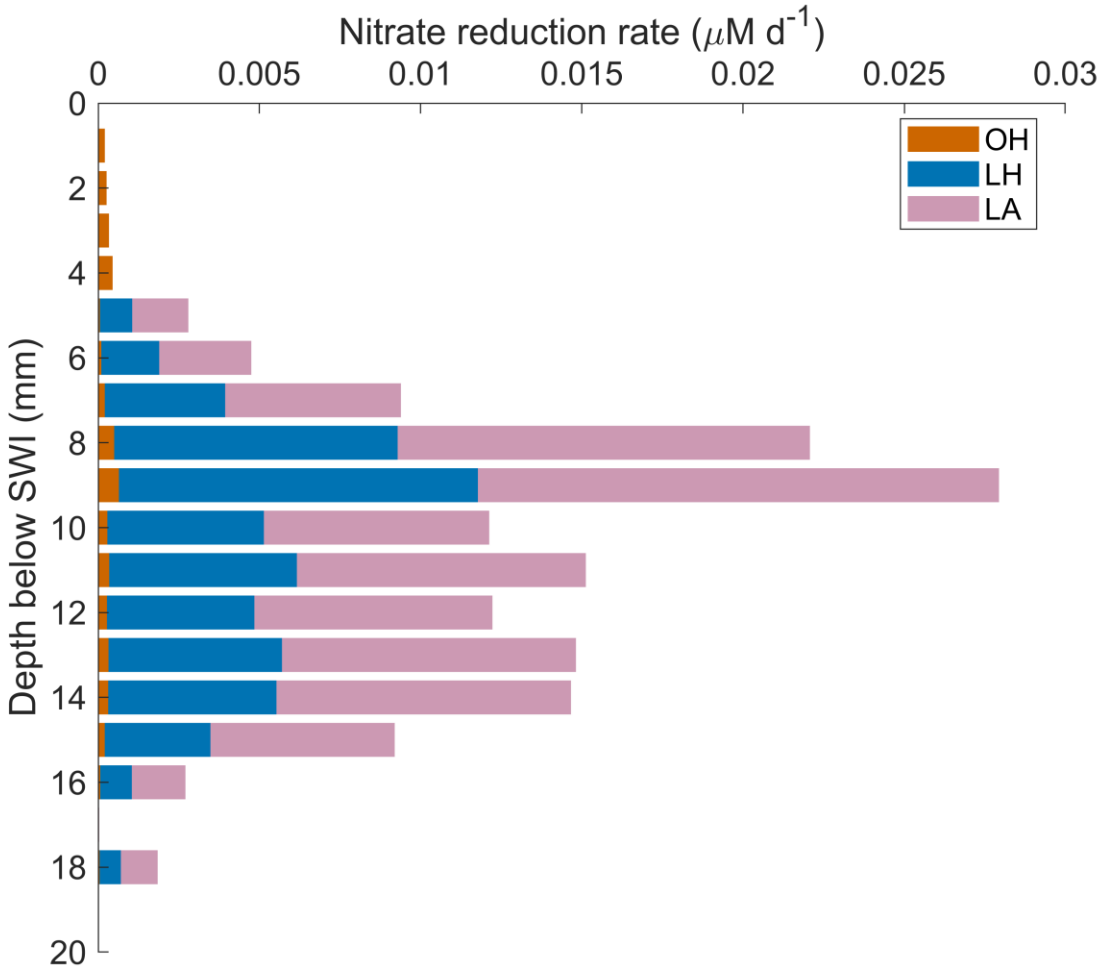


*Figure 3-3. Total $NO_3^-$ reduction rate (indicated by bar length), and MEM-specific $NO_3^-$ reduction rate (colour of bar segments) predicted with depth in the sediment. MEM-specific $NO_3^-$ rates were calculated as described in section 3.3.3.*

### 3.3.3 Implications of mixotrophy for predicting $NO_3^-$ reduction rates

In this section, I use the sensitivity analysis described in section 3.2.3 to demonstrate the implications of the relative abundance of autotrophic metabolisms for the overall rate of turnover of electron acceptor substrates (*i.e.*, $NO_3^-$ in this case), which was also discussed in section 2.5.2 in Chapter 2. In the absence of the sensitivity analysis, the predicted relative proportion of autotrophy and heterotrophy does not change significantly with depth in the sediment (Figure 3-2 A).

The contribution of OH and LH to total $NO_3^-$ reduction rates (Figure 3-3) is greater than their contribution to predicted MEM biomass fractions (Figure 3-2 A). This reflects the higher overall turnover rates of $NO_3^-$ by these two heterotrophic metabolisms. These higher turnover rates are due to the higher growth yields compared to autotrophic metabolisms (Figure B-4 A). While autotrophic metabolisms have higher biomass-specific turnover rates (*i.e.*, the inverse of their growth yields are greater than those of heterotrophic metabolisms), they accumulate less biomass because of their lower growth yields. Collectively, this results in lower overall turnover rates of metabolites (Koenig and Liu, 2001; Cardoso *et al.*, 2006; Handley *et al.*, 2013). As section 2.5.2 in Chapter 2 highlighted, the consequence of the different MEM-specific turnover rates is that mixotrophic activity has the potential to impact the predicted turnover rates of not only C, but all redox-active elements that are used by microbial metabolisms.

The impact of the simulated variable mixtures of autotrophic and heterotrophic activity on $NO_3^-$ reduction rates is shown in Figure 3-4 A. For the same $NO_3^-$ concentration, simulated $NO_3^-$ reduction rates decrease with increasing autotrophy. The curves shown in Figure 3-4 were fit using Monod-type kinetics. As section 3.2.3 describes, the $K_{NO_3^-}$ values were held constant, while the implicit maximum rate parameter, $r_{NO_3^-}^{max}$, was used to fit the curves to the groups of

data. The $r_{NO_3^-}^{max}$ parameters fit to the $f_a$-grouped rates decreased with increasing $f_a$. The overall trend is clear in Figure 3-4 B, with $r_{NO_3^-}^{max}$ decreasing from 171 to 85 μM $d^{-1}$ as $f_a$ increased from 0.1-0.2 to 0.9-1. This trend in the value of the implicit kinetic parameter was generated indirectly by combining the predicted rates of iron oxidation and acetate oxidation using the GEDYM-predicted metabolic reaction stoichiometries to convert the rates to units of [mol $NO_3^-$ $(L\ d)^{-1}$].

### 3.3.4 Implications of mixotrophy for the coupling of C, N and Fe cycles

Figure 3-5 shows the changing ratios between N, Fe and DIC turnover rates as a function of the fraction of autotrophy using the results of the sensitivity analysis described in section 3.2.3. The data from the simulations were again grouped by ranges of the fraction of autotrophy predicted, and linear curves were fit to the grouped data. There are three trends as $f_a$ increases and the overall metabolic reaction stoichiometry for mixotrophic growth changes: the ratio of $NO_3^-$ reduced to $Fe^{2+}$ oxidized decreases, the ratio of net DIC consumed to $Fe^{2+}$ oxidized increases, and the ratio of net DIC fixed to $NO_3^-$ reduced increases (Figure 3-5). Both the DIC:Fe(II) and DIC:N ratios increase from negative values, which indicate net DIC production, and approach positive values with increasing $f_a$. Thus, the predicted $NO_3^-$ consumption rates do not always correlate with net DIC production, as would be the assumption if organoheterotrophy was the only $NO_3^-$ reducing metabolism. Furthermore, the ratio of DIC fixed/ produced to $NO_3^-$ reduced varies as a function of autotrophic activity. The rate of DIC turnover to $Fe^{2+}$ oxidation is also not constant with variable autotrophic activity. These figures emphasize the need to account for competing autotrophic and heterotrophic, and organotrophic and lithotrophic reactions to be able to predict the coupling between the elements used for energy cycling by those metabolisms.

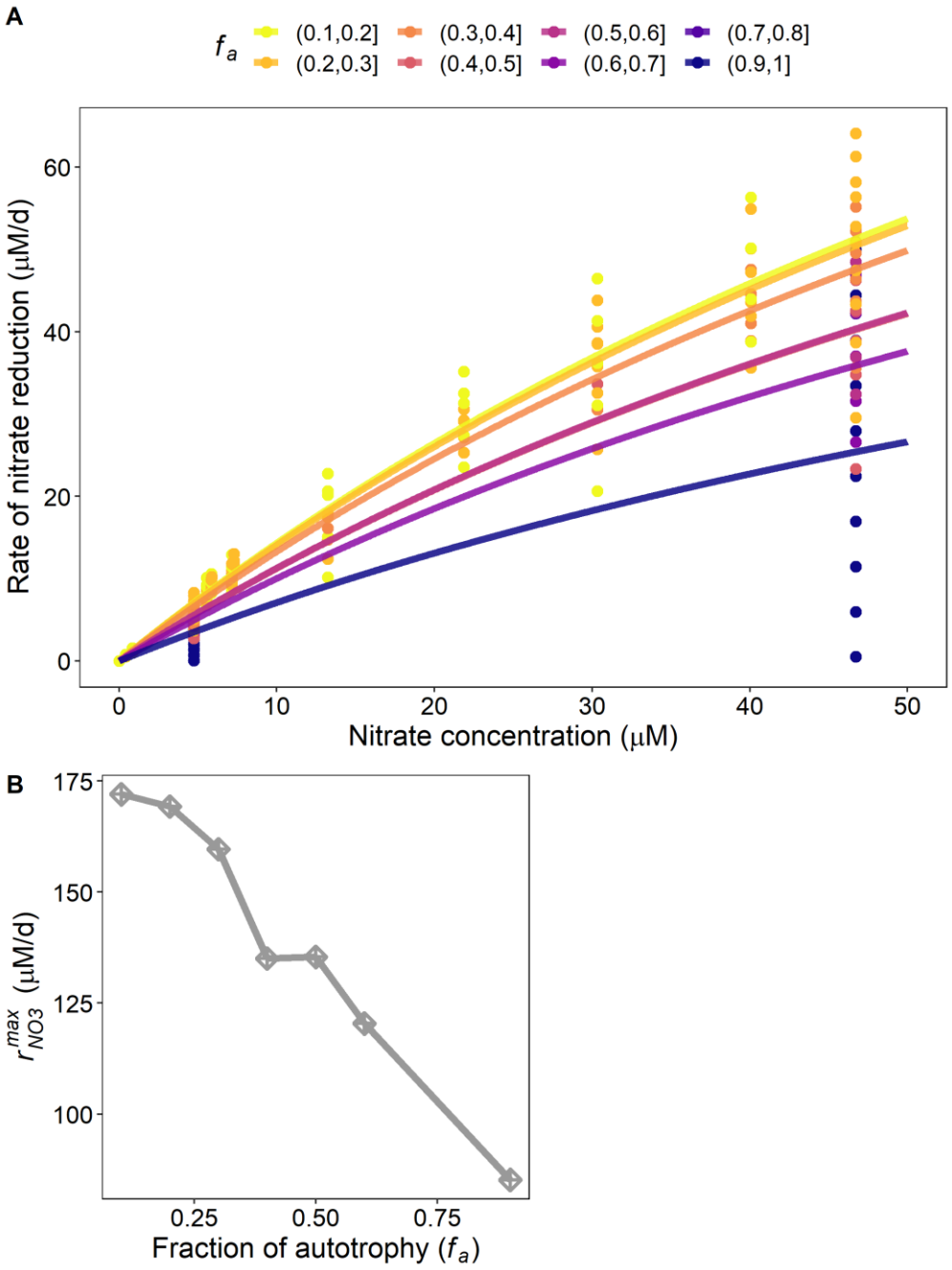


*Figure 3-4. Simulated $NO_3^-$ reduction rates and predicted implicit maximum rates.*
*A: Simulated $NO_3^-$ reduction rates shown as a function of sediment $NO_3^-$ concentration (x-axis) and fraction of autotrophy (colour of points and curves). Curves represent Monod-type curves fit to data points by the fraction of autotrophy, where $K_{NO_3^-}$ is fixed at $1.1*10^{-4}$ M. The method used to generate the simulated data is described in section 3.2.3. B: Values of implicit rate constant, $r^{max}_{NO_3^-}$, fit to data in panel A, shown as a function of the fraction of autotrophy.*

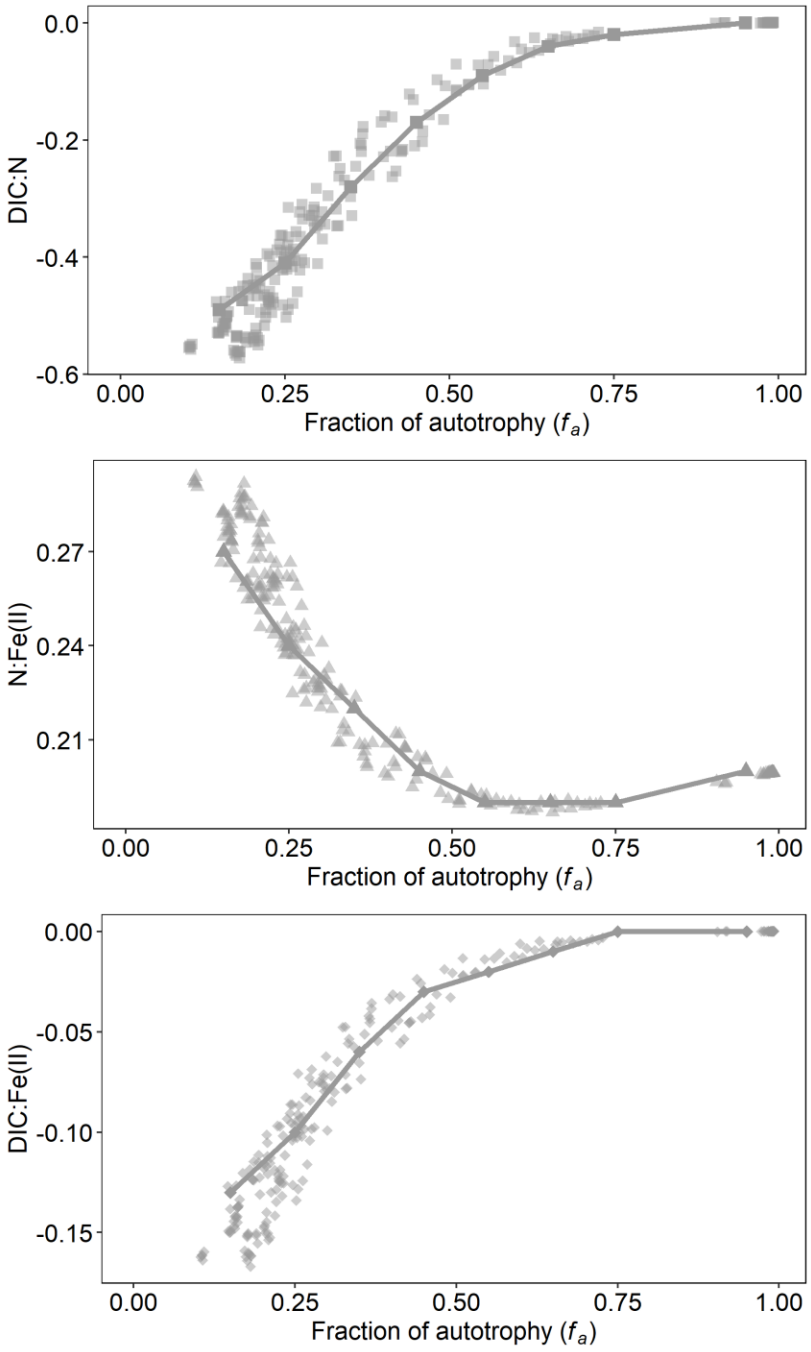


*Figure 3-5.Predicted ratios of coupling of $NO_3^-$:$Fe^{2+}$, DIC: $Fe^{2+}$, and DIC:$NO_3^-$ as a function of the fraction of autotrophic activity. The method for generating the "simulated rates" that were used to calculate these simulated ratios is described in section 3.2.3. The calculated ratios of coupling for each simulated fraction of autotrophy are the semi-transparent points, while the solid lines and points represent the ratios calculated when the simulated rate data is grouped by the fraction of autotrophy.*

### 3.3.5 Limitations of the modeling approach

For the purposes of demonstrating the application of the modeling framework developed in Chapter 2, the scope of sediment biogeochemical processes that are represented is limited compared to what occurs in natural sediments. Many other microbially controlled reactions that impact C, Fe, and N cycling directly and indirectly occur in sediments including $NH_4^+$ oxidation, sulfide oxidation, and/ or acetate (or other organic acid) oxidation, coupled to iron(III) reduction, sulfate reduction, and/ or $O_2$ reduction. The C, N and Fe balances calculated represent only the processes that are predicted to be occurring in the $NO_3^-$ reducing zone of the sediment. In Lake Constance, mixotrophic $NH_4^+$ oxidation coupled to iron(III) reduction is likely present below the zone of $NO_3^-$ reduction (Melton *et al.*, 2014). In the oxic zone of the sediment, microaerophilic mixotrophic or autotrophic metabolisms such as sulfide oxidation are possible, as are photoautotrophic metabolisms such as phototrophic iron oxidation (Geelhoed *et al.*, 2009; Melton *et al.*, 2012). Mineral precipitation and dissolution reactions (*e.g.*, pyrite dissolution and precipitation) or abiotic reactions (*e.g.* chemodenitrification, sulfide oxidation by $O_2$) are also not represented.

Other limitations to the modeling approach are related to the lack of fundamental knowledge regarding the energetics and stoichiometries of microbial $Fe^{2+}$ oxidation and $NO_3^-$ reduction reactions. A largely unknown aspect of the bioenergetics of $Fe^{2+}$ oxidation is what chemical species of $Fe^{2+}$ organisms interact with in terms of both the $Fe^{2+}$ species used as the reactant and the $Fe^{3+}$ species generated as the oxidation product (Bird *et al.*, 2011). The speciation of $Fe^{2+}$ and $Fe^{3+}$ can impact both the kinetic and the energetic constraints. In aqueous solutions, $Fe^{2+}$ can be present as free $Fe^{2+}$ ions, or in carbonate or hydroxide complexes (Whitney King, 1998; Jolivet *et al.*, 2004). In lake sediments, $Fe^{2+}$ could be chelated by organic acids such

as citrate and humic acids, which are present at low concentrations (Peng *et al.*, 2019) . The presence of chelators could inhibit or accelerate microbial iron oxidation rates (Peng *et al.*, 2018; Peng *et al.*, 2019). $Fe^{2+}$ is also present in minerals that are accessible by microbial oxidation (Shelobolina *et al.*, 2012). The speciation of $Fe^{2+}$ and $Fe^{3+}$ impact the Gibbs energy available from the $Fe^{2+}$ oxidation reaction and can therefore impact the bioenergetics-predicted growth yields of lithoheterotrophy and lithoautotrophy (Bird *et al.*, 2011). Similarly, the relative proportions of DNRA versus denitrification during $NO_3^-$ reduction used in bioenergetic calculations would impact the catabolic energy yields of both the organotrophic and lithotrophic reactions and could impact the predicted outcome of competition between the three MEMs.

### 3.4 Conclusions

Applying the modeling framework developed in Chapter 2 to high resolution sediment geochemical data that are available for Lake Constance predicts that there is simultaneous iron and acetate oxidation, and auto- and hetero- trophy occurring in the $NO_3^-$ reducing zone. These predictions agree with MPN data and the presence of *Gallionella* spp. in the sediment. I also showed how the $NO_3^-$ reduction rate depends on the fraction of autotrophic $NO_3^-$ reducers, using the GEDYM-predicted MEM-specific metabolic reaction stoichiometries. This reinforces the fact that the competition between heterotrophic and autotrophic metabolisms impacts not only C cycling, but also the cycling of N in the sediments. The stoichiometries of how the $Fe^{2+}$ oxidation, $NO_3^-$ reduction, and DIC turnover rates are coupled depends on the fraction of autotrophic versus heterotrophic activity, demonstrating the importance of accounting for mixotrophy in models of real environments. In this chapter, therefore, I have demonstrated the utility of the modeling framework developed in Chapter 2 for better constraining chemical reaction rates in subsurface environments like lake sediments.

This modeling framework could be incorporated into models that simulate the interactions of mixotrophy with other sediment processes to be able to predict the response of NDFO-driven mixotrophy to changes in geochemical conditions. Some examples of environmental forcings that could impact the balance of heterotrophic and autotrophic nitrate reducing MEMs, and therefore also the relative net turnover rates of N, Fe, and C could include: seasonal changes in the discharge of $Fe^{2+}$-rich groundwater through the sediment, for example. If implemented in an advection-diffusion-reaction (*i.e.*, reactive transport) model, the role of the cycling of other elements could also be incorporated. For example, an influx of sulfide to the sediment could increase $Fe^{2+}$ removal by iron sulfide mineral precipitation and decrease Fe(III) reduction rates by increasing the bioavailable sulfur pool in the sediment and increasing the extent of the zone of sulfate reduction. This modeling framework accounts for the role of potential mixotrophic biotic activity in the net process of NDFO. The framework could thus serve as the basis for predicting the biotic contribution in a modeling effort that aims to elucidate the relative roles of mixotrophic $Fe^{2+}$ oxidation and abiotic chemodenitrification.

# Chapter 4
# Conclusions and Perspectives

## 4.1 Summary of key findings

In terrestrial subsurface environments, the turnover of many geochemical species is regulated by microorganisms (*i.e.,* bacteria and archaea). These organisms are chemosynthetic, relying on reduction-oxidation reactions rather than photosynthetic reactions for their growth. Subsurface microbial activity is therefore limited by the chemical energy available in the energetic substrates that are present. Many organisms inhabiting the subsurface possess the capacity to switch between heterotrophic (*i.e.,* the source of biomass carbon is organic carbon compounds) and autotrophic (*i.e.,* the source of biomass carbon is inorganic carbon) modes of metabolism. In addition to directly impacting the balance between the mineralization of organic carbon to inorganic carbon and the fixation of inorganic carbon into biomass, autotrophic and heterotrophic metabolisms have different energetic costs that impact the net turnover rates of other elements in addition to carbon. Therefore, representing this metabolic flexibility is essential for predicting the functions carries out by microbial activities in the subsurface.

This thesis outlines the development and demonstrates the application of a modeling framework for predicting the metabolic flexibility observed in chemosynthetic mixotrophs. This modeling framework consists of a deterministic system of governing equations that describes the allocation of the carbon and energy in a microbial system during growth on a mixture of an organic ED/ carbon source and an inorganic ED. The equations incorporate the utilization rates of the EDs and the growth yields of the different metabolisms that are co-occurring during mixotrophy. These can also be described as the "kinetic and energetic constraints," respectively. The growth yields of each of the potential metabolisms are calculated *a priori* for the geochemical conditions using the bioenergetic-based Gibbs Energy Dynamic Yield Method.

These “end member metabolisms” represent the potential unique combinations of the two carbon source and two energy sources that are possible in chemosynthetic mixotrophs.

In Chapter 2, the system of governing equations describing mixotrophy is developed and validated using literature datasets of chemostat experiments where the incorporation of the organic carbon source into biomass carbon was tracked using biochemical methods. Along with measurements of the biomass growth rate and the utilization rates of the two EDs, this enabled the calculation of the observed relative abundances of autotrophic and heterotrophic metabolisms. The system of governing equations describing mixotrophic growth were developed and validated using these experimental results. Application of the calculation method yields relatively good agreement between the observed and predicted relative abundances of the metabolisms.

In Chapter 3, the modeling framework was applied to a geochemical dataset collected from the profundal sediments of Lake Constance, taken from Melton *et al.* (2014). The results of applying the modeling framework to this dataset were consistent with the relative numbers of different metabolic groups in the sediment that were determined by Most Probable Number enumerations, data which were also collected by Melton *et al.* (2014). This dataset was also used to explore the impact of mixotrophic metabolisms on the coupling of the C, N and Fe cycles, by demonstrating the variability of the ratios of their turnover rates with changing relative abundances of autotrophic and heterotrophic metabolisms. The impact of variable fractions of autotrophy on the kinetic parameters describing nitrate (*i.e.*, electron acceptor) turnover was also explored using this dataset.

## 4.2 Research perspectives and future directions

This thesis reinforces that it is the combined kinetic and energetic limitations to microbial activity that control the relative functional abundances of microbial groups in the subsurface. Since these energetic limitations are determined by the combination of electron donor and acceptor used for the catabolic reaction, it is the supply (via the interaction of the generation and transport of these substrates) of energetic substrates that determines the energetic efficiency of microbial growth and activity. The widespread occurrence of autotrophy in subsurface environments is justified by the modeling framework, which mathematically describes when a chemosynthetic microbial system becomes organic carbon-limited. Thus, it predicts ecological niches of heterotrophic and autotrophic metabolisms.

The experimental datasets used in Chapter 2 were collected in controlled chemostat systems that monitored the organic carbon assimilated into biomass and enzyme activities in addition to traditional geomicrobial metrics such as biomass and chemical species. Similarly, the field dataset used in chapter 3 collected genomic data, MPN data, and geochemical data. Targeted experiments and field studies like these which combine geomicrobial measurements with tools for tracking microbial physiology, activity, and energetics are critical to building and validating bioenergetics-based modeling frameworks. These include tools such as calorimetry (*e.g.*, Von Stockar *et al.* 2011; Robador *et al.* 2018), stable isotope probing (*e.g.*, Glaubitz *et al.* 2009), tracing the incorporation and fractionation of natural abundance isotopes (*e.g.*, Vlasceanu, Popa, and Kinkle 1997; Probst *et al.* 2018)), omics techniques (*e.g.*, Dyksma *et al.* 2016; Kusian and Bowien 1997; Li *et al.* 2017). Other tools for tracking microbial physiology and activity could include autofluorescence as a proxy for intracellular redox activity (Yang *et al.* 2012), or spectral induced polarization (Mellage *et al.* 2018).

With the modeling framework outlined in this thesis able to describe chemostat and lake sediment systems that are at steady state (*i.e.*, the supply rates of EDs is unchanging), the sensitivity of mixotrophy to environmental perturbations can be tested. To do this, the modeling framework could be implemented in a kinetic reaction model.

### 4.2.1 Implementation of the modeling framework into a kinetic reaction model

Implementing the modeling framework into a truly kinetic reaction model that describes the evolution of a system over time (*i.e.*, a numerical model that solves a system of governing differential equations that describe the rates of turnover of relevant geochemical species) is the logical next step. Doing so may provide new insights into the dynamic environmental controls on mixotrophy. In addition to the overarching kinetic and energetic controls (*i.e.*, the relative utilization rates of the 2 EDs and the oxidation state of the organic carbon source) on mixotrophy that the modeling framework demonstrates, other environmental forcings could impact the balance between autotrophy and heterotrophy. These could include changes in chemical variables such as pH and $pCO_2$, or changes in temperature. I will briefly outline how the impact of these environmental variables could be accounted for below.

### 4.2.2 Accounting for changes in chemical variables

Both the energetic and kinetic constraints in the mixotrophic modeling framework could respond to changes in chemical variables like pH or $pCO_2$. pH modifies the chemical speciation, and therefore the chemical activity of substrates, which can modify the amount of the bioavailable fraction of a substrate (*i.e.*, the kinetic constraint), while also modifying the Gibbs energy of redox reactions (*i.e.*, the energetic constraints) (Jin and Kirk, 2018a; Jin and Kirk, 2018b). For example, bioenergetic-kinetic modeling approaches have been used to demonstrate how pH controls the balance between the use of iron(III) and methane (Marquart *et al.*, 2018), and sulfate

and iron(III) (Kirk *et al.*, 2016) as electron acceptors coupled to organic carbon oxidation. In the case of mixotrophy, the influence of pH depends on the identity of the mixture of organic ED/ carbon source and inorganic substrates being used by the metabolism. pH is likely to modify the energetics constraints on mixotrophy when protons are present as a product in one and reactant in the other of the two catabolic reactions. Both autotrophic and heterotrophic anabolic reactions typically use protons as reactants (see reactions in Appendix A), but that is also dependent on the ED oxidation reaction required to balance the anabolic reaction.

The impact of $pCO_2$ on the competition between autotrophy and heterotrophy could be important, since one anabolic reaction requires dissolved inorganic carbon species (*i.e.*, $CO_2$, $HCO_3^-$, and/ or $H_2CO_3$) as reactants, while the other generates them as products. The sensitivity of any reaction to changes in the activity of a reactant or product does depend on the stoichiometric coefficient in front of that reactant/product (Jin and Kirk, 2018a). At low $pCO_2$ levels, limitation of autotrophy by the availability of inorganic carbon limitation could be an important constraint, which could be accounted for by incorporating a kinetic limitation factor for inorganic carbon.

### 4.2.3 Accounting for changes in temperature

Temperature would impact the kinetic parameters $\mu_{max}$ and $K_s$ (Ratkowsky *et al.*, 1982; Price and Sowers, 2004; Schaum *et al.*, 2018). The response of $\mu_{max}$ to changes in temperature is proposed to be an asymmetric curve (Price and Sowers, 2004). There is some temperature at which the maximum specific growth rate is at a maximum, and this temperature lies somewhere in the range of temperatures at which the organism can grow. Alternatively, temperature sensitivity can be represented using an Arrhenius-inspired $Q_{10}$ factor that is used to modify $\mu_{max}$ (Dale *et al.*, 2006). Interestingly, the metabolic theory of ecology posits that the $\mu_{max}$ of

photosynthetic autotrophic metabolisms are less sensitive to temperature than heterotrophic metabolisms, and therefore that systems will become more heterotrophic with increasing temperature (Allen *et al.*, 2005).

The sensitivity of the Gibbs energies of metabolism and therefore also growth yields to temperature can be accounted for using the van't Hoff equation (Dale *et al.*, 2006). According to the van't Hoff equation, exothermic reactions which produce heat to in the forward direction should become less energy-yielding with increased temperature. Both chemoautotrophic and chemoheterotrophic metabolisms are typically exothermic, although chemoheterotrophic metabolisms tend to be more exothermic. Changes in temperature could therefore impact the energetic constraints on autotrophic and heterotrophic metabolisms to different extents.

### 4.2.5 The potential to predict "the priming effect" in soils

A kinetic-bioenergetic framework could be used to describe the "priming" of organic ED substrates in the presence of other organic ED substrates. The "priming effect" describes the enhanced degradation of a less "labile" ED in the presence of another, more labile ED (Guenet *et al.*, 2010). The concept of "lability" effectively describes the amount of chemical energy released by the oxidation of an organic ED, and thus its favourability to be used for microbial metabolism. Lability is therefore related to the degree of reduction of an organic ED. The degree of lability is also related to the energetic costs of breaking the substrate down for energy use (*e.g.*, cellulose and other polymers are considered less labile). In addition to the enhanced degradation of the less labile ED, the priming effect is also associated with increased microbial growth efficiency using the more labile ED. The priming effect has been proposed as a key mechanism for soil C retention in biomass and potential storage (Fontaine, Mariotti, & Abbadie, 2003; Qiao *et al.*, 2014) The relative lability of the two ED substrates could be represented using

bioenergetics, making the bioenergetic-kinetic modeling framework an ideal framework for representing the priming effect.

# Bibliography


Adams D. D. and Baudo R. (2001) Gases ($CH_4$, $CO_2$ and $N_2$) and pore water chemistry in the surface sediments of Lake Orta, Italy: Acidification effects on C and N gas cycling. *J. Limnol.* **60**, 79–90.

Alfreider A., Vogt C., Hoffmann D. and Babel W. (2003) Diversity of ribulose-1,5-bisphosphate carboxylase/oxygenase large-subunit genes from groundwater and aquifer microorganisms. *Microb. Ecol.* **45**, 317–328.

Algar C. K. and Vallino J. J. (2014) Predicting microbial nitrate reduction pathways in coastal sediments. *Aquat. Microb. Ecol.* **71**, 223–238.

Allen A. P., Gillooly J. F. and Brown J. H. (2005) Linking the global carbon cycle to individual metabolism. *Funct. Ecol.* **19**, 202–213.

Altermatt F., Alther R., Fišer C., Jokela J., Konec M., Küry D., Mächler E., Stucki P. and Westram A. M. (2014) Diversity and distribution of freshwater amphipod species in Switzerland (Crustacea: Amphipoda). *PLoS One*.

Anantharaman K., Brown C. T., Hug L. A., Sharon I., Castelle C. J., Probst A. J., Thomas B. C., Singh A., Wilkins M. J., Karaoz U., Brodie E. L., Williams K. H., Hubbard S. S. and Banfield J. F. (2016) Thousands of microbial genomes shed light on interconnected biogeochemical processes in an aquifer system. *Nat. Commun.* **7**, 1–11.

Arora B., Cheng Y., King E., Bouskill N. and Brodie E. (2015) Modeling microbial energetics and community dynamics. In *Handbook of Metal-Microbe Interactions and Bioremediation* (eds. S. Das and H. R. Dash). CRC Press, Boca Raton. pp. 445–454.

Arora B., Dwivedi D., Spycher N. and Steefel C. (2017) On modeling $CO_2$ dynamics in a flood plain aquifer. *Procedia Earth Planet. Sci.* **17**, 408–411. Available at: http://linkinghub.elsevier.com/retrieve/pii/S1878522016301370.

Arora B., Spycher N. F., Steefel C. I., Molins S., Bill M., Conrad M. E., Dong W., Faybishenko B., Tokunaga T. K., Wan J., Williams K. H. and Yabusaki S. B. (2016) Influence of hydrological, biogeochemical and temperature transients on subsurface carbon fluxes in a flood plain environment. *Biogeochemistry* **127**, 367–396.

Bellini M. I., Kumaresan D., Tarlera S., Murrell J. C. and Fernández-Scavino A. (2018) Identification of active denitrifiers by DNA-stable isotope probing and amplicon sequencing reveals *Betaproteobacteria* as responsible for attenuation of nitrate contamination in a low impacted aquifer. *FEMS Microbiol. Ecol.* **94**, 1–13.

Berg J. S., Michellod D., Pjevac P., Martinez-Perez C., Buckner C. R. T., Hach P. F., Schubert C. J., Milucka J. and Kuypers M. M. M. (2016) Intensive cryptic microbial iron cycling in the low iron water column of the meromictic Lake Cadagno. *Environ. Microbiol.* **18**, 5288–5302.

Bethke C. M. (2008) *Geochemical and Biogeochemical Reaction Modeling*. Second. ed. C. M. Bethke, Cambridge University Press, Cambridge.

Bethke C. M., Sanford R. A., Kirk M. F., Jin Q. and Flynn T. M. (2011) The thermodynamic ladder in geomicrobiology. *Am. J. Sci.* **311**, 183–210.

Bird L. J., Bonnefoy V. and Newman D. K. (2011) Bioenergetic challenges of microbial iron metabolisms. *Trends Microbiol.* **19**, 330–340.

Blöthe M. and Roden E. E. (2009) Composition and activity of an autotrophic Fe(II)-oxidizing, nitrate-reducing enrichment culture. *Appl. Environ. Microbiol.* **75**, 6937–6940.

Bosch J. and Meckenstock R. U. (2012) Rates and potential mechanism of anaerobic nitrate-dependent microbial pyrite oxidation. *Biochem. Soc. Trans.* **40**, 1280–1283.

Bouwman A. F., Bierkens M. F. P., Griffioen J., Hefting M. M., Middelburg J. J., Middelkoop H. and Slomp C. P. (2013) Nutrient dynamics, transfer and retention along the aquatic continuum from land to ocean: Towards integration of ecological and biogeochemical models. *Biogeosciences* **10**, 1–23.

Bowien B., Friedebold J., Kusian D., Bommer D. and Schaferjohann J. (1996) Biochemistry and genetics of organoautotrophy in *Alcaligenes eutrophus*. In *Microbial growth on C1 compounds* (eds. M. E. Lidstrom and F. R. Tabita). Kluwer Academic Publishers, Dordrecht, The Netherlands.

Bradford M. A., Wieder W. R., Bonan G. B., Fierer N., Raymond P. A. and Crowther T. W. (2016) Managing uncertainty in soil carbon feedbacks to climate change. *Nat. Clim. Chang.* **6**, 751–758. Available at: http://dx.doi.org/10.1038/nclimate3071.

Brookfield A. E., Blowes D. W. and Mayer K. U. (2006) Integration of field measurements and reactive transport modelling to evaluate contaminant transport at a sulfide mine tailings impoundment. *J. Contam. Hydrol.* **88**, 1–22.

Bryce C., Blackwell N., Schmidt C., Otte J., Huang Y., Kleindienst S., Tomaszewski E., Schad M., Warter V., Peng C., Byrne J. and Kappler A. (2018) Microbial anaerobic Fe(II) oxidation - ecology, mechanisms and environmental implications. *Environ. Microbiol.* **20**, 3462–3483. Available at: http://doi.wiley.com/10.1111/1462-2920.14328.

Buchkowski R. W., Bradford M. A., Grandy A. S., Schmitz O. J. and Wieder W. R. (2017) Applying population and community ecology theory to advance understanding of belowground biogeochemistry. *Ecol. Lett.* **20**, 231–245.

Burgin A. J., Yang W. H., Hamilton S. K. and Silver W. L. (2011) Beyond carbon and nitrogen: How the microbial energy economy couples elemental cycles in diverse ecosystems. *Front. Ecol. Environ.* **9**, 44–52.

Byrne-Bailey K. G., Weber K. A. and Coates J. D. (2012) Draft genome sequence of the anaerobic, nitrate-dependent, Fe(II)-oxidizing bacterium *Pseudogulbenkiania ferrooxidans* strain 2002. *J. Bacteriol.* **194**, 2400–2401.

Van Cappellen P., Gaillard J.-F. and Rabouille C. (1993) Biogeochemical transformations in sediments: Kinetic models of early diagenesis. In *Interactions of C, N, P and S Biogeochemical Cycles and Global Change. Volume 4 of NATO advanced science institutes series: Global environmental change.* (eds. R. Wollast, F. T. Mackenzie, and L. Chou). Springer Berlin Heidelberg. pp. 401–445.

Cardoso R. B., Sierra-Alvarez R., Rowlette P., Flores E. R., Gómez J. and Field J. A. (2006) Sulfide oxidation under chemolithoautotrophic denitrifying conditions. *Biotechnol. Bioeng.* **95**, 1148–1157.

Carlson H. K., Clark I. C., Blazewicz S. J., Iavarone A. T. and Coates J. D. (2013) Fe(II) oxidation is an innate capability of nitrate-reducing bacteria that involves abiotic and biotic reactions. *J. Bacteriol.* **195**, 3260–3268.

Chakraborty A. and Picardal F. (2013) Induction of nitrate-dependent Fe(II) oxidation by Fe(II) in Dechloromonas sp. strain UWNR4 and *Acidovorax* sp. strain 2AN. *Appl. Environ. Microbiol.* **79**, 748–752.

Chakraborty A., Roden E. E., Schieber J. and Picardal F. (2011) Enhanced growth of *Acidovorax* sp. strain 2AN during nitrate-dependent Fe(II) oxidation in batch and continuous-flow systems. *Appl. Environ. Microbiol.* **77**, 8548–8556.

Couture R. M., Gobeil C. and Tessier A. (2010) Arsenic, iron and sulfur co-diagenesis in lake sediments. *Geochim. Cosmochim. Acta* **74**, 1238–1255.

Dale A., Regnier P. and Van Cappellen P. (2006) Bioenergetic controls of anaerobic oxidation of methane in organic-rich marine sediments: A sensitivity analysis. *Am. J. Sci.* **306**, 246–294.

Dijkhuizen L., Groen L., Harder W. and Konings W. N. (1977a) Active transport of oxalate by *Pseudomonas oxalaticus* OX1. *Arch. Microbiol.* **115**, 223–227.

Dijkhuizen L. and Harder W. (1984) Current views on the regulation of autotrophic carbon dioxide fixation via the Calvin cycle in bacteria. *Antonie Van Leeuwenhoek* **50**, 473–487.

Dijkhuizen L. and Harder W. (1979) Regulation of autotrophic and heterotrophic metabolism in *Pseudomonas oxalaticus* OX1. *Arch. Microbiol.* **123**.

Dijkhuizen L., van der Werf B. and Harder W. (1980) Metabolic regulation in Pseudomonas oxalaticus OX1. Diauxic growth on mixtures of oxalate and formate or acetate. *Arch. Microbiol.* **124**, 261–268.

Dijkhuizen L., Wiersma M. and Harder W. (1977b) Energy production and growth of *Pseudomonas oxalaticus* OX1 on oxalate and formate. *Arch. Microbiol.* **115**, 229–236.

Dwivedi D., Arora B., Steefel C. I., Dafflon B. and Versteeg R. (2018) Hot spots and hot moments of nitrogen in a riparian corridor. *Water Resour. Res.* **54**, 205–222.

Emerson J. B., Thomas B. C., Alvarez W. and Banfield J. F. (2016) Metagenomic analysis of a high carbon dioxide subsurface microbial community populated by chemolithoautotrophs and bacteria and archaea from candidate phyla. *Environ. Microbiol.* **18**, 1686–1703.

Esteve-Núñez A., Rothermich M., Sharma M. and Lovley D. (2005) Growth of Geobacter sulfurreducens under nutrient-limiting conditions in continuous culture. *Environ. Microbiol.* **7**, 641–648.

Fleming E. J., Woyke T., Donatello R., Kuypers M., Sczyrba A., Littmann S. and Emerson D. (2018) Insights into the fundamental physiology of the uncultured Fe-oxidizing bacteria *Leptothrix ochracea*. *Appl. Environ. Microbiol.* **84**, 1–15.

Fontaine S., Mariotti A. and Abbadie L. (2003) The priming effect of organic matter: A question of microbial competition? *Soil Biol. Biochem.* **35**, 837–843.

Francois C. M., Mermillod-Blondin F., Malard F., Fourel F., Lécuyer C., Douady C. J. and Simon L. (2016) Trophic ecology of groundwater species reveals specialization in a low-productivity environment. *Funct. Ecol.* **30**, 262–273.

Geelhoed J. S., Sorokin D. Y., Epping E., Tourova T. P., Banciu H. L., Muyzer G., Stams A. J. M. and Van Loosdrecht M. C. M. (2009) Microbial sulfide oxidation in the oxic-anoxic transition zone of freshwater sediment: Involvement of lithoautotrophic *Magnetospirillum* strain J10. *FEMS Microbiol. Ecol.* **70**, 54–65.

Gommers P. J. F., Van Schie B. J., Van Dijken J. P. and Kuenen J. G. (1988) Biochemical limits to microbial growth yields: An analysis of mixed substrate utilization. *Biotechnol. Bioeng.* **32**, 86–94.

Gottschal J. C. (1993) Growth kinetics and competition - some contemporary comments. *Antonie Van Leeuwenhoek* **63**, 299–313.

Gottschal J. C. and Dijkhuizen L. (1988) The place of continuous culture in ecological research. In *CRC Handbook of Laboratory Model Systems for Microbial Ecosystems* (ed. J. Wimpenny). CRC Press, Inc., Boca Raton, Florida. pp. 19–31.

Gottschal J. C. and Kuenen G. (1980) Mixotrophic growth of *Thiobacillus* A2 on acetate and thiosulfate as growth limiting substrates in the chemostat. *Arch. Microbiol.* **126**, 33–42.

Gottschal J. C. and Thingstad T. F. (1982) Mathematical description of competition between two and three bacterial species under dual substrate limitation in the chemostat: A comparison with experimental data. *Biotechnol. Bioeng.* **24**, 1403–1418.

Griebler C. and Avramov M. (2015) Groundwater ecosystem services: A review. *Freshw. Sci.* **34**, 355–367.

Griebler C. and Lueders T. (2009) Microbial biodiversity in groundwater ecosystems. *Freshw. Biol.* **54**, 649–677.

Guenet B., Danger M., Abbadie L. and Lacroix G. (2010) Priming effect: Bridging the gap between terrestrial and aquatic ecology. *Ecology* **91**, 2850–2861.

Hallbeck L. and Pedersen K. (1991) Autotrophic and mixotrophic growth of *Gallionella ferruginea*. *J. Gen. Microbiol.* **137**, 2657–2661.

Handley K. M., Verberkmoes N. C., Steefel C. I., Williams K. H., Sharon I., Miller C. S., Frischkorn K. R., Chourey K., Thomas B. C., Shah M. B., Long P. E., Hettich R. L. and Banfield J. F. (2013) Biostimulation induces syntrophic interactions that impact C, S and N cycling in a sediment microbial community. *ISME J.* **7**, 800–816. Available at: http://dx.doi.org/10.1038/ismej.2012.148.

Hauck S., Benz M., Brune A. and Schink B. (2001) Ferrous iron oxidation by denitrifying bacteria in profundal sediments of a deep lake (Lake Constance). *FEMS Microbiol. Ecol.* **37**, 127–134.

He J. Z., Shen J. P., Zhang L. M., Zhu Y. G., Zheng Y. M., Xu M. G. and Di H. (2007) Quantitative analyses of the abundance and composition of ammonia-oxidizing bacteria and ammonia-oxidizing archaea of a Chinese upland red soil under long-term fertilization practices. *Environ. Microbiol.* **9**, 2364–2374.

Heijnen J. J. and van Dijken J. P. (1992) In search of a thermodynamic description of biomass yields for the chemotrophic growth of microorgansims. *Biotechnol. Bioengeneering* **39**, 833–852.

Herrmann M., Rusznyák A., Akob D. M., Schulze I., Opitz S., Totsche K. U. and Küsel K. (2015) Large fractions of $CO_2$-fixing microorganisms in pristine limestone aquifers appear to be involved in the oxidation of reduced sulfur and nitrogen compounds. *Appl. Environ. Microbiol.* **81**, 2384–2394.

Hubbard C. G., Cheng Y., Engelbrekston A., Druhan J. L., Li L., Ajo-franklin J. B., Coates J. D., Conrad M. E., Miller L. G., States U., Conrad M. E. and Berkeley L. (2014) Isotopic insights into microbial sulfur cycling in oil reservoirs. *Front. Microbiol.* **5**, 1–12.

Hug L. A. and Co R. (2018) It takes a village: Microbial communities thrive through interactions and metabolic handoffs. *mSystems* **3**, e00152-17.

Huitema C. and Horsman G. (2018) Analyzing enzyme kinetic data using the powerful statistical capabilities of R. *bioRxiv Biochem.* **10**. Available at: http://biorxiv.org/cgi/content/short/316588v1.

Hunter K. S., Wang Y. and Van Cappellen P. (1998) Kinetic modeling of microbially-driven redox chemistry of subsurface environments: coupling transport, microbial metabolism and geochemistry. *J. Hydrol.* **209**, 53–80.

Hutchins B. T., Engel A. S., Howlin W. H. and Schwartz B. F. (2016) Chemolithoautotrophy supports macroinvertebrate food webs and affects diversity and stability in groundwater communities. *Ecology* **97**, 1530–1542.

Ishii S., Joikai K., Otsuka S., Senoo K. and Okabe S. (2016) Denitrification and nitrate-dependent Fe(II) oxidation in various Pseudogulbenkiania strains. *Microbes Environ.* **31**,

293–298.
Jamieson J., Prommer H., Kaksonen A. H., Sun J., Siade A. J., Yusov A. and Bostick B. (2018) Identifying and quantifying the intermediate processes during nitrate-dependent iron(II) oxidation. *Environ. Sci. Technol.* **52**, 5771–5781.
Jewell T. N. M., Karaoz U., Brodie E. L., Williams K. H. and Beller H. R. (2016) Metatranscriptomic evidence of pervasive and diverse chemolithoautotrophy relevant to C, S, N and Fe cycling in a shallow alluvial aquifer. *ISME J.* **10**, 2106–2117.
Jin Q. and Bethke C. M. (2003) A new rate law describing microbial respiration. *Appl. Environ. Microbiol.* **69**, 2340–2348.
Jin Q. and Kirk M. F. (2018a) pH as a primary control in environmental microbiology: 1. Thermodynamic perspective. *Front. Environ. Sci.* **6**, 1–15.
Jin Q. and Kirk M. F. (2018b) pH as a primary control in environmental microbiology: 2. Kinetic perspective. *Front. Environ. Sci.* **6**, 1–16.
Jolivet J.-P., Chanéac C. and Tronc E. (2004) Iron oxide chemistry. From molecular clusters to extended solid networks. *Chem. Commun.*, 477–483.
Katayama Y., Hiraishi A. and Kuraishi H. (1995) *Paracoccus thiocyanatus* sp. nov., a new species of thiocyanate-utilizing facultative chemolithotroph, and transfer of *Thiobacillus versutus* to the genus *Paracoccus* as *Paracoccus versutus* comb. nov. with emendation of the genus. *Microbiology* **141**, 1469–1477.
Kellermann C., Selsi D., Lee N., Hugler M., Esperchutz J., Hartmann A. and Griebler C. (2012) Microbial $CO_2$ fixation potential in a tar-oil-contaminated porous aquifer. *FEMS Microbiol. Ecol* **81**, 172–187.
Kelly D. P. (1981) Introduction to chemolithotrophic bacteria. In *The Prokaryotes Volume 1* (eds. M. Starr, H. Stolp, H. Truper, A. Balows, and H. Schlegel). Springer-Verlag Berlin Heidelberg, New York. pp. 997–1004.
Kieft T. L. (2016) Microbiology of the deep continental biosphere. In *Their World: A Diversity of Microbial Environments* (ed. C. J. Hurst). Spring International Publishing, Switzerland. pp. 225–250.
Kirk M. F., Jin Q. and Haller B. R. (2016) Broad-scale evidence that pH influences the balance between microbial iron and sulfate reduction. *Groundwater* **54**, 406–413.
Kleerebezem R. and Van Loosdrecht M. C. M. (2010) A generalized method for thermodynamic state analysis of environmental systems. *Crit. Rev. Environ. Sci. Technol.* **40**, 1–54.
Klueglein N. and Kappler A. (2013) Abiotic oxidation of Fe(II) by reactive nitrogen species in cultures of the nitrate-reducing Fe(II) oxidizer *Acidovorax* sp. BoFeN1 - questioning the existence of enzymatic Fe(II) oxidation. *Geobiology* **11**, 180–190.
Koenig A. and Liu L. H. (2001) Kinetic model of autotrophic denitrification in sulphur packed-bed reactors. *Water Res.* **35**, 1969–1978.
Kopf S. H., Henny C. and Newman D. K. (2013) Ligand-enhanced abiotic iron oxidation and the effects of chemical versus biological iron cycling in anoxic environments. *Environ. Sci. Technol.* **47**, 2602–2611.
Kovarova-Kovar K. and Egli T. (1998) Growth kinetics of suspended microbial cells: From single-substrate-controlled growth to mixed-substrate kinetics. *Microbiol. Mol. Biol. Rev.* **62**, 646–666.
LaRowe D. E. and Van Cappellen P. (2011) Degradation of natural organic matter: A thermodynamic analysis. *Geochim. Cosmochim. Acta* **75**, 2030–2042. Available at: http://dx.doi.org/10.1016/j.gca.2011.01.020.

LaRowe D. E., Dale A. W., Amend J. P. and Van Cappellen P. (2012) Thermodynamic limitations on microbially catalyzed reaction rates. *Geochim. Cosmochim. Acta* **90**, 96–109. Available at: http://dx.doi.org/10.1016/j.gca.2012.05.011.

Laufer K., Røy H. and Jørgensen B. (2016) Evidence for the existence of autotrophic nitrate-reducing Fe(II) - oxidizing bacteria in marine coastal sediment. *Appl. Environ. Microbiol.* **82**, 6120–6131.

Lawrence J. R., Gupta R. and Germida J. J. (1988) Impact of elemental sulfur fertilization on agricultural soils. II. Effects on sulfur-oxidizing populations and oxidation rates. *Can. J. Soil Sci.* **68**, 475–483.

Lee H. Y., Erickson L. E. and Yang S. S. (1985) Analysis of bioenergetic yield and maintenance parameters associated with mixotrophic and photoheterotrophic growth. *Biotechnol. Bioeng.* **27**, 1640–1651.

Li L., Maher K., Navarre-Sitchler A., Druhan J., Meile C., Lawrence C., Moore J., Perdrial J., Sullivan P., Thompson A., Jin L., Bolton E. W., Brantley S. L., Dietrich W. E., Mayer K. U., Steefel C. I., Valocchi A., Zachara J., Kocar B., Mcintosh J., Tutolo B. M., Kumar M., Sonnenthal E., Bao C. and Beisman J. (2017) Expanding the role of reactive transport models in critical zone processes. *Earth-Science Rev.* **165**, 280–301.

Linton J. D. and Stephenson R. J. (1978) A preliminary study on growth yields in relation to the carbon and energy content of various organic growth substrates. *FEMS Microb. Ecol. Lett.* **3**, 95–98.

Liu K., Wu L., Couture R. M., Li W. and Van Cappellen P. (2015) Iron isotope fractionation in sediments of an oligotrophic freshwater lake. *Earth Planet. Sci. Lett.* **423**, 164–172.

Lloyd K. G., Steen A. D., Ladau J., Yin J. and Crosby L. (2018) Phylogenetically novel uncultured microbial cells dominate Earth microbiomes. *mSystems* **3**, 1–12.

Long P. E., Williams K. H., Hubbard S. S. and Banfield J. F. (2016) Microbial metagenomics reveals climate-relevant subsurface biogeochemical processes. *Trends Microbiol.* **24**, 600–610.

Lovley D. R. and Chapelle F. H. (1995) Deep subsurface microbial processes. *Rev. Geophys.* **33**, 365–381.

Marquart K. A., Haller B. R., Paper J. M., Flynn T. M., Boyanov M. I., Shodunke G., Gura C., Jin Q. and Kirk M. F. (2018) Influence of pH on the balance between methanogenesis and iron reduction. *Geobiology*, 1–14.

MathWorks (2016) MATLAB and Statistics Toolbox 2016b.

Matin A. (1978) Organic nutrition of chemolithotrophic bacteria. *Annu. Rev. Microbiol.* **32**, 433–468.

Mayer K. U., Frind E. O. and Blowes D. W. (2002) Multicomponent reactive transport modeling in variably saturated porous media using a generalized formulation for kinetically controlled reactions. *Water Resour. Res.* **38**, 1–20.

Melton E. D., Schmidt C. and Kappler A. (2012) Microbial iron(II) oxidation in littoral freshwater lake sediment: The potential for competition between phototrophic vs. nitrate-reducing iron(II)-oxidizers. *Front. Microbiol.* **3**, 1–12.

Melton E., Stief P., Behrens S., Kappler A. and Schmidt C. (2014) High spatial resolution of distribution and interconnections between Fe- and N-redox processes in profundal lake sediments. *Environ. Microbiol.* **16**, 3287–3303.

Miltner A., Kopinke F.-D., Kindler R., Selesi D., Hartmann A. and Kästner M. (2005) Non-phototrophic $CO_2$ fixation by soil microorganisms. *Plant Soil* **269**, 193–203.

Muehe E. M., Gerhardt S., Schink B. and Kappler A. (2009) Ecophysiology and the energetic benefit of mixotrophic Fe(II) oxidation by various strains of nitrate-reducing bacteria. *FEMS Microbiol. Ecol.* **70**, 335–343.

Newman D. K. and Banfield J. F. (2002) Geomicrobiology: How molecular-scale interactions underpin biogeochemical systems. *Science (80-. ).* **296**, 1071–1077.

Omoregie E. O., Couture R. M., Van Cappellen P., Corkhill C. L., Charnock J. M., Polya D. A., Vaughan D., Vanbroekhoven K. and Lloyd J. R. (2013) Arsenic bioremediation by biogenic iron oxides and sulfides. *Appl. Environ. Microbiol.* **79**, 4325–4335.

Orihel D. M., Baulch H. M., Casson N. J., North R. L., Parsons C. T., Seckar D. C. M. and Venkiteswaran J. J. (2017) Internal phosphorus loading in Canadian fresh waters: a critical review and data analysis. *Can. J. Fish. Aquat. Sci.* **74**, 2005–2029.

Oshiki M., Ishii S., Yoshida K., Fujii N., Ishiguro M., Satoh H. and Okabe S. (2013) Nitrate-dependent ferrous iron oxidation by anaerobic ammonium oxidation (anammox) bacteria. *Appl. Environ. Microbiol.* **79**, 4087–4093.

Pace M. L. and Prairie Y. T. (2005) Respiration in lakes. In *Respiration in Aquatic Ecosystems* (eds. P. del Giorgio and P. Williams). Oxford University Press Inc., Oxford. pp. 103–121.

Parkhurst D. L. and Appelo C. A. J. (2013) PHREEQC (Version 3)-A Computer Program for Speciation, Batch-Reaction, One-Dimensional Transport, and Inverse Geochemical Calculations. U.S. Geological Survey Techniques and Methods, book 6, chap. A43, 497 p., available only at https://pubs.usgs.gov/tm/06/a43/.

Payn R. A., Helton A. M., Poole G. C., Izurieta C., Burgin A. J. and Bernhardt E. S. (2014) A generalized optimization model of microbially driven aquatic biogeochemistry based on thermodynamic, kinetic, and stoichiometric ecological theory. *Ecol. Modell.* **294**, 1–18.

Peng C., Bryce C., Sundman A., Borch T. and Kappler A. (2019) Organic matter complexation promotes Fe(II) oxidation by the photoautotrophic Fe(II)-oxidizer Rhodopseudomonas palustris TIE-1. *ACS Earth Sp. Chem.* **3**, 531–536.

Peng C., Sundman A., Bryce C., Catrouillet C., Borch T. and Kappler A. (2018) Oxidation of Fe(II)-organic matter complexes in the presence of the mixotrophic nitrate-reducing Fe(II)-oxidizing bacterium *Acidovorax* sp. BoFeN1. *Environ. Sci. Technol.* **52**, 5753–5763.

Perez R. C. and Matin A. (1982) Carbon dioxide assimilation by *Thiobacillus novellus* under nutrient-limited mixotrophic conditions. *J. Bacteriol.* **150**, 46–51.

Piché-Choquette S. and Constant P. (2019) Molecular hydrogen, a neglected key driver of soil biogeochemical processes. *Appl. Environ. Microbiol.* Available at: http://aem.asm.org/lookup/doi/10.1128/AEM.02418-18.

Preuß A., Schauder R., Fuchs G. and Stichler W. (1989) Carbon isotope fractionation by autotrophic bacteria with three different $CO_2$ fixation pathways. *Zeitschrift fur Naturforsch. - Sect. C J. Biosci.* **44**, 397–402.

Price P. B. and Sowers T. (2004) Temperature dependence of metabolic rates for microbial growth, maintenance, and survival. *Proc. Natl. Acad. Sci.* **101**, 4631–4636.

Probst A. J., Castelle C. J., Singh A., Brown C. T., Anantharaman K., Sharon I., Hug L. A., Burstein D., Emerson J. B., Thomas B. C. and Banfield J. F. (2017) Genomic resolution of a cold subsurface aquifer community provides metabolic insights for novel microbes adapted to high CO2concentrations. *Environ. Microbiol.* **19**, 459–474.

Probst A. J., Elling F. J., Castelle C. J., Zhu Q., Elvert M., Birarda G., Holman H.-Y., Lane K. R., Ladd B., Ryan M. C., Woyke T., Hinrichs K.-U. and Banfield J. F. (2018) Lipid analysis of $CO_2$-rich subsurface aquifers suggests an autotrophy-based deep biosphere with

lysolipids enriched in CPR bacteria. *bioRxiv Prepr.*, 1–24.
Probst A. J., Weinmaier T., Raymann K., Perras A., Emerson J. B., Rattei T., Wanner G., Klingl A., Berg I. A., Yoshinaga M., Viehweger B., Hinrichs K. U., Thomas B. C., Meck S., Auerbach A. K., Heise M., Schintlmeister A., Schmid M., Wagner M., Gribaldo S., Banfield J. F. and Moissl-Eichinger C. (2014) Biology of a widespread uncultivated archaeon that contributes to carbon fixation in the subsurface. *Nat. Commun.* **5**, 1–13. Available at: http://dx.doi.org/10.1038/ncomms6497.
Qiao N., Schaefer D., Blagodatskaya E., Zou X., Xu X. and Kuzyakov Y. (2014) Labile carbon retention compensates for $CO_2$ released by priming in forest soils. *Glob. Chang. Biol.* **20**, 1943–54. Available at: http://www.ncbi.nlm.nih.gov/pubmed/24293210.
Ratkowsky D., Olley J., McMeekin T. and Ball A. (1982) Relationship between temperature and growth rate of bacterial cultures. *J. Bacteriol.* **149**, 1–5.
Regnier P., Dale A., Pallud C., van Lith Y., Bonneville S., Hyacinthe C., Thullner M. and Van Cappellen P. (2005) Incorporating geomicrobial processes in reactive transport models of subsurface environments. In *Reactive Transport in Soil and Groundwater* (eds. G. Nutzmann, P. Viotti, and P. Aagaard). Berlin, Germany. pp. 109–125.
Rittenberg S. C. (1972) The obligate autotroph - the demise of a concept. *Antonie Van Leeuwenhoek* **38**, 457–478.
Rivett M. O., Buss S. R., Morgan P., Smith J. W. N. and Bemment C. D. (2008) Nitrate attenuation in groundwater: A review of biogeochemical controlling processes. *Water Res.* **42**, 4215–4232.
Robertson E. K., Roberts K. L., Burdorf L. D. W., Cook P. and Thamdrup B. (2016) Dissimilatory nitrate reduction to ammonium coupled to Fe(II) oxidation in sediments of a periodically hypoxic estuary. *Limnol. Oceanogr.* **61**, 365–381.
Robertson E. K. and Thamdrup B. (2017) The fate of nitrogen is linked to iron(II) availability in a freshwater lake sediment. *Geochim. Cosmochim. Acta* **205**, 84–99. Available at: http://dx.doi.org/10.1016/j.gca.2017.02.014.
Roden E. E. and Jin Q. (2011) Thermodynamics of microbial growth coupled to metabolism of glucose, ethanol, short-chain organic acids, and hydrogen. *Appl. Environ. Microbiol.* **77**, 1907–1909.
Rohatgi A. (2019) WebPlotDigitizer. Available at: https://automeris.io/WebPlotDigitizer.
Sato T. and Atomi H. (2010) Microbial inorganic carbon fixation. *Encycl. Life Sci.*, 1–12.
Schaum C.-E., Pawar S., Yvon-Durocher G., Bestion E. and García-Carreras B. (2018) Metabolic traits predict the effects of warming on phytoplankton competition. *Ecol. Lett.*, 655–664.
Schink B. and Benz M. (1999) Microbial metabolism of iron species in freshwater lake sediments. In *Redox: Fundamentals, Processes and Applications* (eds. J. Schüring, H. D. Schulz, W. R. Fischer, J. Böttcher, and W. H. M. Duijnisveld). Springer, Berlin. pp. 228–234.
Schmidt C., Behrens S. and Kappler A. (2010) Ecosystem functioning from a geomicrobiological perspective - a conceptual framework for biogeochemical iron cycling. *Environ. Chem.* **7**, 399–405.
Schulz S. (2002) Influence of temperature on pathways to methane production in the permanently cold profundal sediment of Lake Constance. *FEMS Microbiol. Ecol.* **20**, 1–14.
Schulz S. and Conrad R. (1995) Effect of algal deposition on acetate and methane concentrations in the profundal sediment of a deep lake (Lake Constance). *FEMS Microbiol. Ecol.* **16**,

251–260.
Schulz S. and Conrad R. (1996) Influence of temperature on pathways to methane production in the permanently cold profundal sediment of Lake Constance. *FEMS Microbiol. Ecol.*
Seto M. (2014) The Gibbs free energy threshold for the invasion of a microbial population under kinetic constraints. *Geomicrobiol. J.* **31**, 645–653.
Shelobolina E., Xu H., Konishi H., Kukkadapu R., Wu T., Blöthe M. and Roden E. (2012) Microbial lithotrophic oxidation of structural Fe(II) in biotite. *Appl. Environ. Microbiol.* **78**, 5746–5752.
Sherwood-Lollar B., Lacrampe-Couloume G., Voglesonger K., Onstott T. C., Pratt L. M. and Slater G. F. (2008) Isotopic signatures of $CH_4$ and higher hydrocarbon gases from Precambrian Shield sites: A model for abiogenic polymerization of hydrocarbons. *Geochim. Cosmochim. Acta* **72**, 4778–4795.
Shively J. M., van Keulen G. and Meijer W. G. (2002) Something from almost nothing: Carbon dioxide fixation in chemoautotrophs. *Annu. Rev. Microbiol.* **52**, 191–230.
Smeaton C. M. and Van Cappellen P. (2018) Gibbs Energy Dynamic Yield Method (GEDYM): Predicting microbial growth yields under energy-limiting conditions. *Geochim. Cosmochim. Acta* **241**, 1–16.
Von Stockar U., Marison I., Janssen M. and Patiño R. (2011) Calorimetry and thermodynamic aspects of heterotrophic, mixotrophic, and phototrophic growth. *J. Therm. Anal. Calorim.* **104**, 45–52.
Straub K. L., Benz M., Schink B. and Widdel F. (1996) Anaerobic, nitrate-dependent microbial oxidation of ferrous iron. *Appl. Environ. Microbiol.* **62**, 1458–1460.
Thullner M., Regnier P. and Van Cappellen P. (2007) Modeling microbially induced carbon degradation in redox-stratified subsurface environments: Concepts and open questions. *Geomicrobiol. J.* **24**, 139–155.
Tijhuis L., van Loosdrecht M. C. M. and Heijnen J. J. (1993) A thermodynamically based correlation for maintenance Gibbs energy requirements in anaerobic and aerobic chemotrophic growth. *Biotechnol. Bioeng.* **42**, 509–519.
Torres E., Couture R. M., Shafei B., Nardi A., Ayora C. and Cappellen P. Van (2015) Reactive transport modeling of early diagenesis in a reservoir lake affected by acid mine drainage: Trace metals, lake overturn, benthic fluxes and remediation. *Chem. Geol.* **419**, 75–91.
Vallino J. J. (2010) Ecosystem biogeochemistry considered as a distributed metabolic network ordered by maximum entropy production. *Philos. Trans. R. Soc. B Biol. Sci.* **365**, 1417–1427.
Vallino J. J., Hopkinson C. S. and Hobbie J. E. (1996) Modeling bacterial utilization of dissolved organic matter: Optimization replaces Monod growth kinetics. *Limnol. Oceanogr.* **41**, 1591–1609.
Vollrath S. (2012) Microbial Fe(II) oxidation at circumneutral pH: Reaction kinetics, mineral products, and distribution of neutrophilic iron oxidizers in wetland soils. Utrecht University. Available at: http://igitur-archive.library.uu.nl/dissertations/2012-0110-200347/vollrath.pdf%5Cnpapers2://publication/uuid/6806E599-E2FB-4202-8A7A-EB0FB70B251C.
Wahl B. and Peeters F. (2014) Effect of climatic changes on stratification and deep-water renewal in Lake Constance assessed by sensitivity studies with a 3D hydrodynamic model. *Limnol. Oceanogr.*
Watson I. A., Oswald S. E., Mayer K. U., Wu Y. and Banwart S. A. (2003) Modeling kinetic

processes controlling hydrogen and acetate concentrations in an aquifer-derived microcosm. *Environ. Sci. Technol.* **37**, 3910–3919.

Weber K. A., Urrutia M. M., Churchill P. F., Kukkadapu R. K. and Roden E. E. (2006) Anaerobic redox cycling of iron by freshwater sediment microorganisms. *Environ. Microbiol.* **8**, 100–113.

Wegner C.-E., Gaspar M., Geesink P., Herrmann M., Küsel K. and Marz M. (2018) Biogeochemical regimes in shallow aquifers reflect the metabolic coupling of elements of nitrogen, sulfur and carbon. *Appl. Environ. Microbiol.* **85**, 1–18.

Whitman W. B., Coleman D. C. and Wiebe W. J. (1998) Prokaryotes: The unseen majority. *Proc. Natl. Acad. Sci.* **95**, 6578–6583.

Whitney King D. (1998) Role of carbonate speciation on the oxidation rate of Fe(II) in aquatic systems. *Environ. Sci. Technol.* **32**, 2997–3003.

Wieder W. R., Allison S. D., Davidson E. A., Georgiou K., Hararuk O., He Y., Hopkins F., Luo Y., Smith M. J., Sulman B., Todd-Brown K., Wang Y. P., Xia J. and Xu X. (2015) Global biogeochemical cycles in Earth system models. *Global Biogeochem. Cycles* **29**, 1–19.

Williams K. H., Long P. E., Davis J. A., Wilkins M. J., Guessan A. L. N., Steefel C. I., Yang L., Newcomer D., Frank A., Kerkhof L. J., Mcguinness L., Dayvault R. and Lovley D. R. (2011) Acetate availability and its influence on sustainable bioremediation of uranium-contaminated groundwater. *Geomicrobiol. J.* **28**, 519–539.

Wood A. and Kelly D. (1980) Carbohydrate degradation pathways in Thiobacillus A2 grown on various sugars. *J. Gen. Microbiol.* **120**, 333–345.

Yabusaki S. B., Wilkins M. J., Fang Y., Williams K. H., Arora B., Bargar J., Beller H. R., Bouskill N. J., Brodie E. L., Christensen J. N., Conrad M. E., Danczak R. E., King E., Soltanian M. R., Spycher N. F., Steefel C. I., Tokunaga T. K., Versteeg R., Waichler S. R. and Wainwright H. M. (2017) Water table dynamics and biogeochemical cycling in a shallow, variably-saturated floodplain. *Environ. Sci. Technol.* **51**, 3307–3317.

# Appendix A: Supplementary Information for Chapter 2

***Defining the reaction stoichiometries of the anabolic and catabolic MEM reactions for all 3 literature chemostat studies***

*Table A-1. Catabolic and anabolic end member reaction stoichiometries for experiments carried out in Gottschal and Kuenen, 1979 ("study 1"). The organic ED is acetate ($C_2H_3O_2^-$), while the inorganic ED is thiosulfate ($S_2O_3^{-2}$).*

| Reaction No. | Name | Reaction stoichiometry | Thermodynamic parameters |
|---|---|---|---|
| Catabolic reactions | | | $\Delta G_r^{\circ\prime}$ (kJ (mol ED)$^{-1}$) |
| A-1 | Organotrophy | $0.125C_2H_3O_2^- + 0.25O_2 \rightarrow 0.25HCO_3^- + 0.125H^+$ | -852.78 |
| A-2 | Lithotrophy | $S_2O_3^{2-} + 2O_2 + H_2O \rightarrow 2SO_4^{2-} + 2H^+$ | -773.2 |
| Anabolic reactions | | | $\Delta G_r^{\circ\prime}$ (kJ mol-C$^{-1}$) |
| A-3 | Organohetero-trophy | $0.53C_2H_3O_2^- + 0.2NH_4^+ + 0.28H^+ \rightarrow 0.05HCO_3^- + 0.4H_2O + CH_{1.8}O_{0.5}N_{0.2}$ | 31.2 |
| A-4 | Lithohetero-trophy | $0.15S_2O_3^{2-} + 0.5C_2H_3O_2^- + 0.2NH_4^+ + 0.27H_2O \rightarrow 0.3SO_4^{-2} + 0.05HCO_3^- + 0.06H^+ + CH_{1.8}O_{0.5}N_{0.2}$ | 31.9 |
| A-5 | Lithoauto-trophy | $HCO3^- + 0.53S_2O_3^{2-} + 0.2NH_4^+ + 0.13H_2O \rightarrow CH_{1.8}O_{0.5}N_{0.2} + 1.05SO_4^{-2} + 0.25H^+$ | 46.5 |

*Table A-2. Catabolic and anabolic end member reaction stoichiometries for experiments carried out in Dijkhuizen & Harder, 1979 ("study 2"). The organic ED is oxalate ($C_2O_4^{2-}$), while the inorganic ED is formate ($CHO_2^-$).*

| Reaction No. | Name | Reaction stoichiometry | Thermodynamic parameters |
|---|---|---|---|
| Catabolic reactions | | | $\Delta G_r^{\circ\prime}$ (kJ (mol ED)$^{-1}$) |
| A-6 | Organotrophy | $0.5C_2O_4^{2-} + 0.25O_2 + 0.5\,H_2O \rightarrow HCO_3^-$ | -847.7 |
| A-7 | Lithotrophy | $0.5CHO_2^- + 0.25O_2 \rightarrow 0.5HCO_3^-$ | -283.9 |
| Anabolic reactions | | | $\Delta G_r^{\circ\prime}$ (kJ (C-mol)$^{-1}$) |
| A-8 | Organohetero-trophy | $2.1C_2O_4^{2-} + 0.2NH_4^+ + 1.7H_2O + 0.8H^+ \rightarrow 3.2HCO_3^- + CH_{1.8}O_{0.5}N_{0.2}$ | 31.21 |
| A-9 | Lithohetero-trophy | $1.6CHO_2^- + 0.5C_2O_4^{2-} + 0.2NH_4^+ + 0.1H_2O + 0.8H^+ \rightarrow 1.6HCO_3^- + CH_{1.8}O_{0.5}N_{0.2}$ | 24.9 |
| A-10 | Lithoauto-trophy | $2.1CHO_2^- + 0.2NH_4^+ + 0.8H^+ \rightarrow CH_{1.8}O_{0.5}N_{0.2} + 1.1HCO_3^- + 0.4H_2O$ | -101.5 |

*Table A-3. Catabolic and anabolic end member reaction stoichiometries for experiments carried out in Dijkhuizen, van der Werf, & Harder, 1980 ("study 3"). The organic ED is acetate ($C_2H_3O_2^-$), while the inorganic ED is formate ($CHO_2^-$).*

| Reaction No. | Name | Reaction stoichiometry | Thermodynamic parameters |
|---|---|---|---|
| Catabolic reactions | | | $\Delta G_r^{\circ\prime}$ (kJ (mol ED)$^{-1}$) |
| A-11 | Organotrophy | $0.125C_2H_3O_2^- + 0.25O_2 \rightarrow 0.25HCO_3^- + 0.125H^+$ | -847.7 |
| A-12 | Lithotrophy | $0.5CHO_2^- + 0.25O_2 \rightarrow 0.5HCO_3^-$ | -283.9 |
| Anabolic reactions | | | $\Delta G_r^{\circ\prime}$ (kJ (C-mol)$^{-1}$) |
| A-13 | Organohetero-trophy | $0.53C_2H_3O_2^- + 0.2NH_4^+ + +0.28H^+ \rightarrow 0.05HCO_3^- + 0.4H_2O + CH_{1.8}O_{0.5}N_{0.2}$ | 31.2 |
| A-14 | Lithohetero-trophy | $0.1CHO_2^- + 0.5C_2H_3O_2^- + 0.2NH_4^+ + 0.3H^+ \rightarrow 0.1HCO_3^- + 0.4H_2O + CH_{1.8}O_{0.5}N_{0.2}$ | 24.9 |
| A-15 | Lithoauto-trophy | $2.1CHO_2^- + 0.2NH_4^+ + 0.8H^+ \rightarrow CH_{1.8}O_{0.5}N_{0.2} + 1.1HCO_3^- + 0.4H_2O$ | -101.5 |

***Correcting Gibbs energies for non-standard temperatures***

Gibbs energies of catabolism ($\Delta G^{\circ}_{cat}$) and anabolism ( $\Delta G^{\circ}_{an}$) under standard state conditions are corrected for temperature using the Gibbs-Helmholtz equation (Smeaton and Van Cappellen, 2018):

$$\Delta G^{\circ}_{r\,T} = \Delta G^{\circ}_{r\ 298} \cdot \left(\frac{T}{298.15}\right) + \Delta H^{\circ}_{r\ 298} \cdot \left(\frac{298.15 - T}{298.15}\right) \qquad \text{(A-16)}$$

where *T* is the temperature (K) and $\Delta H^{\circ}_{298}$ is the standard enthalpy change at 298.15 K.

To account for the deviation of the growth medium (*i.e.*, chemical environment) from standard state conditions, Gibbs energies of catabolism ($\Delta G_{cat}$) and anabolism ($\Delta G_{an}$) under non-standard state conditions were determined using Eq. 1-2 (where $\Delta G^{\circ}_{r\,T}$ in place of $\Delta G^{\circ}_{r}$). Meanwhile, the activities of the products and reactants are corrected for temperature in PHREEQC using the temperature correction methods built into the program (Parkhurst and Appelo, 2013). These corrected activities are used to calculate the reaction quotient in Eq. 1-2.

***GEDYM theoretical background and derivation***

The Gibbs Energy Dissipation Method (GEDM) is an example of a $Y$ prediction method which relates the cellular energy balance to $Y$ using (Heijnen and Van Dijken, 1992):

$$Y = \frac{\Delta G_{cat}}{\Delta G_{met} + \nu \Delta G_{cat} - \Delta G_{an}} \tag{A-17}$$

The Gibbs Energy Dynamic Yield Method (GEDYM) builds on the GEDM by explicitly accounting for the deviation of the experimental/environmental conditions from standard-state conditions to improve $Y$ prediction (Smeaton and Van Cappellen, 2018). GEDYM relies on empirical linear relationships between the Gibbs energies of the catabolism and metabolism under standard and non-standard state conditions, expressed as:

$$\left( {\Delta G_{met}} \Big/ {\Delta G^{\,0}_{\,met}} - 1 \right) = m \left( {\Delta G_{cat}} \Big/ {\Delta G^{\,0}_{\,cat}} - 1 \right) + b \tag{A-18}$$

where $m$ and $b$ are the slope and y-intercept, respectively. When Eqs. A-17 and A-18 are combined, $Y$ (C-mol biomass (mol eeq) $^{-1}$) is predicted using:

$$Y = \frac{\alpha \Delta G^{\circ 2}_{cat} - \beta \Delta G^{\circ}_{cat} \Delta G_{cat}}{\alpha \nu \Delta G^{\circ 2}_{cat} - \Delta G^{\circ}_{cat} (\beta \nu \Delta G_{cat} + \alpha \Delta G^{\circ}_{an} + \Delta G_{an}) + m \Delta G_{cat} \Delta G^{\circ}_{an}} \cdot \frac{1}{n_{eeq}} \cdot \tag{A-19}$$

where

$$\alpha = m - b - 1 \tag{A-20}$$

and

$$\beta = m - 1 \tag{A-21}$$

The empirical parameters, $m$, $b$, $\alpha$, and $\beta$ used in Eq. A-19 for heterotrophic and autotrophic metabolisms are summarized in Table A-4:

*Table A-4. Empirical GEDYM parameters used to calculate yield values for heterotrophic and autotrophic metabolisms*

| Metabolism | $\boldsymbol{m}$ | $\boldsymbol{b}$ | $\boldsymbol{\alpha}$ | $\boldsymbol{\beta}$ |
|---|---|---|---|---|
| Heterotrophic metabolisms ("Majority of metabolisms" from: Smeaton and Van Cappellen, 2018) | 0.9306 | −0.0690 | −0.0004 | −0.0694 |
| Autotrophic metabolisms | 1.0168 | -0.0117 | 0.0285 | 0.0168 |

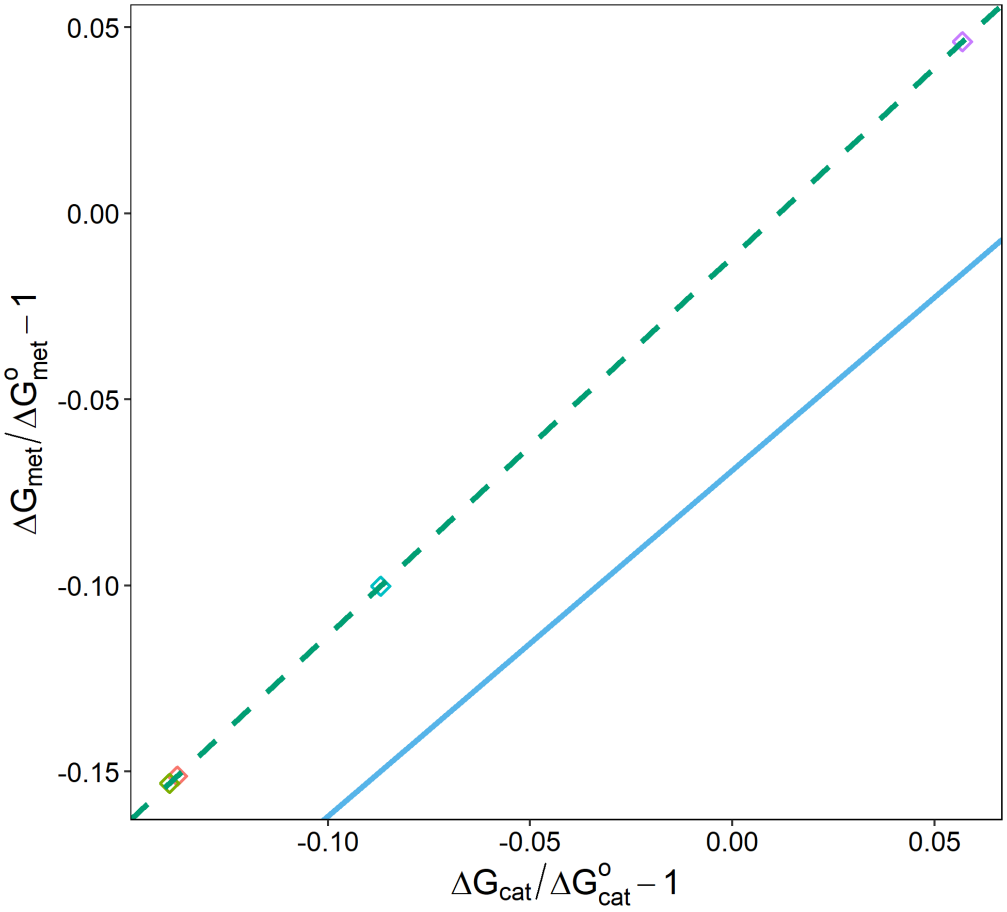


*Figure A-1. Example of linear regressions used by GEDYM, with $\Delta G_{met}/\Delta G^{\circ}_{met} - 1$ plotted versus $\Delta G_{cat}/\Delta G^{\circ}_{cat} - 1$. Green, dotted line represents the linear regression used for autotrophic metabolisms, while the blue line represents that used for heterotrophic metabolisms.*

***Maximum theoretical growth yield ($Y_{max}$)***

A maximum theoretical growth yield ($Y_{max}$) can be determined which corresponds to the $Y$ value when $\Delta G_{met}$ = 0, yet the catabolic reaction remains thermodynamically favorable (*i.e.*, $\Delta G_{cat} < 0$):

$$Y_{max} = \frac{\Delta G_{cat}}{\Delta G_{cat}\nu - \Delta G_{an}} \quad \text{(A-22)}$$

Knowledge of this theoretical maximum growth yield can be used in models to prevent a metabolic reaction from occurring when it is not thermodynamically possible. When $\Delta G_{met}$ calculated using the GEDYM is greater than 0, $Y$ is set to $Y_{max}$, and the reaction is not permitted to occur until the geochemical conditions changes such that $\Delta G_{met}$ value becomes thermodynamically favourable (*i.e.*, $\Delta G_{met} < 0$) (Smeaton and Van Cappellen, 2018).

***Calculating steady state concentrations in the chemostat***

The net utilization rates of the two ED substrates and biomass concentration in the chemostat are known and can be used to calculate the steady state ED concentration using Monod kinetics:

$$r_{ED}^{met} = \frac{X}{Y}\mu_{max}(\frac{C_{ED}}{C_{ED} + K_{ED}}) \quad \text{(A-23)}$$

Re-arranging reaction A16 gives reaction A17, which expresses the steady state concentration of the ED as a function of the ED utilization rate:

$$C_{ED} = \frac{r_{ED}^{met} \cdot Y \cdot K_{ED}}{f_{ED}^{eeq} \cdot X \cdot \mu_{max} - r_{ED}^{met} \cdot Y} \quad \text{(A-24)}$$

The values of $\mu_{max}$ and $K_{ED}$ used for the EDs used in all three studies are summarized in Table A5. Mixotroph-specific $\mu_{max}$ and $K_{ED}$ parameters can be calculated from the parameters of obligate organisms using the relationship proposed by Gottschal and Thingstad (1982). The $\mu_{max}$ values are 25% lower, while the $K_{ED}$ values are also around 25% lower for mixotrophs (*i.e.*, facultative organisms) compared to the value for organisms capable of growing only on the single ED (*i.e.*, obligate organisms). This how the parameters for the growth of *P. versutus* on thiosulfate and acetate were calculated.

Most of the $\mu_{max}$ and $K_{ED}$ values in Table A5 were taken from studies where mixotrophs were grown on the single substrates, so these adjustments to the parameters were not required. The calculation of these parameters is described in the next section.

The ED utilization rates and steady state ED concentrations in all three studies are summarized in Figure A-2.

*Table A-5. Monod kinetic parameters calculated for the growth of P. versutus on acetate and thiosulfate and P. oxalaticus on acetate, oxalate and formate*

| Substrate (Organism) | $\mu_{max}$ ($h^{-1}$) | $K_{ED}$ | Source |
|---|---|---|---|
| Acetate (*P. versutus*) | 0.145 | 1 µM | [1] |
| Thiosulfate (*P. versutus*) | 0.085 | 1 µM | [1] |
| Acetate (*P. oxalaticus*) | 0.432 | 1.4 mM | [2], fitted |
| Oxalate (*P. oxalaticus*) | 0.095 | 0.71 mM | [2], fitted |
| Formate (*P. oxalaticus*) | 0.208 | $9.3 * 10^{-2}$ mM | [2], fitted |

1: (Gottschal and Thingstad, 1982), 2: (Dijkhuizen *et al.*, 1980)

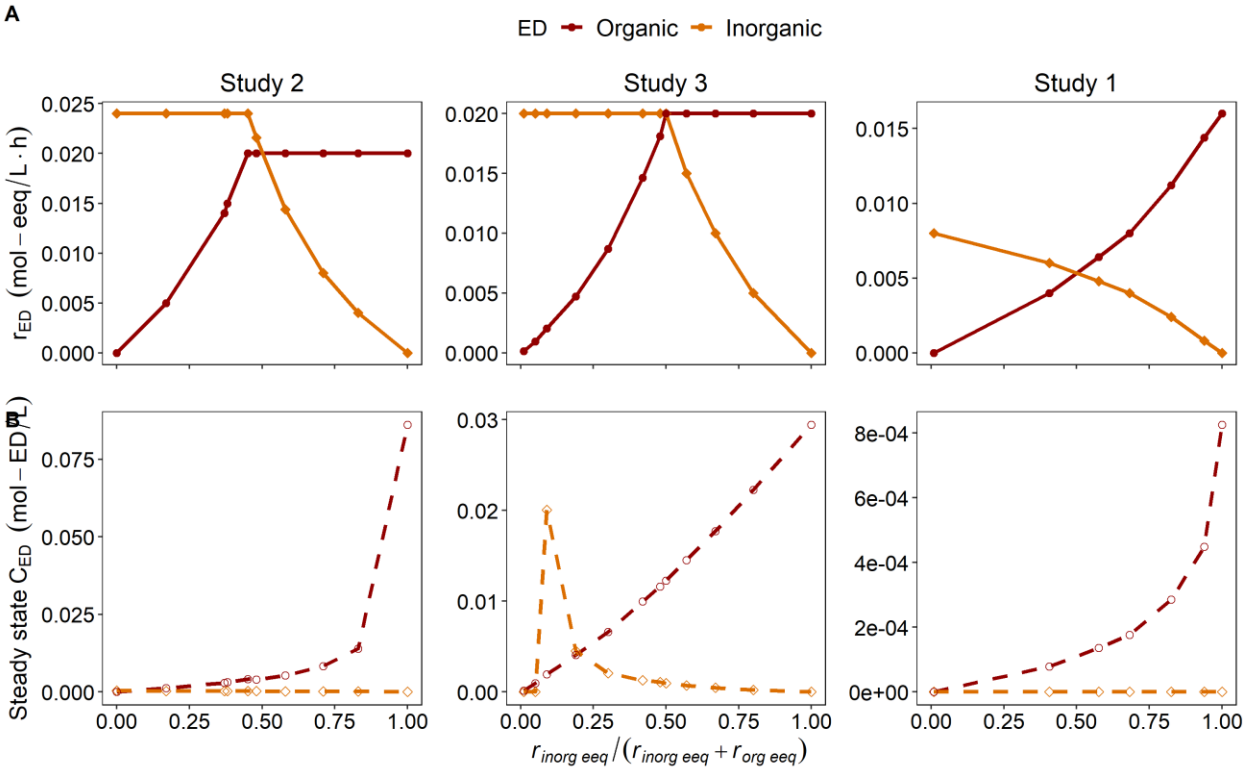


*Figure A-2. ED utilization rates (top panel) and steady state concentration of the two EDs (bottom panel) as a function of the fraction of inorganic electron equivalents consumed for all three studies.*

***Calculating the kinetic parameters for the growth of P. oxalaticus on formate, oxalate and acetate***

To calculate the values of the maximum specific growth rate ($\mu_{max}$) and the half-saturation constant ($K_s$) kinetic parameters for the growth of *P. oxalaticus* on the electron donor (ED) substrates formate, acetate and oxalate, experimental data for these organisms growing in batch culture was used.

The data used came from Dijkhuizen *et al.* (1980). In this study, *P. oxalaticus* was grown on mixtures of two EDs. The optical density of the cells was measured over time, along with the residual concentration of each ED in the culture. Given these data, the specific growth rate can be calculated and related to the residual ED concentration.

In batch culture, specific growth rates are higher, and growth on two substrates is diauxic, meaning that each ED is used one at a time for growth rather than simultaneously. I therefore identified phases where the ED of interest was being used for growth and used those data for calculating the kinetic parameters since I was interested in the kinetic parameters that represented growth on single ED substrates.

The specific growth rate of the cells in batch culture was calculated using the method described in Smeaton and Van Cappellen (2018). Briefly, the doubling time ($t_d$) of the culture at any point during its growth in batch phase was calculated using Eq. A-25:

$$t_d = \frac{0.301(t_2 - t_1)}{\log X_2 - \log X_1} \tag{A-25}$$

where $X_1$ and $X_2$ are cell concentrations (as optical density) measured at times $t_1$ and $t_2$, respectively. Using the doubling time, the specific growth rate (μ) was calculated using Eq. A-26:

$$\mu = \frac{\ln 2}{t_d} \tag{A-26}$$

To calculate the parameters $\mu_{max}$ and $K_s$, the Monod-type equation was fit to the data using a non-linear least squares fitting procedure, using the method and base script outlined by Huitema

and Horsman (2018). Figure A-3 shows the plots of the specific growth rate with residual concentration, and the line of best fit generated using the calculated parameters. Table A-5 summarizes the fitting parameters that were calculated.

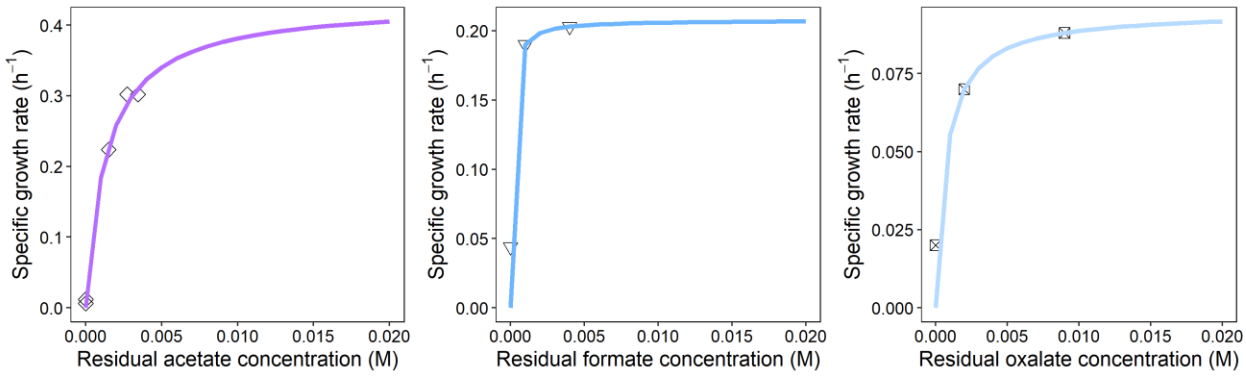


*Figure A-3. Specific growth rate of P. oxalaticus as a function of the steady state (i.e., residual) acetate, formate, and oxalate concentrations during growth in batch culture. Lines shows the line of best fit calculated using the fitted kinetic parameters. Note that the y-axes have different scales, while the scale for all three x-axes is the same.*

***Accounting for biochemical maintenance energies when calculating growth yields using the GEDYM***

The steady state concentrations calculated as described above are used to predict the growth yields using the GEDYM framework. Growth yields calculated using the GEDYM represent the growth yield before non-growth energetic costs (also called maintenance energy) are accounted for. For *Pseudomonas oxalaticus*, some of these costs are known given the detailed biochemistry of the catabolic reactions and experimental evidence:

- During growth on oxalate, 50% of the ATP generated by its oxidation is used for active utilization of oxalate into the cell (Dijkhuizen *et al.*, 1977b; Dijkhuizen *et al.*, 1977a). This was accounted for by multiplying the GEDYM-calculated yield value by 0.5.
- During growth on formate, 25% of the ATP generated by its oxidation is used for its transport into the cell (Dijkhuizen *et al.*, 1977b). This was accounted for by multiplying the GEDYM-calculated yield value by 0.75.
- To match GEDYM predicted yields and observed yields during growth of *P. oxalaticus* on acetate, a factor of 0.5 was required, indicating that 50% of the acetate used for energy is allocated to non-growth costs.

***Trends in Gibbs energies during the transition between MEMs***

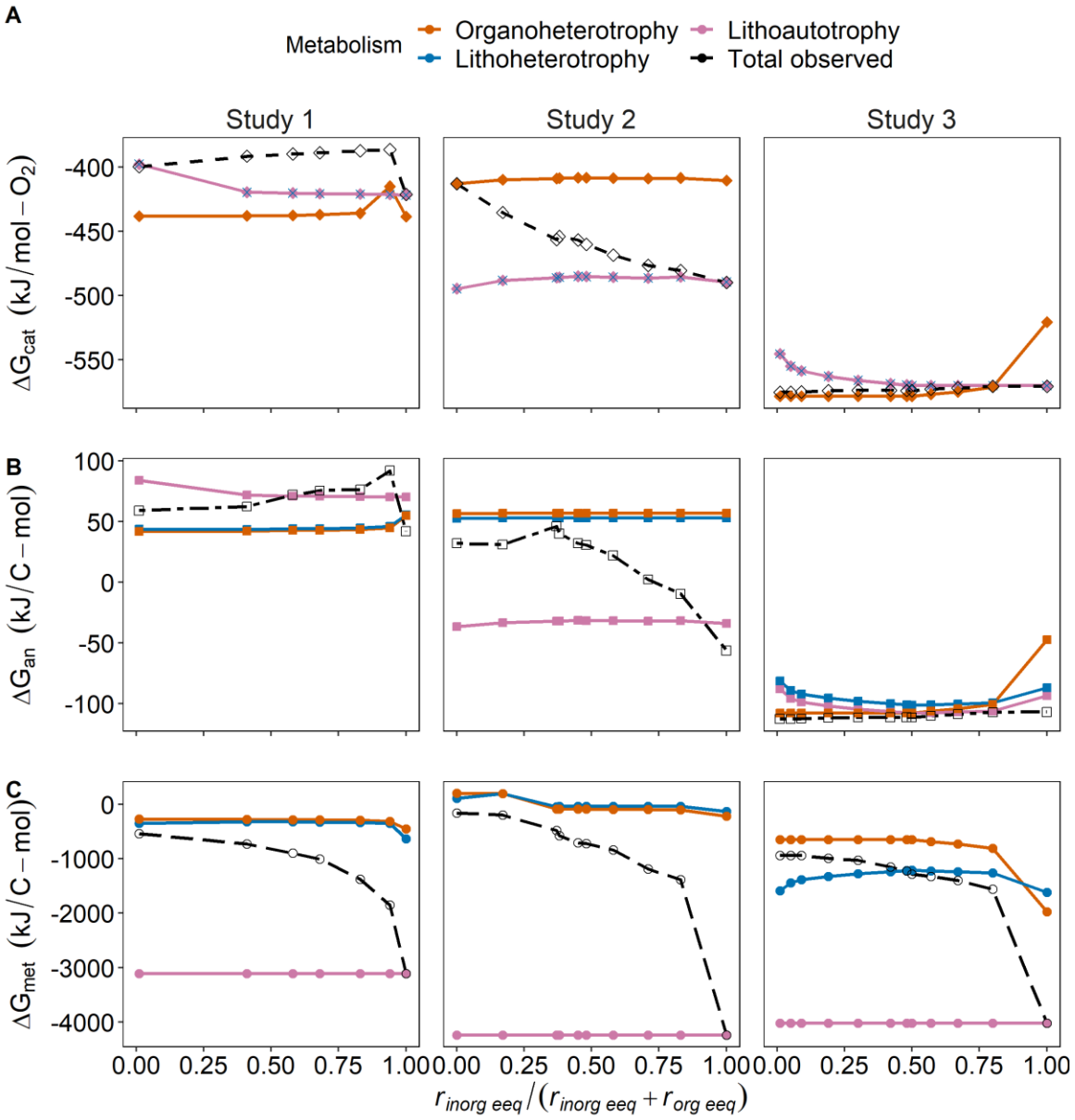


*Figure A-4. Total calculated and MEM specific Gibbs energy of catabolism, $\Delta G_{cat}$ (A) Gibbs energy of anabolism, $\Delta G_{an}$ (B), and Gibbs energy of metabolism, $\Delta G_{met}$ (C), versus fraction of inorganic electron equivalents consumed, $r_{inorg\ eeq}/(r_{inorg\ eeq} + r_{org\ eeq})$.*

# Appendix B: Supplementary Information for Chapter 3

***Digitized geochemical and microbiological data***

These geochemical and microbiological (16S rRNA gene copy number) data were not shown in the main text to save space but were used for the bioenergetic calculations and are therefore shown here in Figures B-1 and B-2 for reference.

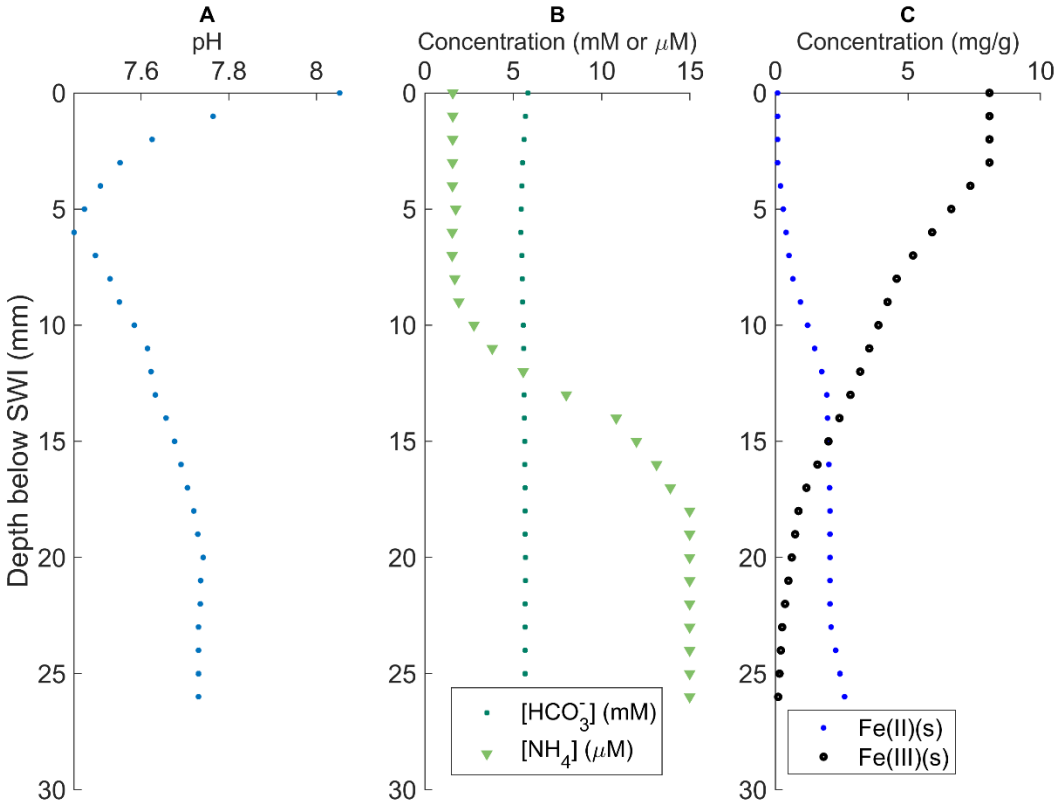


*Figure B-1. Depth profiles of pH, ammonium ($NH_4^+$), and solid phase Fe(II) and Fe(III) taken from Melton et al. (2014). Bicarbonate ($HCO_3^-$) and Fe(II) concentrations were calculated using the geochemical data, as described in chapter 3 of the text.*

***Estimating the geochemical concentrations not available in Melton et al. (2014) needed for bioenergetic calculations***

As with acetate, the dissolved inorganic carbon in the sediment was assumed to be constant at 6.3 mM with depth, based on the information available for Lake Constance (Melton *et al.*, 2012). I entered this into my PHREEQC code to calculate the activity of bicarbonate ($HCO_3^-$) for the given geochemical conditions. The predicted depth profile of $HCO_3^-$ concentrations is shown in Figure B-1. The concentration of $N_2$ in sediments is often around 1 mM (Adams and Baudo, 2001). $N_2$ concentration data were not available for Lake Constance, but I assumed that this would also be the case in those sediments. The activity of goethite was assumed to be 1, since it is a solid. The temperature of the profundal sediments of Lake Constance is 4°C throughout the year (Schulz and Conrad, 1996; Schulz, 2002). This temperature was used to adjust Gibbs energies for non standard temperature (using Eq. A-16) and to adjust the chemical activities computed in PHREEQC and subsequently used to calculate the reaction quotient in Eq. 1-2.

***Digitized microbiological data***

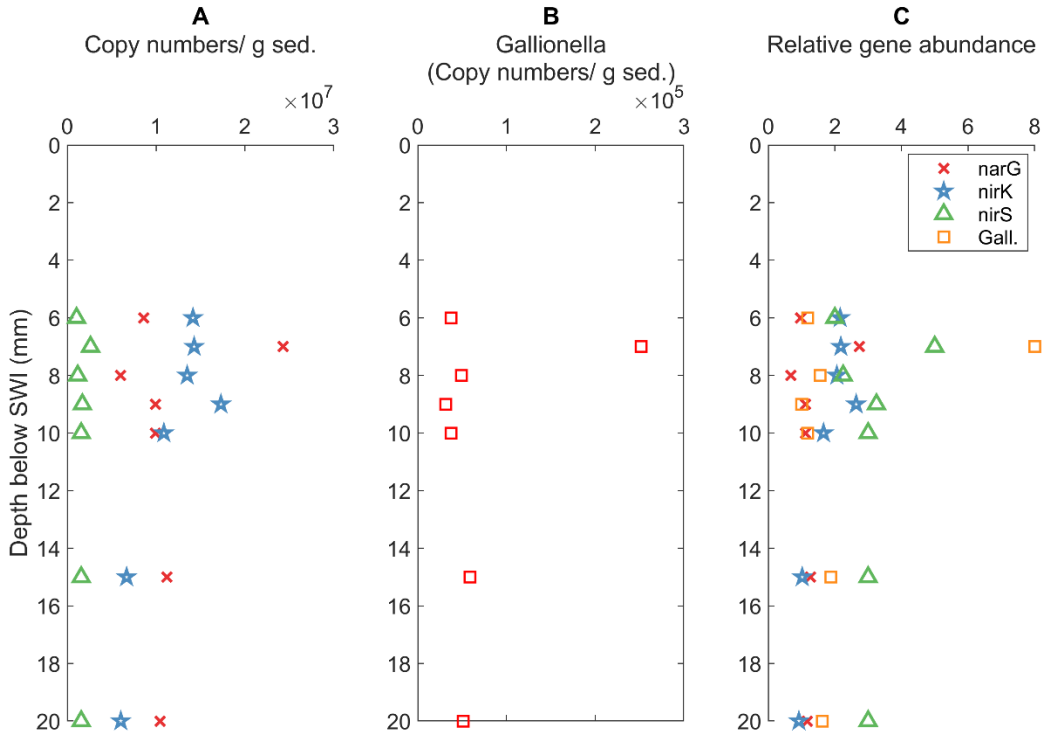


*Figure B-2. Depth profiles of 16S rRNA gene copy numbers of genes involved in nitrate reduction (nirK, nirS, narG) (panel A) and iron (II) oxidation (Gallionella spp., noted in legend as "Gall.") (panel B) as a function of depth in the sediment taken from Melton et al. (2014). The furthest right panel (panel C) shows the relative gene abundances calculated from these gene copy number data.*

"Relative gene abundances" shown in Figure B-2, B-3 and B-4 were calculated by normalizing the copy numbers at each depth by the copy numbers measured at the greatest depth (50 mm, these data are not shown here).

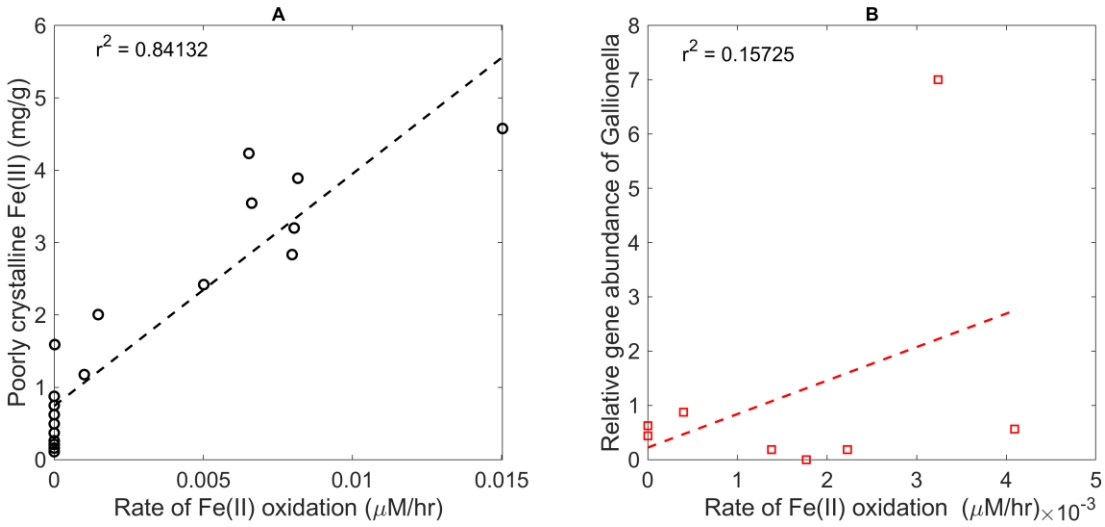


*Figure B-3. Calculated iron oxidation rates versus relative gene abundance of Gallionella (A) and amount of poorly crystalline Fe(III) (B) measured by Melton et al. (2014).*

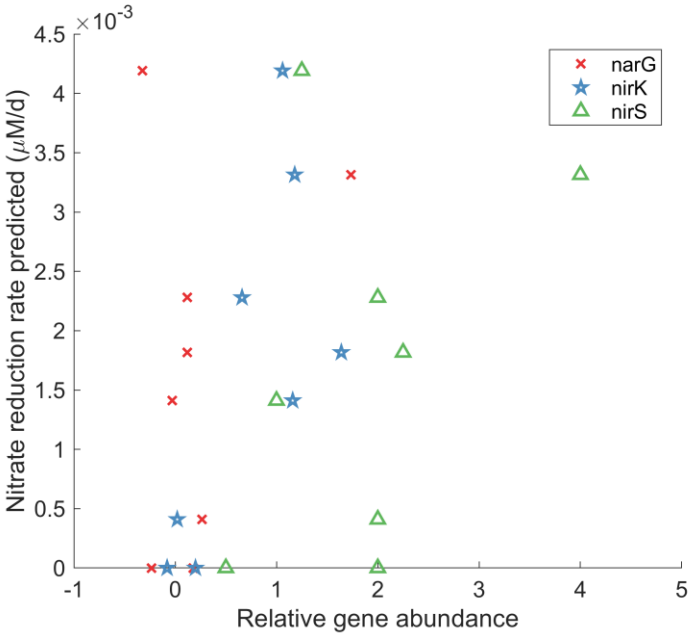


*Figure B-4. Nitrate reduction rate calculated versus relative gene abundance of functional genes relevant to nitrate reduction. "Relative gene abundances" were calculated by normalizing the measured gene copy numbers at each depth to the copy number at the greatest depth measured.*

***Growth yields and Gibbs energies of metabolism calculated with depth in the sediment***

*Table B-1. Catabolic and anabolic end member reaction stoichiometries assumed for nitrate-dependent iron oxidation by mixotrophic organisms such as Gallionella spp.*

| Reaction No. | Name | Reaction stoichiometry | Thermodynamic parameters |
|---|---|---|---|
| Catabolic reactions | | | $\Delta G_r^{\circ\prime}$ (kJ (mol ED)$^{-1}$) |
| 3-3 | Organotrophy | $C_2H_3O_2^- + 1.6NO_3^- + 0.6H^+ \rightarrow 2HCO_3^- + 0.8H_2O + 0.8N_2$ | -816.2 |
| 3-4 | Lithotrophy | $Fe^{+2} + 0.2NO_3^- + 1.4H_2O \rightarrow FeO(OH) + 0.1N_2 + 1.8H^+$ | -49.5 |
| Anabolic reactions | | | $\Delta G_r^{\circ\prime}$ (kJ (C-mol)$^{-1}$) |
| 3-5 | Organohetero-trophy | $0.53C_2H_3O_2^- + 0.2NH_4^+ + + 0.28H^+ \rightarrow 0.05HCO_3^- + 0.4H_2O + CH_{1.8}O_{0.5}N_{0.2}$ | 18.6 |
| 3-6 | Lithohetero-trophy | $0.2Fe^{2+} + 0.2NH_4^+ + 0.5C_2H_3O_2^- \rightarrow CH_{1.8}O_{0.5}N_{0.2} + 0.2FeO(OH) + 0.1H_2O + 0.1H^+$ | 29.0 |
| 3-7 | Lithoauto-trophy | $4.2Fe^{2+} + 0.2NH_4^+ + HCO_3^- + 5.9H_2O \rightarrow CH_{1.8}O_{0.5}N_{0.2} + 4.2FeO(OH) + 7.6H^+$ | 239.1 |

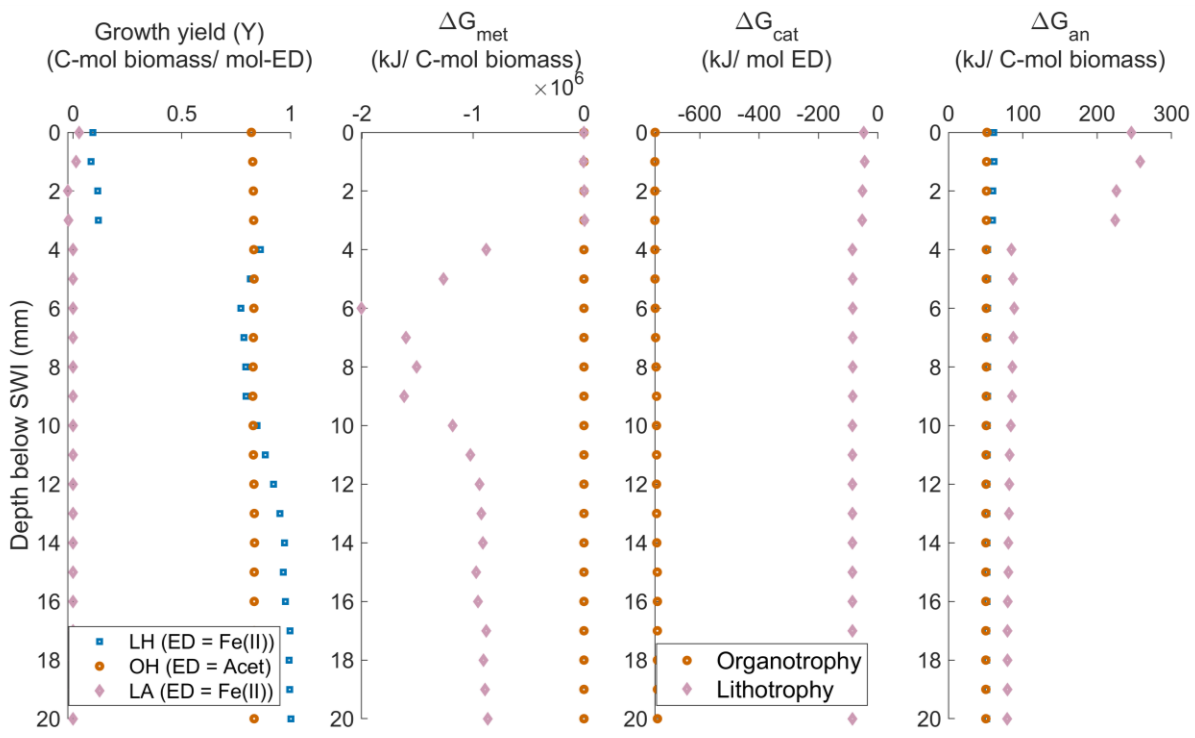


*Figure B-5. Trends in calculated growth yields, and Gibbs energies of metabolism, catabolism and anabolism with depth in the sediment for all 3 MEMs. LH = lithoheterotrophy, LA = lithoautotrophy and OH = organoheterotrophy.*